Design and Analysis of Novel Receiver Front-end Sub-systems in Ku-band for Satellite Applications

by

Sanket S. Patel

(201121005)

A thesis submitted in partial fulfillment of the requirements for the degree of

Doctor of Philosophy

to

Dhirubhai Ambani Institute of Information and Communication Technology,
Gandhinagar, Gujarat, India

December, 2014

Design and Analysis of Novel Receiver Front-end Sub-systems in Ku-band for Satellite Applications

by
Sanket S. Patel

A thesis submitted in partial fulfillment of the requirements for the degree of Doctor of Philosophy
to
Dhirubhai Ambani Institute of Information and Communication Technology, Gandhinagar, Gujarat, India

Author's Declaration

This is to certify that

1. The thesis comprises my original work towards the degree of Doctor of Philosophy in Information and Communication Technology at DA-IICT and has not been submitted elsewhere for a degree,

2. Due acknowledgment has been made in the text to all other material used.

Signature of Student

Certificate

This is to certify that the thesis work entitled "Design and Analysis of Novel Receiver Front-end Sub-systems in Ku-band for Satellite Applications" has been carried out by Sanket Sureshbhai Patel (201121005) for the degree of Doctor of Philosophy in Information and Communication Technology at this Institute under our supervision.

Thesis Supervisor
Prof. (Dr.) Sanjeev Gupta
(DA-IICT)

Thesis Co-supervisor
Prof. (Dr.) Deepak Ghodgaonkar
(DA-IICT)

Dedicated to

my beloved Unnati,

Parents & Family

Design and Analysis of Novel Receiver Front-end Sub-systems in Ku-band for Satellite Applications

by
Sanket S. Patel

A thesis submitted in partial fulfillment of the requirements for the degree of Doctor of Philosophy
to
Dhirubhai Ambani Institute of Information and Communication Technology, Gandhinagar, Gujarat, India

Abstract

A novel receiver front-end; Low Noise Amplifier (LNA), mixer and Local Oscillator (LO); is designed and analyzed in Ku-band. Different design aspects of the subsystems along with the trade-offs and improvements are presented.

Two different configurations of the three-stage cascaded LNAs are designed, analyzed, fabricated and tested. The aim is to design, analyze, and improve the performance parameters of three-stage LNA, especially, to minimize the noise figure while keeping considerable gain. A cumulative approach of two-port modelling and noise extraction is presented. The work is extended to the multistage circuit level analysis from the device level analysis. For the same, sixteen-element device distributed model with all possible inherent resistor temperature noise sources is considered and analyzed. Input referred noise was analyzed and presented in terms of intrinsic and extrinsic parasitics. Noise figure was analyzed in terms of correlated and uncorrelated noises, and the conditions were indentified in our case, to make the noise figure minimum by making the correlated noise ideally zero. The achieved noise figure is as low as 1.46dB (with 30.1dB gain) in Ku-band by analyzing the three-stage LNA considering gain-constrained-noise optimization, extrinsic device parasitics, stability resistor and matching networks to the next stage. Measurement results are promising in comparison with the recent relevant work published in Ku-band LNA.

Next, a wideband 3-dB balanced coupler for the mixer application is presented. Typical rat-race coupler is modified by introducing Composite Left/Right Hand (CRLH) transmission line to provide wideband response. Proposed coupler is small in size (4.3mm X 4.3mm) and provides wideband response in 13–16GHz. Using the coupler presented; small size wideband singly balanced passive mixer in Ku-band is designed. Mixer simulated results are presented in terms of mixer performance parameters; conversion loss, noise figure and linearity. Proposed mixer has low conversion loss (–5dB) and very good Radio Frequency (RF)–LO isolation (–25dB) in Ku-band. The mixer exhibits good linear response which is analyzed by 1–dB compression (4dBm) and 3^{rd} order intercept point (IP_3) (15.7dBm). Two-stage multiband-reject Intermediate Frequency (IF) filter is designed and simulated to suppress– RF, LO frequency, 2^{nd} order intermodulation products, and 3^{rd} order intermodulation products.

To complete the receiver front end, next, low power Ku-band Voltage Controlled Oscillator (VCO) is designed as LO. Using VCO, frequency can be tuned in order to achieve desired IF. Two different new topologies of the negative resistance voltage-controlled oscillators at Ku-band are proposed. In VCO design-1, novel active open ended planar structure is proposed as a resonator for the VCO. Even though being a planar resonator, it provides very good quality factor (up to 235) which ensures low phase noise. VCO microwave IC is fabricated and tested. Measurements show that the VCO can be tuned for 180MHz by varying resonators' varactors from 0V to 22V. Measured output power remains in between 4.20dBm and 8.06dBm for the entire tuning range. Measured normalized Phase Noise Figure of Merit (PNFOM) for the VCO is –214.4dBc/Hz. The DC to RF efficiency ($\eta_{DC\text{-}RF}$) of VCO is 19%. To the best of our knowledge, PNFOM and $\eta_{DC\text{-}RF}$ are the best among the published planar resonator based VCOs in our frequency band of interest, to date. In VCO design-2, a novel double negative active metamaterial planar structure is proposed as a resonator. Metamaterial resonator is analyzed and composite complex constituent parameters are extracted. Metamaterial resonator has an improved quality factor compare to the resonator proposed in the design-1. The IC was fabricated and tested. Measurements show 10.37dBm power at 14.3GHz which is improved compare to the VCO design-1.

Acknowledgments

I am indebted to my supervisor Prof. Sanjeev Gupta and co-supervisor Prof. Deepak Ghodgaonkar for accepting me as a doctoral student and allowing me to join their resea group. By means of the courses and research projects, they introduced me to advance topics like Wireless Systems Design, Advanced Radio Wave Propagation and Metamaterials in microwave applications that laid a strong technical foundation of my research work. Their unique motivating capability to be on the front line of the research kept me aware of the advancements. They have always provided me with the required resources and guidance, without which this research could not have been possible. Their leadership skills and result-oriented nature have created deep impression in my mind, and will continue to inspire me for the rest of the life.

I am grateful to Prof. V.P Sinha for his continuous encouragement and mentoring throughout the years. In earlier years of the programme, his insightful directions lead me motivated to work in the advancements in the field of my interest.

I sincerely thank to my Research Progress Committee members; Prof. Mukesh Tiwari, Prof. Vijaykumar Chakka, Prof. Bhaskar Chaudhury, and Prof. Anjan Ghosh for channelizing my efforts and spending their valuable time. Especially, I thank to Prof. Mukesh Tiwari for the knowledge gained from him through the long interactions during the teaching assistanceship under him for the course of Electromagnetic Theory, which helped me a lot during the tenure of my research.

I thank my synopsis review committee members; Prof. V. P. Sinha, Prof. Mukesh Tiwari, and Prof. Bhaskar Chaudhuri, for spending the time, reviewing my synopsis and providing valuable guidance to improve thesis.

Most importantly, I thank Deputy Director, Shri Tapan Misra, Group Head, Shri Ch V N Rao and scientists, Mr/Ms Shruti Kavdia, Harshita Tolani, Nidhi Singh, Samidha Jain, Anil Gupta, Ravi Khatri and Nitesh Sharma at Microwave Sensors Receiver Division

(MSRD), Microwave Sensors Trans-receiver Group (MSTG), Space Application Centre (SAC), Indian Space Research Organization (ISRO) for providing the opportunity to work in their lab and providing necessary facilities for the fabrication and testing throughout the process.

I thank Dr. M. R. Patel, Director, Innovative Instruments, Baroda for his support in providing me the components required for some of the designs.

I acknowledge the DA-IICT Resource Centre for ensuring to be the best library, information and reference services which has played an important role in my work.

The staff members at DA-IICT have provided lot of help and support. Lab assistants, faculty secretaries, help desk and administration staff have always helped me in various issues. I acknowledge their kind co-operation.

At last but definitely not the least, I thank my family that has been my driving force. With unconditional love, I am always ensured emotional, financial and any other kind of support that I needed in my pursuits. I understand and acknowledge every one for all the compromises and sacrifices done to ease my efforts. I cannot thank my family enough for providing me a strong base on which I could stand still and was able to complete this work.

Table of Contents

List of Figures

List of Tables

Chapter 1

Introduction

Receiver system is an important part of the communication channel. Receiver front-end architecture includes LNA, RF filter, mixer, IF filter and LO.

Satellites play unique part of the daily routine life by providing voice, video and data applications. Exponential growth of satellite communications in wide range of commercial and daily routine applications like satellite radio, television and Direct-To-Home (DTH) broadcasting services using Fixed Service Satellites (FSS) and Direct Broadcast Satellites (DBS), digital cinema, broadband internet connections, weather forecast, geographic observations like agriculture, forestry and geology, military communication and control applications, etc have always motivated the researchers. Satellite receiver is one of the backbone systems in satellite communication channel.

Any satellite uplink or downlink signal travels considerably long distance and gets contaminated by the channel noise before it reaches to the receiver. As the signal attenuates significantly (more than 150dB), the received signal power is so less that the signal seems almost immersed in the noise floor. Hence, it becomes interestingly challenging to process such weak signals received by the receiver. The work presented here describes the analysis and design of novel receiver front-end for Ku-band scatterometer for Indian weather satellite OceanSat-3. Like many other bands, Ku-band is also identified for the satellite communications as the atmosphere provides below 0.08dB/km absorption in Ku-band (considering worst case– at sea level) [1]. Fig. 1.1 shows the typical receiver front-end architecture which is applicable to satellite receivers also.

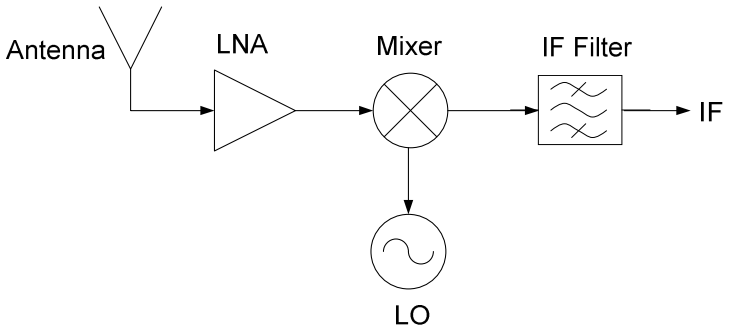

Fig. 1.1. Typical receiver front-end architecture

1.1 Organization of the thesis

The work presented here is organized in the following way. The relevant theory and literature survey for the LNA, mixer and LO is carried out and presented in chapter 2.

In chapter 3, Ku-band three-stage low noise amplifier is designed and analyzed. Analysis is carried out for the multistage design in order to minimize the noise figure. Circuit input referred noise is analyzed using resistor temperature noise sources, and intrinsic and extrinsic parameters of the sixteen element GaAs HEMT device. Both the low noise amplifiers are fabricated and tested in Ku-band.

In chapter 4, we have presented a modified small size rat-race coupler for the mixer application. This chapter focuses on Ku-band mixer design to achieve linear and wideband response. Two-stage multiband-reject IF filter is designed and simulated to suppress the unwanted intermodulation products.

Chapter 5 describes the design and analysis of low power low phase noise VCOs as LO. Two different new topologies of the negative resistance VCOs at Ku-band are proposed. Novel resonators for the oscillators are proposed in order to achieve better phase noise performance. The circuits are fabricated and measurement results are presented.

Chapter 6 describes the conclusions and the suggestions for the future work. Appendix A describes the abstract noise representation of the system with cascaded low noise amplifier. While appendix B focuses on the detailed resistor temperature noise representation considering the device distributed model for the three-stage LNA.

Chapter 2

Theory and Literature Survey

2.1. Low noise amplifier

Low noise amplifier is the most important building block of the communication channel. As it is placed just after an antenna, according to Friis formula, LNA's noise figure dominates over the noise figure of the following stages. The noise factor of the cascaded system F_{syst} is given by, [2]

$$F_{syst} = F_1 + \frac{F_2 - 1}{G_1} + \frac{F_3 - 1}{G_1 G_2} + \frac{F_4 - 1}{G_1 G_2 G_3} + \ldots \quad \ldots\ldots (1.1)$$

Where, F_i= Noise factor of the i^{th} stage

G_i= Gain of the i^{th} stage

i=1,2,3,…

The LNA receives very weak signals and amplifies them with considerable gain and extremely low noise to preserve the required Signal to Noise Ratio (SNR) as well as to improve the receiver sensitivity. LNA challenging design trade-offs to be taken care off are: gain and input matching vs. noise figure, linearity vs. noise figure, stability vs. noise figure, etc.

The stability of the amplifier is very important consideration in the design. Stability implies the resistance of an amplifier to oscillate. The conditions for the unconditional stability in terms of reflection coefficients (as defined in Fig. 2.1) can be written as, [3]

$$|\Gamma_S| < 1 \quad \ldots\ldots (1.2)$$

$$|\Gamma_L| < 1 \quad \ldots\ldots (1.3)$$

$$\left|\Gamma_{IN}\right| = \left|S_{11} + \frac{S_{12}S_{21}\Gamma_L}{1 - S_{22}\Gamma_L}\right| < 1 \qquad \ldots\ldots (1.4)$$

$$\left|\Gamma_{OUT}\right| = \left|S_{22} + \frac{S_{12}S_{21}\Gamma_S}{1 - S_{11}\Gamma_S}\right| < 1 \qquad \ldots\ldots (1.5)$$

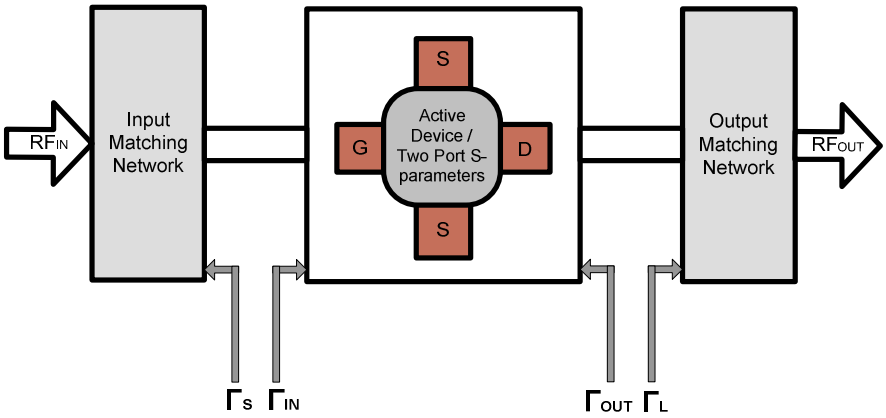

Fig. 2.1. Typical single stage amplifier

The amplifier shows negative resistance at the corresponding port (refer Fig. 2.1) if the reflection coefficient in any of the equations (1.2)–(1.5) is greater than 1. Negative resistance leads to unstability and oscillations. This negative resistance can be compensated by applying appropriate additional external resistor at the corresponding unstable port. Stability of the amplifier can be ensured if the source and load stability circles are not intersecting the Smith chart. Source stability circle (r_S,C_S) and load stability circle (r_L,C_L) can be plotted as, [3]

$$r_S = \left|\frac{S_{12}S_{21}}{\left|S_{11}\right|^2 - \left|\Delta\right|^2}\right|, \; C_S = \frac{\left(S_{11} - \Delta S_{22}^*\right)^*}{\left|S_{11}\right|^2 - \left|\Delta\right|^2} \qquad \ldots\ldots (1.6)$$

$$r_L = \left|\frac{S_{12}S_{21}}{\left|S_{22}\right|^2 - \left|\Delta\right|^2}\right|, C_L = \frac{\left(S_{22} - \Delta S_{11}^*\right)^*}{\left|S_{22}\right|^2 - \left|\Delta\right|^2} \qquad \ldots\ldots (1.7)$$

Unconditional stability will give stability factor K>1 and |Δ|<1. [3]

where,

$$K = \frac{1 - |S_{11}|^2 - |S_{22}|^2 + |\Delta|^2}{2|S_{12}S_{21}|} \quad \ldots\ldots (1.8)$$

$$\Delta = S_{11}S_{22} - S_{12}S_{21} \quad \ldots\ldots (1.9)$$

Once the device is made stable, the simultaneous conjugate reflection coefficient solutions Γ_{MS} and Γ_{ML} are to be presented at the input and the output port for the case of power amplifier. [3]

where,

$$\Gamma_{MS} = \frac{B_1 \pm \sqrt{B_1^2 - 4|C_1|^2}}{2C_1} \quad \ldots\ldots (1.10)$$

$$\Gamma_{ML} = \frac{B_2 \pm \sqrt{B_2^2 - 4|C_2|^2}}{2C_2} \quad \ldots\ldots (1.11)$$

$$B_1 = 1 + |S_{11}|^2 - |S_{22}|^2 - |\Delta|^2 \quad \ldots\ldots (1.12)$$

$$B_2 = 1 + |S_{22}|^2 - |S_{11}|^2 - |\Delta|^2 \quad \ldots\ldots (1.13)$$

$$C_1 = S_{11} - \Delta S_{22}^* \quad \ldots\ldots (1.14)$$

$$C_2 = S_{22} - \Delta S_{11}^* \quad \ldots\ldots (1.15)$$

However for the low noise amplifier, the input port has to be noise matched instead of power match. The optimum value of the reflection coefficient presented at the input port will result into minimum noise figure at the cost of reduced gain. Analysis of the optimum reflection coefficient requires the knowledge of input referred noise. Input referred noise can be represented in terms of device intrinsic and extrinsic parasitics. Hence the analysis of the minimum noise figure requires parasitic extractions.

Selection of the device used in LNA plays a crucial role. At high frequencies, High Electron Mobility Transistor (HEMT) devices are preferable. A simple microwave HEMT temperature dependent noise model was demonstrated in [4]. Minimum noise temperature and optimal source impedance minimizing noise measure was derived. For the same, three types of noise representations were considered in [4]:

1. Y-matrix representation: G_1, G_2, ρ_c

   where,

$$G_1 = \frac{\overline{|i_1|^2}}{4kT_0\Delta f},\ G_2 = \frac{\overline{|i_2|^2}}{4kT_0\Delta f},\ \rho_c = \frac{\overline{i_1^* i_2}}{\sqrt{|i_1|^2\,|i_2|^2}} \qquad \ldots\ldots (1.16)$$

where,

G_1 and G_2 are the input and output conductances respectively

ρ_c = noise correlation coefficient

i_1,i_2 are the current noise sources at input and output respectively

k = Boltzmann's constant

Δf = incremental BW

T_0 = standard temperature in Kelvin

2. ABCD-matrix representation: R_n, g_n, ρ_c

   where,

$$R_n = \frac{\overline{|e_n|^2}}{4kT_0\Delta f},\ g_n = \frac{\overline{|i_n|^2}}{4kT_0\Delta f},\ \rho_c = \frac{\overline{e_n^* i_n}}{\sqrt{|e_n|^2\,|i_n|^2}} \qquad \ldots\ldots (1.17)$$

where,

e_n and i_n are input refereed voltage and current noise sources respectively

R_n and g_n are the input noise resistance and input noise conductance respectively

3. Representation in terms of noise temperature T_n, optimal source impedance Z_{opt}, and noise conductance g_n

   For generator impedance $Z_g = R_g + jX_g$, and minimum noise temperature T_{min},

$$T_n = T_{\min} + T_0 \frac{g_n}{R_g}\left|Z_g - Z_{opt}\right|^2,\ \Gamma_{opt} = \frac{Z_{opt} - Z_0}{Z_{opt} + Z_0} \qquad \ldots\ldots (1.18)$$

where, Γ_{opt} = optimum value of reflection coefficient leading to minimum reflection coefficient

While [5] discusses the noise parameter modelling of HEMT and Metal-Semiconductor Field Effect Transistor (MESFET) considering resistor temperature noise sources. The model proposed was based on the three uncorrelated noise sources located at the intrinsic transistor, which were assumed to show white spectral behaviour.

Methods of analysis for the device behavior can be broadly classified in two parts. First is the load-pull measurement technique. It uses the load-pull set up, in which load impedances are varied considering the available power, in order to understand the device behavior as a function of frequency. Second is the cold FET technique. It requires the S-parameter measurements of the device in cold-state (off-state) by driving the device gate below threshold voltage.

Two-port equivalent circuit of the GaN HEMT with intrinsic and extrinsic parameters is studied in [6]. Using measured noise parameter and scattering parameter data, gate and drain noise sources were determined. Three noise mechanisms were identified and studied, namely, those due to velocity fluctuation, gate leakage, and traps.

While in [7] another method was proposed for large signal model extraction. The large signal model is based on small signal models derived at different bias conditions. A low gate bias parameter extraction was proposed in [7] which does not require to bias gate at a higher voltage to extract the parameters, especially parasitic inductance and resistance.

A new parameter extraction approach was presented in [8], [9]. Extraction was carried out by identifying high quality initial parameter values derived from cold S-parameter measurements and then applying them to the optimization algorithm.

The typical noise parameters including minimum noise figure (NF_{min}), noise equivalent resistance (R_n), optimum source reflection coefficient (Γ_{opt}) and associate gain (G_a) at different temperatures were measured and their dependencies on temperature were modeled by a linear or a quadratic approximation and presented in [10]. While, nonlinear large signal

scalable model was developed by revising Angelov (Chalmers) model and it was discussed in [11].

However, all of the referred literature presents the noise analysis and parameter extraction for the device only. We have taken further the cited work to analyze the noise extending to the circuit level from the intrinsic device level. We have represented the input referred noise in terms of extracted parameters, and then the conditions are analyzed in order to achieve the minimum noise figure.

2.2. Mixer

Mixer mixes RF signal coming from LNA with the LO signal in order to generate the IF. Fig. 2.2 shows the typical singly balanced passive mixer [12]. Mixer uses 90º or 180º 3dB coupler to combine the RF and LO signals. Output of the coupler is fed to the pair of anti-parallel diodes. Nonlinear operation of the diode is driven by the LO power as typically, the LO power dominates over RF power. L_1 and L_2 are the inductors to provide DC return for the diodes. Mixing operation generates ideally infinite order intermodulation frequency terms, in general ($\pm nf_{RF} \pm mf_{LO}$) where n and m are the integer numbers. However the desired term is only the f_{IF}, which is $|f_{RF} - f_{LO}|$. L_f and C_f are the low pass IF filter components to extract out the desired IF from the intermodulation products.

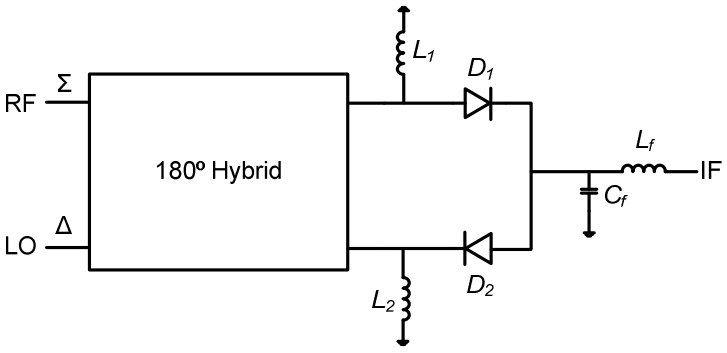

Fig. 2.2. 180º singly balanced passive mixer. The diodes D_1 and D_2 can be unmatched diodes or complete, individual, single-diode mixers. The mixer can be configured with either the sigma or delta port as the RF; the other is the LO [12]

In Fig. 2.3(a), consider the equivalent model for the mixer shown in Fig. 2.2. As RF is applied to Σ-port of the 180º hybrid, RF signal (V_{RF}) coming to the diode is in phase. While

LO is applied to Δ-port, hence, LO signal (V_{LO}) is 180º out of phase at the output ports of the hybrid. Locally generated oscillator signal has the noise components (V_n) present which enter through the port in the similar way as the LO signal. However, no external dc bias is applied and the diodes are driven by the signal power only in the case of passive mixers. Fig. 2.3(b) shows LO power driven diodes configuration. It can be seen that the LO noise is 180º out of phase, and gets cancelled at the IF. Hence, perfectly balanced coupler design in the mixer ensures LO noise cancellation. Mixer port isolations and wide bandwidth also directly depend on the coupler design. Hence, coupler plays a crucial role in the microwave mixers.

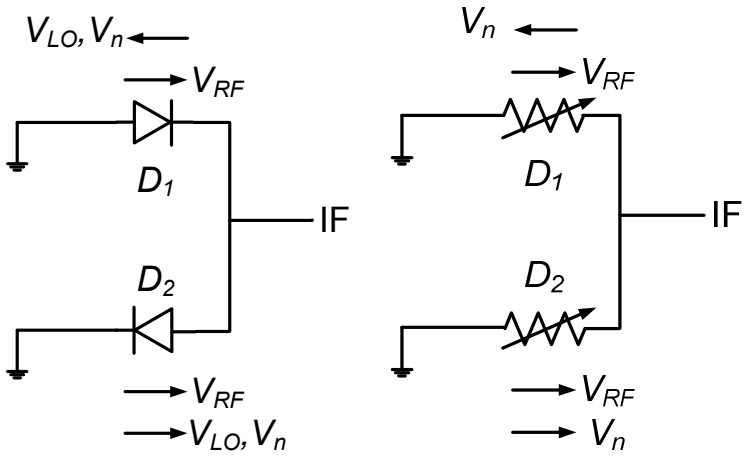

(a) (b)

Fig. 2.3. (a) Mixer equivalent presentation (b) LO noise cancellation [13]

Conventional couplers may be divided into two categories: coupled-line couplers (backward, forward) and tight-couplers (e.g., branch line, hybrid ring, and so forth). While the former are limited to loose coupling levels (typically less than –3 dB) because of the excessively small gap required for tight coupling, the latter are limited in bandwidth (i.e., typically less than 20%). [14]

After Veselago [15] conceptualized and proposed double negative left handed structures in 1968 which was later experimentally verified by Smith, et al. [16] and Shelby, et al. [17] in 2000 and 2001 respectively, it opened up an interesting emerging field of research in unconventional metamaterials. Later, Planar distributed structures, which support left-

handed (LH) waves were presented and their negative refractive index (NRI) properties were shown theoretically, numerically, and experimentally in [18].

However, the use of couplers is often problematic as many wireless systems operate in two frequency bands or operate in wideband, and thus require dual-band or wideband components, such as the use of two hybrid ring couplers. Furthermore, the need for small and light-weight systems lead to the desire to employ compact components in front-end systems. The operating frequency and the physical dimensions of the structure make it challenging to design a compact dual-band component based on conventional methodology. Compact dual band metamaterial based hybrid ring coupler was proposed in US patent [14, Dec. 2011] by Itoh, et al. However, the designed coupler uses lumped inductors and lumped capacitors in left hand transmission line. All the four ports have equal splitting as shown in Fig. 2.4.

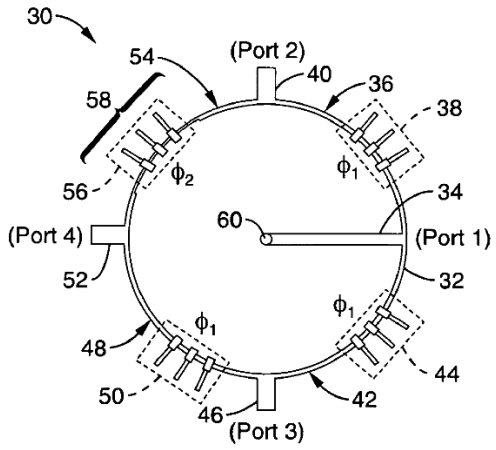

Fig. 2.4. Metamaterial based rat-race coupler proposed in [14]

Similar is the case in [19] where wideband small size coupler using slow wave structure and metamaterial was analyzed and designed at 2GHz. Slow wave structure lines are designed for three of the four branches in the coupler as shown in Fig. 2.5(a). While, miniaturized metamaterial line is placed as a forth branch of the coupler as shown in Fig. 2.5(b). At the design frequency of 2 GHz, the size of the proposed coupler is about 2.0 cm X 2.0 cm. In addition, the phase balance bandwidths based on $\angle S_{21} - \angle S_{31}$ ($0^o \pm 10^o$) and $\angle S_{24} - \angle S_{34}$ ($180^o \pm 10^o$) were 150 and 125% respectively.

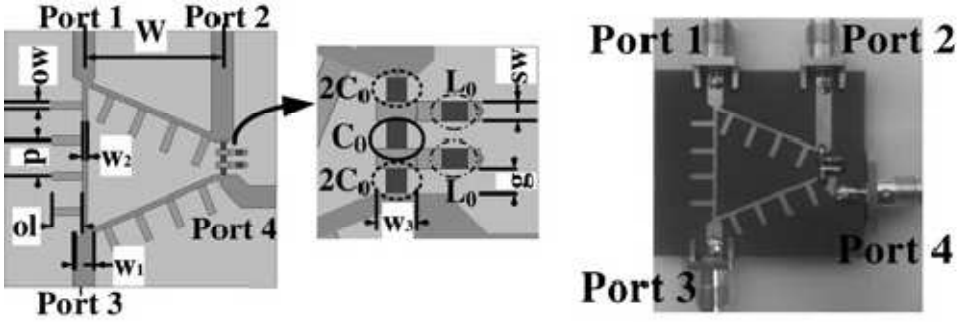

(a) (b)

Fig. 2.5. Rat-race coupler using slow wave lines in [19] (left three lines) and meta-line (right one line) (a) Layout (b) Fabricated rat-race coupler

Novel, miniaturized dual-band symmetric directional coupler using composite right/left-handed transmission structures was analyzed for dual-band at 1GHz and 2GHz in [20], the same is shown in Fig. 2.6. Designed dual-band 90° and 180° hybrids achieved 10% and 43.7% size reduction, respectively, compared to conventional microstrip couplers. In addition, the fabricated 180° hybrid was shown to have enhanced bandwidth performance in both isolation and 3dB magnitude balance.

A coupled line coupler in 1.7–2.5GHz range with circular split ring resonators etched out in the ground plane was discussed in [21] as shown in Fig. 2.7. The results of simulation and measurement showed that the coupler achieved a high degree of coupling (nearly 3-dB coupling) over a wide frequency band (38.1% relative bandwidth).

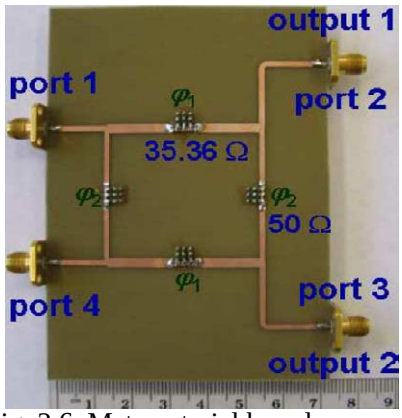

Fig. 2.6. Metamaterial based compact dual-band 90° hybrid coupler in [20]

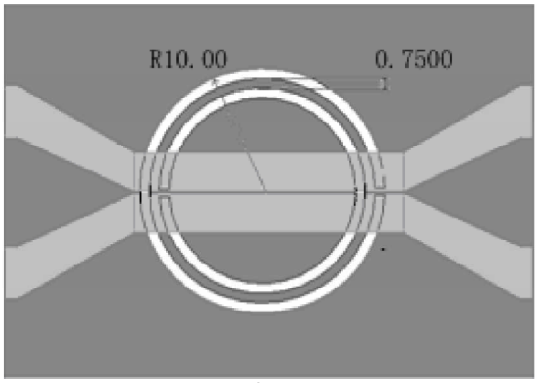

Fig. 2.7. Structure of Complementary Split Ring Resonator (CSRR)-based directional coupler in [21]

Similarly, symmetrical coupled line direction coupler based on four cascaded unit cells of square split ring resonators was analyzed and designed in [22]. Other kinds of mixer design aspects are also noted, like in [23] single-balanced diode mixer exploiting cellulose-based materials was discussed.

2.3. Local oscillator

Local oscillator contributes as an important building block in the communication systems. In receiver, it generates a frequency offset from the RF in order to produce IF using mixer. LO should provide the stable frequency with required output power.

The theory and design of oscillators can also be approached using the negative resistance method. If an active device is used to supply an amount of energy equal to the energy dissipated, the circuit can sustain oscillations. The behavior of the active device can be represented by a negative resistance in series with a reactance, as shown in Figure 2.8. [24]

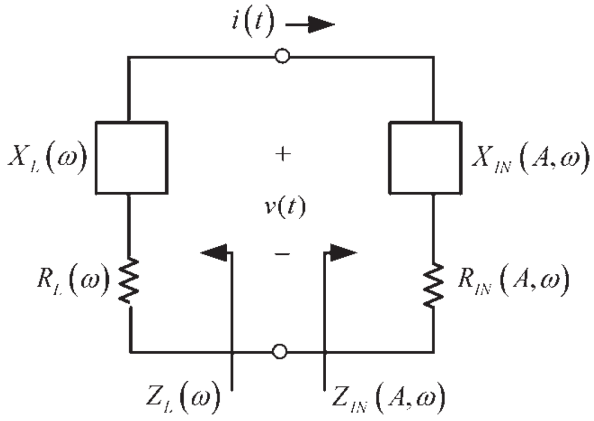

Fig. 2.8. Negative resistance model for an oscillator [24]

The impedance of the negative-resistance active device is represented by,

$$Z_{IN}(A,\omega) = R_{IN}(A,\omega) + jX_{IN}(A,\omega)$$
$$\textit{where, } R_{IN}(A,\omega) < 0 \qquad \ldots\ldots (1.19)$$

The oscillator is constructed by connecting the active device to the passive impedance, which is given by,

$$Z_L(\omega) = R_L(\omega) + jX_L(\omega) \quad \ldots\ldots (1.20)$$

If $R_{IN}(A,\omega) + R_L(\omega) > 0$ then the circuit will not oscillate. [24]

The start of the oscillation condition is given by, [24]

$$R_{IN}(A,\omega) + R_L(\omega) < 0 \quad \ldots\ldots (1.21)$$

The circuit will oscillate at the frequency (ω_0) and amplitude (A_0), where, [24]

$$Z_{IN}(A_0,\omega_0) + Z_L(\omega_0) = 0 \quad \ldots\ldots (1.22)$$

Hence, $R_{IN}(A_0,\omega_0) + R_L(\omega_0) = 0$ and $X_{IN}(A_0,\omega_0) + X_L(\omega_0) = 0$

The sustained oscillations can be ensured by Nyquist stability test and checking the Kurokawa condition [24]. The Nyquist test can be applied to analyze the function $1 - \Gamma_{IN}(j\omega)\,\Gamma_L(j\omega)$ by determining the encirclements of the point $\Gamma_{IN}(j\omega)\,\Gamma_L(j\omega) = 1$, where, Γ_{IN} corresponds to Z_{IN} and $\Gamma_L(j\omega)$ corresponds to Z_L [24]. Kurokawa condition [25] is given as,

$$\left.\frac{\partial R_{IN}(A)}{\partial A}\right|_{A=A_0} \left.\frac{dX_L(\omega)}{d\omega}\right|_{\omega=\omega_0} - \left.\frac{\partial X_{IN}(A)}{\partial A}\right|_{A=A_0} \left.\frac{dR_L(\omega)}{d\omega}\right|_{\omega=\omega_0} > 0 \quad \ldots\ldots (1.23)$$

As VCO provides the frequency tunability in order to generate the required IF, low phase noise VCO is used as a LO in our case. Phase noise of the oscillator depends on the resonator used in it. Hence, resonator design plays an important role in the oscillator design. Any oscillator requires high-Q resonator in order to achieve low phase noise and so frequency stability. At high frequencies, dielectric resonators are preferred as they have very high-Q. But, one of the drawbacks of the dielectric resonator oscillator is, they are bulky in size. Introducing small size planar resonators in the circuit rather than the conventional dielectric resonators, drastically reduces the cost of fabrication and time to market.

The published works cite different VCO topologies with various resonator structures. Such as, simultaneously small size, low phase noise, low DC power consumption and low thermal drift VCO was designed and discussed in [26]. VCO operating around 3.4GHz was discussed, which uses a varactor diode at the emitter of a bipolar transistor as shown in Fig. 2.9.

A method for the design of a low phase-noise planar oscillator based on a compact low-noise active elliptic filter for its frequency stabilization was presented and discussed in [27]. The phase noise of the oscillator was significantly reduced by taking advantage of the low-noise characteristics of the active filter shown in Fig. 2.10. The filter occupies a relatively small area, making it suitable for the fabrication of very compact low phase-noise oscillators. The oscillator, operating at 8.1 GHz, achieves a measured phase-noise of –150 dBc/Hz at 1 MHz frequency offset with 10 dBm output power. But it requires 160mW of dc power resulting in low dc to RF efficiency (6.5%).

Similar way, as shown in Fig. 2.11, the four pole bandpass elliptic filter for oscillator was proposed in [28]. At the oscillation frequency of 8.05 GHz, the measured phase noise is –122.5 dBc/Hz at 100 KHz offset frequency. The oscillator exhibits an output power of 3.5 dBm with dc to RF efficiency of 10%.

Now instead of passive filters, active elliptic filter (Fig. 2.12) was presented as a resonator in [29]. The oscillator, operating at 8 GHz, shows a measured phase noise of –150 dBc/Hz at 1-MHz frequency offset with 10-dBm output power.

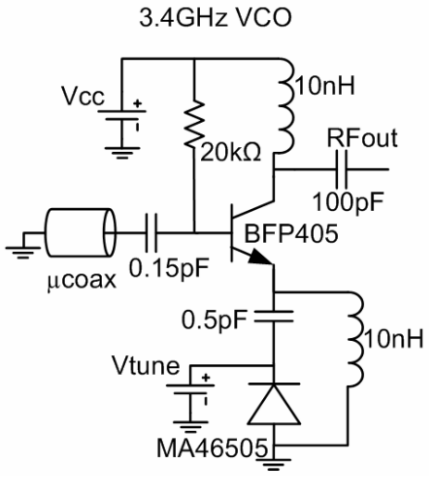

Fig. 2.9. Circuit diagram of the 3.4GHz VCO in [26]

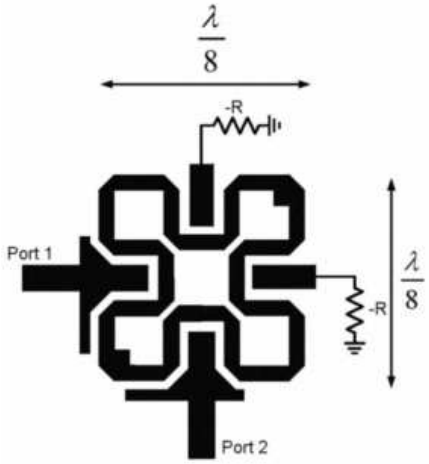

Fig. 2.10. Compact elliptic filter structure as a resonator for oscillator, proposed in [27]

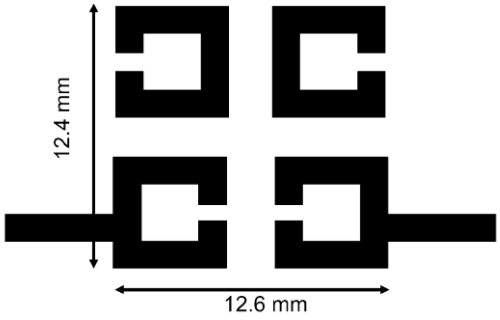

Fig. 2.11. Four-pole elliptic filter as a resonator for oscillator, proposed in [28]

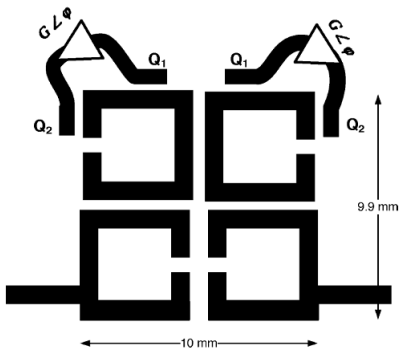

Fig. 2.12. Active four-pole elliptic-response bandpass filter designed for low phase-noise oscillator applications. [29]

An X-band VCO was designed by employing a compact tunable high-Q negative-resistance resonator and presented in [30] (Fig. 2.13). The fabricated VCO operates at 8.2 GHz with 105 MHz tuning range.

Similarly, a harmonic voltage controlled oscillator using planar hairpin resonator structure as shown in Fig. 2.14, was designed and presented in [31]. It has 5dBm output power at 11.17GHz with 6V varactor bias.

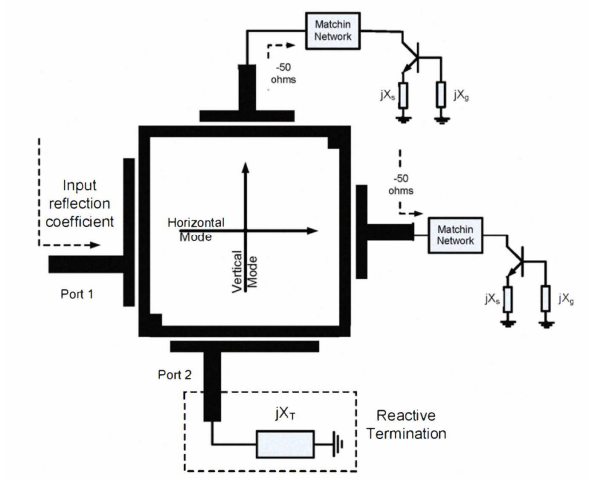

Fig. 2.13. A reactively terminated dual-mode active filter used as a high-Q negative-resistance resonator for oscillator designs. [30]

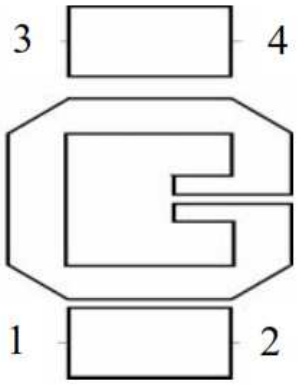

Fig. 2.14. Hairpin resonator layout with two 50Ω coupled microstrip lines. [31]

The Multi-Coupled Line Resonator (MCLR) based oscillator/VCO was discussd in [32]. MCLR is promising alternative of dielectric resonators, and supports better noise performance than commercial available high *Q* (quality factor) dielectric resonators.

While in [33], a low phase noise X-band push-push VCO with microstrip resonator is discussed. The measured oscillation frequency was from 9.166 GHz to 9.583 GHz. The peak output power of the push-push VCO was –10dBm.

A low phase-noise oscillator using a microstrip trisection bandpass filter (shown in Fig. 2.15) was designed, fabricated, and experimentally verified in [34]. The trisection filter is mainly treated as a frequency stabilization element, and then embedded into the feedback loop of the oscillator. The oscillation frequency of the oscillator was designed at 2.46 GHz, and the measured phase noise is –144.47 dBc/Hz at 1 MHz offset frequency. Moreover, the developed VCO has a frequency turning range from 2.497 to 2.537 GHz. Over this frequency range, the measured phase noise is from –127.47 to –138.47 dBc/Hz at 1 MHz offset frequency.

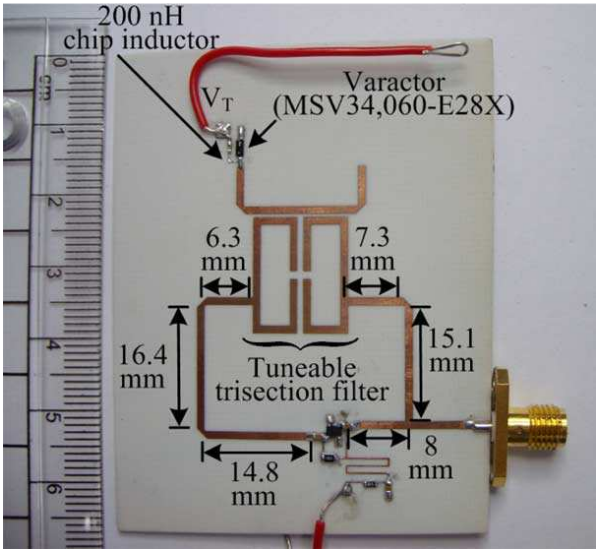

Fig. 2.15. A feedback oscillator using microstrip bandpass trisection filter [34]

A wideband VCO using microstrip combline bandpass filters is presented in [35]. The developed oscillator with the three-pole combline filter was experimentally demonstrated at 2.05 GHz with –148.3-dBc/Hz phase noise at 1-MHz offset frequency. The developed VCO

has a frequency tuning range from 1.3 to 2.2813 GHz with a 54.8% bandwidth. Over this frequency range, all the phase noises measured at 1-MHz offset frequency are better than –117.19 dBc/Hz.

A low phase-noise microwave oscillator (Fig. 2.16) based on a hairpin-shaped resonator (HSR) using a composite right/left-handed transmission line (CRLH TL) was proposed and analyzed in [36]. The HSR consists of the conventional transmission line (CTL) and the CRLH TL. The proposed HSR has a very compact size of $0.105\lambda_g$ X $0.19\lambda_g$. An oscillator based on the HSR was designed, fabricated and measured. At the oscillation frequency of 4.95 GHz, the measured phase noise is –120.5 dBc/Hz at 100 kHz offset with 4.93 dBm output power.

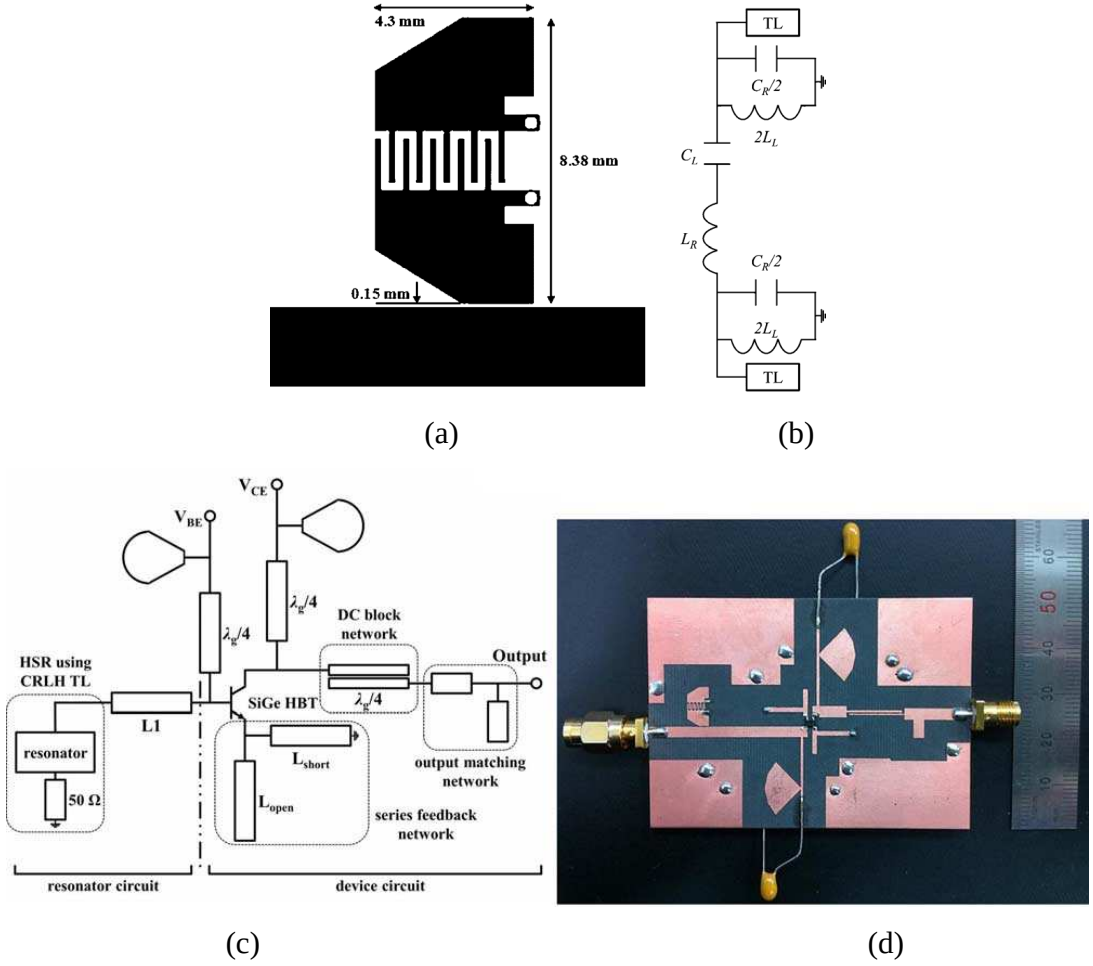

Fig. 2.16. (a) Hairpin shaped resonator (HSR) layout (b) HSR equivalent circuit (c)Microwave oscillator circuit schematic based on HSR (d) fabricated oscillator. [36]

Chapter 3

Low Noise Amplifier

This section describes the design and analysis of the three-stage LNA. The aim is to analyze, design and improve the performance parameters of three-stage LNA. We have presented a cumulative approach of two-port modelling and noise extraction. We have extended the work to the multistage circuit level analysis from the device level analysis– using Y-matrix representation (G_1, G_2, ρ_c) [4], and noise parameter modeling using resistor temperature noise sources [5] (as discussed in section 2.1). Two-port multistage analysis is carried out. The work presents the extraction of noise, considering intrinsic and extrinsic parameters. We have modeled and analyzed the input referred noise of the LNA in order to minimize the noise figure. For the same, sixteen-element device distributed model with all possible inherent resistor temperature noise sources are considered in the analysis. We have analyzed the LNA considering gain-constrained-noise optimization, extrinsic device parasitics, stability resistor and matching networks to the next stage for the multistage design considerations. We fabricated and tested two different designs of the LNA. In design-1, we analyzed the typical single stage LNA and then extended the same for the three-stage design. In design-2, we minimized the input referred noise by making the correlated noise ideally zero. We considered stability-gain-noise figure trade off and the gain constrained noise optimization. Results are presented showing the improvements in the design-2 over design-1. However, the improved design-2 results are also compared extensively with the relevant work published in the Ku-band LNA. It was found that the final design has the simultaneously better performance parameters compared to the existing designs.

As the received signal by satellite on-board receiver is highly attenuated, three-stage design is considered for the high gain requirement. Fig. 3.1 shows the proposed three-stage low noise amplifier circuit. Each stage input and output impedances are mentioned.

Three-stage LNA has three active devices, two interstage matching networks, input matching network and output matching network. Input and output impedances before and after each stage are shown in Fig. 3.1. L_{11}, L_{12}, L_{13}, L_{14} along with C_{11}, C_{12} and, stub distributed elements L_{st1}, C_{st1} form an input matching network. Same way the interstage matching networks and output matching network are shown. L_{g1} to L_{g3}, C_{g1} to C_{g3} and R_{g1} to R_{g3} form the gate bias network for all three devices. Similarly, drain bias networks are shown in the figure. C_{in}, C_{out}, C_{c1} and C_{c2} are the dc blocking capacitors having Specific Resonance Frequency (SRF) at the desired RF. L_{s1} to L_{s3} are very small inductances to model the transmission lines between the device sources and the ground.

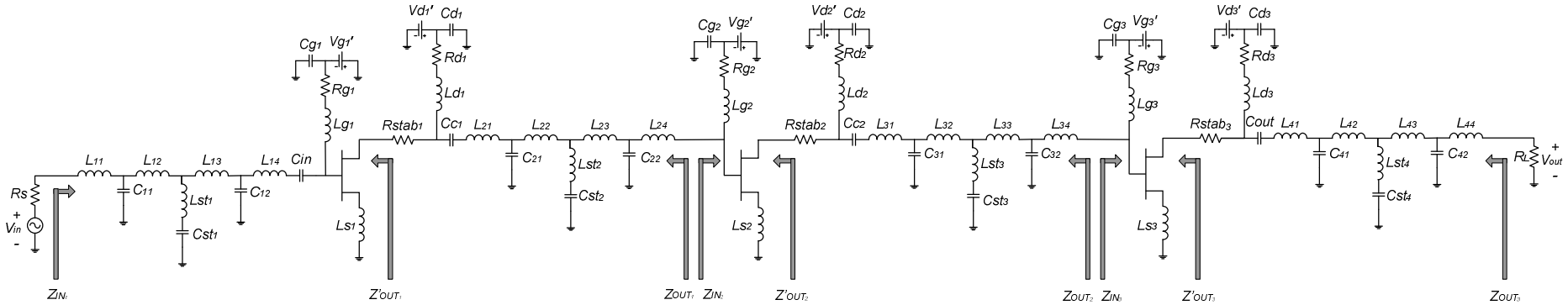

Fig. 3.1. Schematic of the analyzed three-stage Ku-band low noise amplifier

3.1. Abstract noise representation of the three-stage LNA

An adequate resistor connected to the input or output, can stabilize the amplifier. We have analyzed the noise figure considering the stability resistor. It is desirable to use stability resistor at the output stage rather than the input to avoid the noise amplification. Fig. 3.2 shows two different configurations to stabilize the low noise system. Series and shunt stability resistor are connected to the output (port-2) of the system.

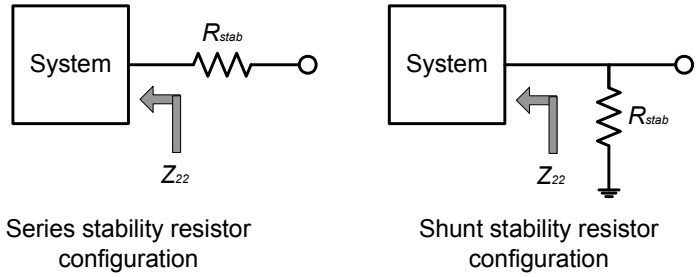

Fig. 3.2. Series and shunt stability resistor configuration

If R_{stab} is the stability resistor and if port-2 has the output impedance Z_{22} then, for series stability resistor configuration, noise factor F may be calculated as,

$$F = \frac{4kT\left(\left|Z_{22}\right| + R_{stab}\right)}{4kT\left|Z_{22}\right|} = 1 + \frac{R_{stab}}{\left|Z_{22}\right|} \quad \text{... ...(3.1)}$$

Equation (3.1) implies that the noise figure can be reduced by keeping the series stability resistor as low as possible.

While for the shunt stability resistor configuration, the noise factor may be calculated as,

$$F = \frac{1}{A_v^2}\frac{4kT\left(\left|Z_{22}\right| \| R_{stab}\right)}{4kT\left|Z_{22}\right|} = \frac{1}{A_v^2}\frac{R_{stab}}{R_{stab} + \left|Z_{22}\right|} = \left(\frac{R_{stab} + \left|Z_{22}\right|}{R_{stab}}\right)^2 \frac{R_{stab}}{R_{stab} + \left|Z_{22}\right|} = 1 + \frac{\left|Z_{22}\right|}{R_{stab}} \quad \text{..(3.2)}$$

Equation (3.2) implies that the noise figure can be reduced by keeping shunt stability resistor as high as possible.

However *series* stability resistor is considered in the design to reduce the design complexity. On the other side, shunt stability resistor requires $\lambda/4$ high impedance

transmission line (TL) (around 180µm on alumina substrate) which shows an open circuit at the desired RF and does not allow RF to bypass to the ground.

Now, we are going to analyze the noise figure in terms of gain and, input and output impedances of the each stage considering Fig 3.1. Only device channel noise is taken into account noting the fact that in device, channel thermal noise is the only dominating noise source amongst all of the others [37]. The device channel noise is given by $\overline{i_{nD}^{\,2}} = 4kT(\gamma g_m)\Delta f$ where, channel noise coefficient γ is greater than 2/3 for the short channel (<1µm) devices. [37],[38],[39]

For three-stage LNA, noise factor F may be represented as follows, (Refer to Appendix A for the analysis)

$$F = 1 + \frac{\left(\overline{I_{nD_1}^2}\left|Z'_{OUT_1}\right|^2\right)\left|\frac{R_{stab_1}}{Z'_{OUT_1}+R_{stab_1}}\right|^2 + \overline{v_{nR_{stab_1}}^2}}{\left|\frac{Z_{IN_1}}{R_s+Z_{IN_1}}\right|^2 A_{v_1}^2\,\overline{v_{nR_s}^2}} + \frac{\left(\overline{I_{nD_2}^2}\left|Z'_{OUT_2}\right|^2\right)\left|\frac{R_{stab_2}}{Z'_{OUT_2}+R_{stab_2}}\right|^2 + \overline{v_{nR_{stab_2}}^2}}{\left|\frac{Z_{IN_1}}{R_s+Z_{IN_1}}\right|^2 A_{v_1}^2\left|\frac{Z_{IN_2}}{Z_{OUT_1}+Z_{IN_2}}\right|^2 A_{v_2}^2\,\overline{v_{nR_s}^2}}$$
$$+ \frac{\left(\overline{I_{nD_3}^2}\left|Z'_{OUT_3}\right|^2\right)\left|\frac{R_{stab_3}}{Z'_{OUT_3}+R_{stab_3}}\right|^2 + \overline{v_{nR_{stab_3}}^2}}{\left|\frac{Z_{IN_1}}{R_s+Z_{IN_1}}\right|^2 A_{v_1}^2\left|\frac{Z_{IN_2}}{Z_{OUT_1}+Z_{IN_2}}\right|^2 A_{v_2}^2\left|\frac{Z_{IN_3}}{Z_{OUT_2}+Z_{IN_3}}\right|^2 A_{v_3}^2\,\overline{v_{nR_s}^2}} \qquad ...(3.3)$$

where,

R_s = Source resistor

I_{nDm} = *Effective* channel thermal noise present at the output end of the m^{th} stage device. It is a function of channel thermal noise i_{nD}.

R_{stabm} = Series stability resistor connected at the drain of the m^{th} stage

$\overline{V_{nR_{stab_m}}^2} = 4R_{stab_m}kT$ = m^{th} stage stability resistor thermal noise

Z_{INm} = m^{th} stage input impedance

Z_{OUTm} = m^{th} stage output impedance considering stability resistor and matching network

Z'_{OUTm} = m^{th} stage output impedance without considering stability resistor and matching network

A_{vm} = Unloaded m^{th} stage voltage gain

Equation (3.3) is analogous to the Friis equation (1.1). Equation (3.3) can also be extended for the multistage amplifier, in general with *m* stages. As expressed in equation (3.1), the stability resistor connected in the series at the output of the each stage contributes the additional noise of $F = 1 + R_{stab} / |Z_{22}|$ to the system's overall noise figure. However it is taken care of in equation (3.3).

3.2. Ku-band three-stage LNA design–1

For single stage amplifier topology, source and load stability circles at 2V/15mA are presented in Fig. 3.3. Source and load stability circles can be plotted using the equations (1.6) and (1.7). From the Fig. 3.3 it can be concluded that the LNA is potentially unstable.

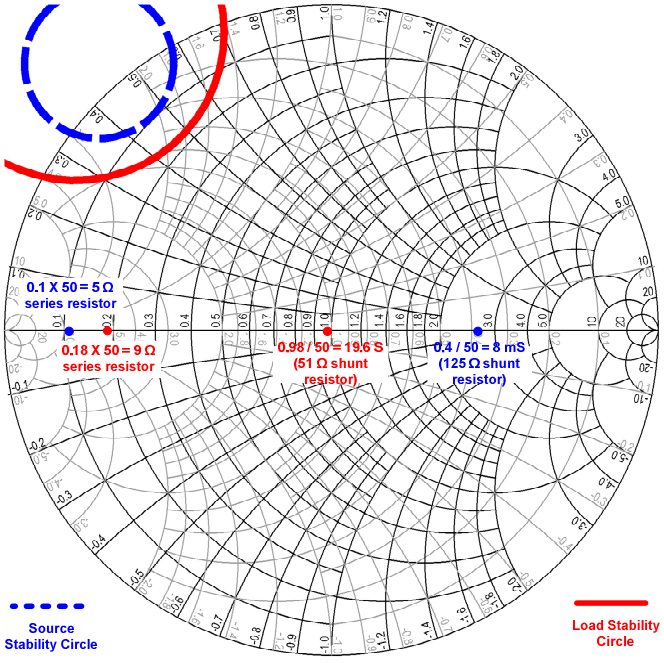

Fig. 3.3. Analyzing required stability resistor for single stage LNA

Stability analysis shows, for single stage amplifier, 9Ω output series stability resistor is enough to achieve the unconditional stability. However, 10Ω (Vishay Dale 0805 [40]) stability resistor is used in the design, in order to avoid the undesired oscillations considering fabrication tolerance and temperature variability. Single stage LNA is extended for the three-stage design. Fig. 3.4 and 3.5 show the simulated and measured S-parameter and noise figure results of the three-stage LNA. 10Ω series stability resistor is connected at the output port of the each stage in the three-stage LNA. Measurement at desired frequency (13.515GHz) show 25dB gain and 1.76dB noise figure with 90mW power consumption for three-stage design. Measured input return loss is around –7dB which is almost adequate for LNA, but further improvement is desirable. Measured output return loss is –24dB which provides robust power match at the output stage. –52dB measured isolation ensures unconditional stability and eliminates any chances of oscillation. Simulated and measured results have very good match which can be seen from the Fig. 3.4 and Fig. 3.5.

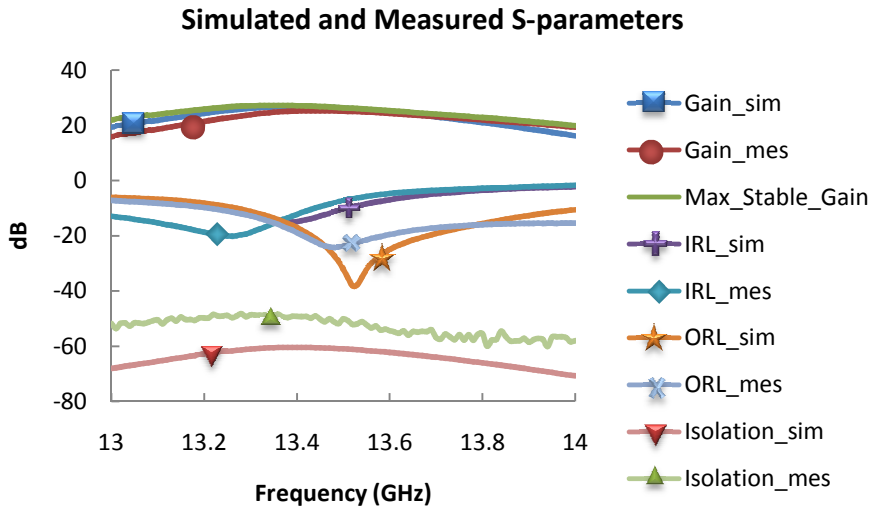

Fig. 3.4. Simulated and measured S-parameter results of Ku-band LNA (design-1)

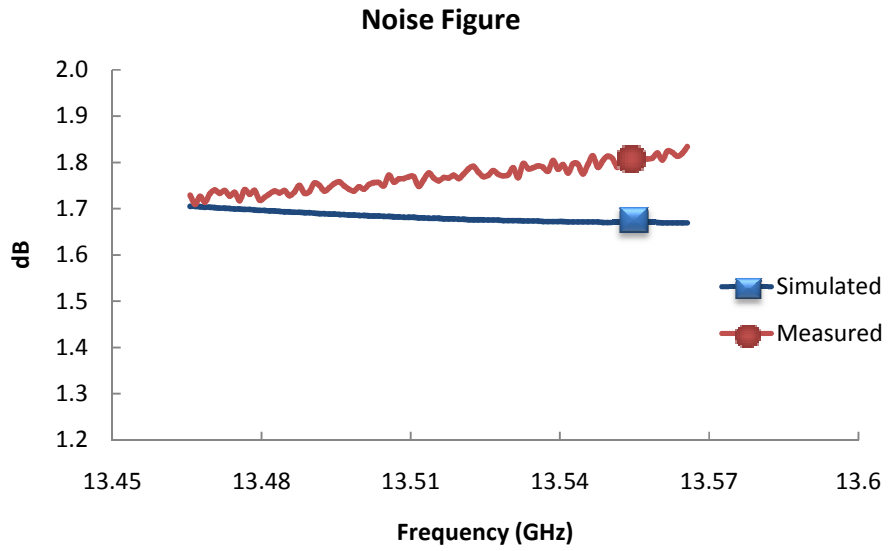

Fig. 3.5. Simulated and measured noise figure of Ku-band LNA (design-1)

Device's performance is measured on the test jig with 50Ω terminations at different bias conditions in 13–14GHz band. Fig. 3.6 and 3.7 show device gain and noise figure respectively. It was found that the device has the minimum noise figure and high gain at 3V/15mA. The device used here is the Infineon Technologies' CFY67-08P [41] Gallium Arsenide (GaAs) HEMT.

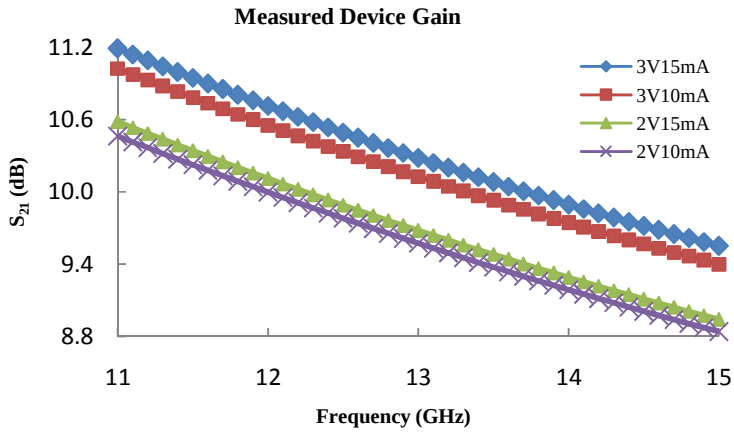

Fig. 3.6. Measured device gain vs. frequency for various operating points

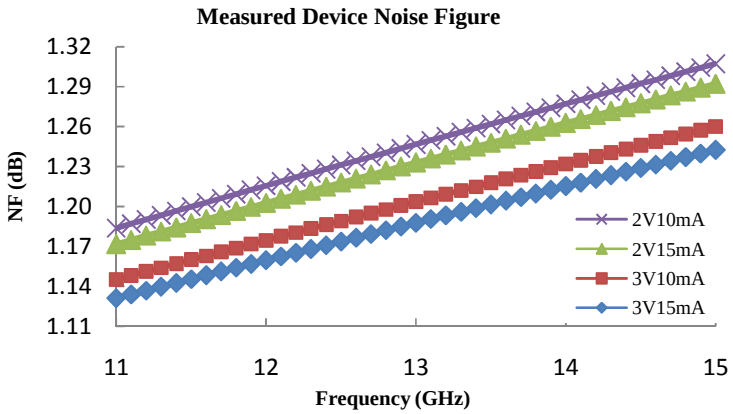

Fig. 3.7. Measured device noise figure vs. frequency for various operating points

In space, temperature changes rapidly. Consequently, the bias resistor values changes which results into fluctuations of bias operating point. Change in V_{DS}–I_D affects in the active device's high frequency performance which can be analyzed by S-parameter variations. Hence, there exist a possibility of the circuit becoming unstable and oscillating or it may at least degrade the noise and gain performance. Thus temperature change and so the bias variations have disastrous effects on the circuit's performance. The designed LNA performance is briefly analyzed in terms of the large signal and small signal nonlinear effects and presented in Fig. 3.8 to Fig. 3.17. Sensitivity analysis is carried out with respect to different parameters; operating bias V_{DS}–I_D, and input signal RF power. It is found that the proposed design is robust against the RF power variations.

Measured LNA gain at 13.515GHz as a function of each stage operating bias is presented in Fig. 3.8. It can be seen from the results that at 35mA drain current, LNA exhibits large signal gain compression by 1dB from its maximum value. However, devices in the circuits are biased at < 55mA to avoid break down and to handle P_{DC}. At 20mA, circuit shows 2dB more gain when drain is biased at 3V rather than 2V. Fig. 3.9 analyzes the effect of V_{DS} and I_D variations on the measured noise figure. In context with the Fig. 3.6 and 3.7 describing device measurements, it is understood that the circuit shows lower noise figure with 3V drain bias. NF drops to minimum possible level below 1.5dB and then again starts increasing as I_D increases. From the Fig. 3.8 and 3.9, it can be concluded that where circuit achieves better gain well before the large signal compression, minimum noise cannot be achieved. It is a gain-

noise trade-off at the same frequency. Measured gain and noise figure, as a function of frequency and operating bias, are shown in Fig. 3.10 and 3.11 respectively. As LNA is designed to operate at 13.515GHz, measurement results show excellent agreement by achieving minimum noise figure and maximum gain around the desired frequency for all the operating biases. As the input port is noise matched, gain is desirably shifted a little to achieve minimum noise. While in measurement, it is also seen that the circuit has noise figure below 1.5dB when devices are operated around 40mA at the cost of large signal gain compression resulting in nonlinearities and lower gain.

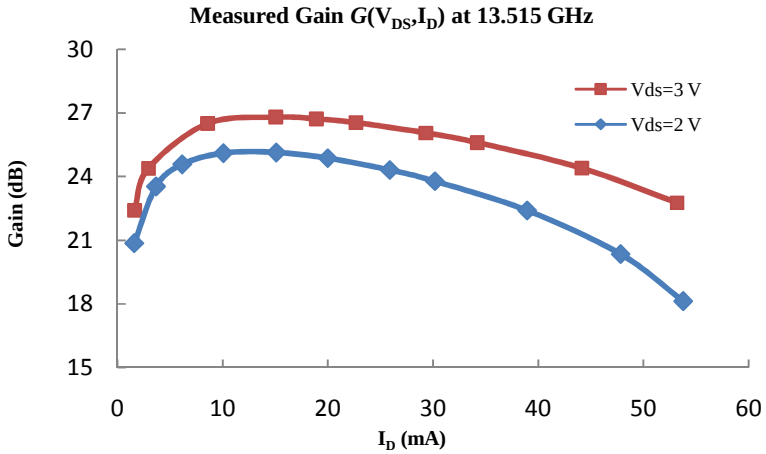

Fig. 3.8. Measured LNA gain vs. operating bias (large signal gain compression)

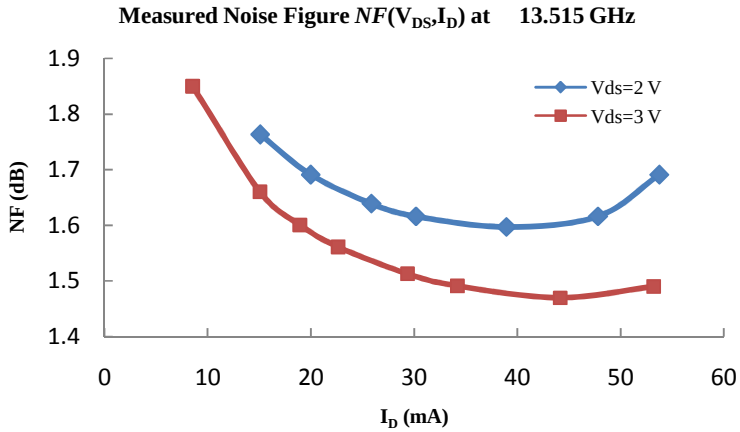

Fig. 3.9. Measured LNA *NF* vs. operating bias (Trade-off: NF_{min} cannot be achieved where gain is maximum)

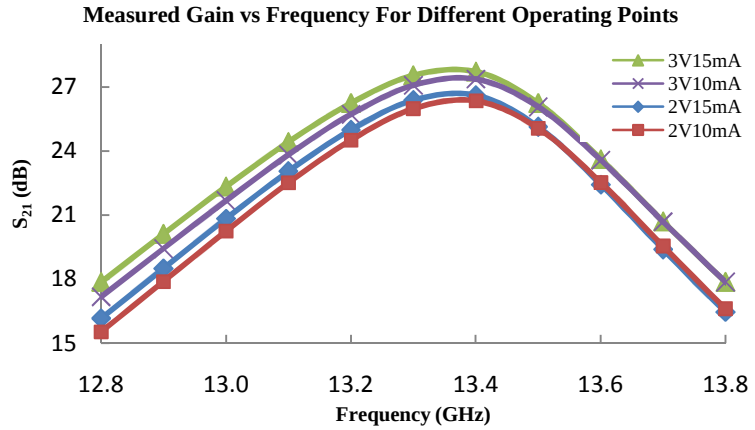

Fig. 3.10. Measured LNA gain vs. frequency for different operating points

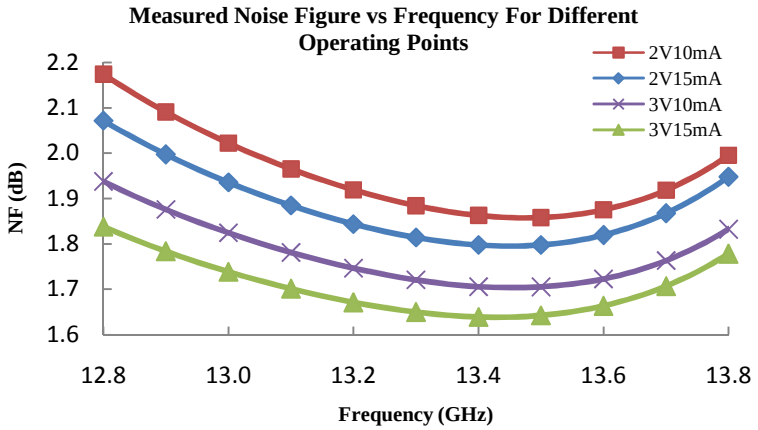

Fig. 3.11. Measured LNA noise figure vs. frequency for different operating points

Now, small signal input power variations and their effects on the circuit performance is analyzed. In this section, devices in the LNA are biased all the time at 2V–15mA. All the measurements are carried out at 13.515GHz operating frequency. Measured gain as a function of small signal RF power is presented in Fig. 3.12. Measured 1dB gain compression is –17dBm. Fig. 3.13 shows 3rd order intercept point (IP_3) measured result. Two tones at 10 KHz apart (13.515GHz and 13.515010GHz) are applied using Narda [42] power combiner to generate the intermodulation products. Measured 3rd order input intercept point (IIP_3) is –4.2dBm and 3rd order output intercept point (OIP_3) is 20dBm providing good linear response. Fig. 3.14, 3.15 and 3.16 show the effect of input RF signal power variations on the input return loss, output return loss and isolation respectively. It is seen that the designed circuit is robust and does not show much variations against such nonlinear effects. Fig. 3.17 represents the

stability factor as a function of RF power. As soon as the nonlinearity becomes significant after –10dBm RF power, stability factor increases. Minimum stability factor (>1) is achieved at the operating frequency which proves appreciable circuit design as high stability factor ruins the gain. However the circuit is found stable for the device's complete operating frequency range 0–20 GHz.

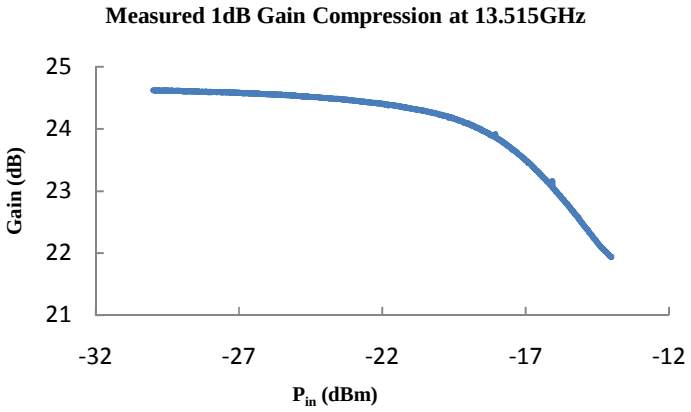

Fig. 3.12. Small signal RF 1dB gain compression (–17dBm)

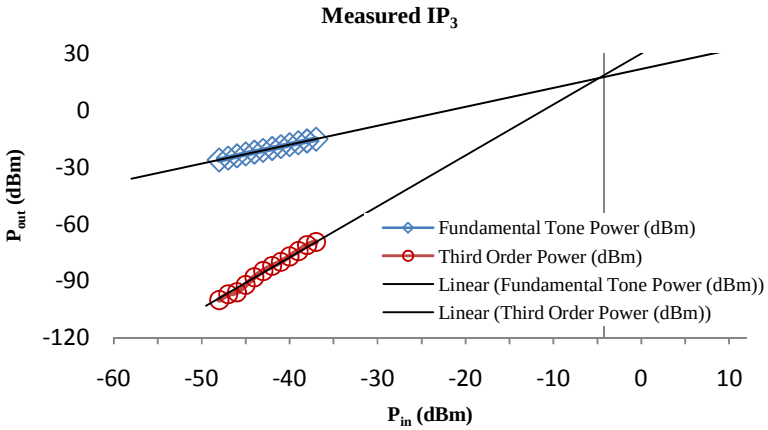

Fig. 3.13. 3rd order input intercept point (–4.2dBm) and output intercept point (20dBm)

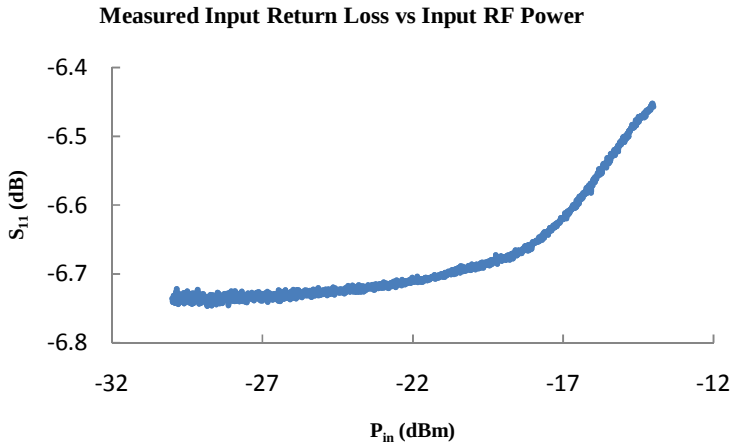

Fig. 3.14. Measured input return loss vs. input RF power. Controlled variations in input return loss stabilizes noise figure.

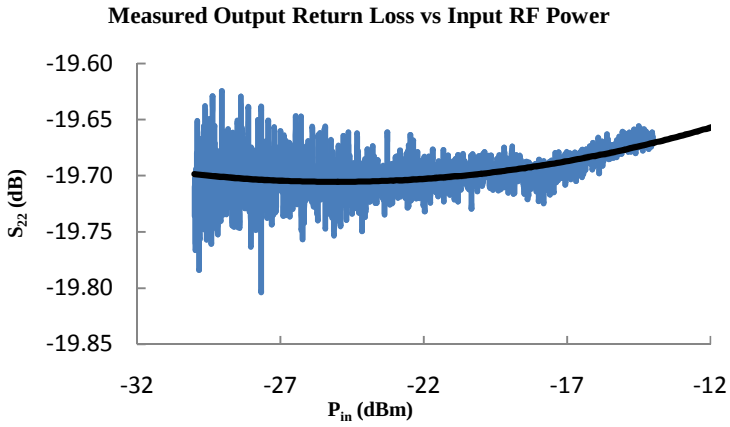

Fig. 3.15. Output return loss with respect to small signal variations (Expanded scale on vertical axis)

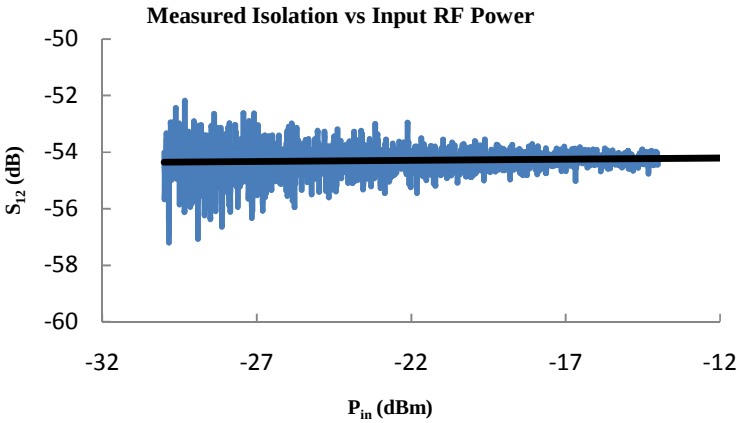

Fig. 3.16. Isolation vs. input RF power. Steady isolation ensures unconditional stability.

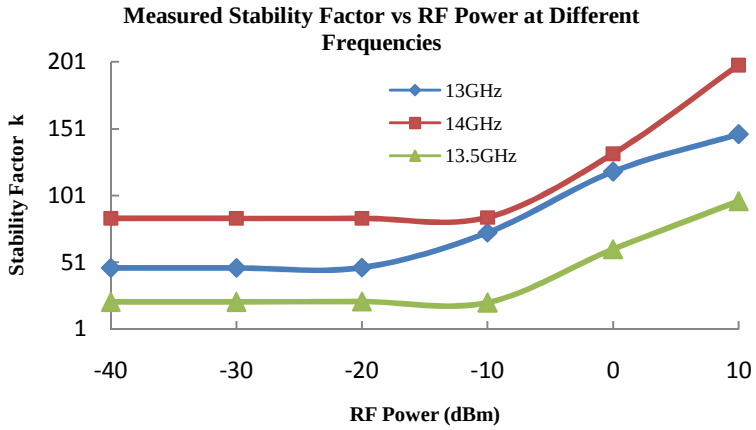

Fig. 3.17. Calculated stability factor from the measured S-parameter data. Nonlinearity is significant after –10dBm RF power which ruins LNA gain.

The fabricated high reliability (HiRel) three-stage LNA microwave integrated circuit with space qualified technology is presented in Fig. 3.18. The circuit is fabricated on 25mil alumina (ε_r=9.9, $tan\delta$=0.0007 at 10GHz) substrate. Metallization process is *Cr-Cu-Au* with 8µm accuracy.

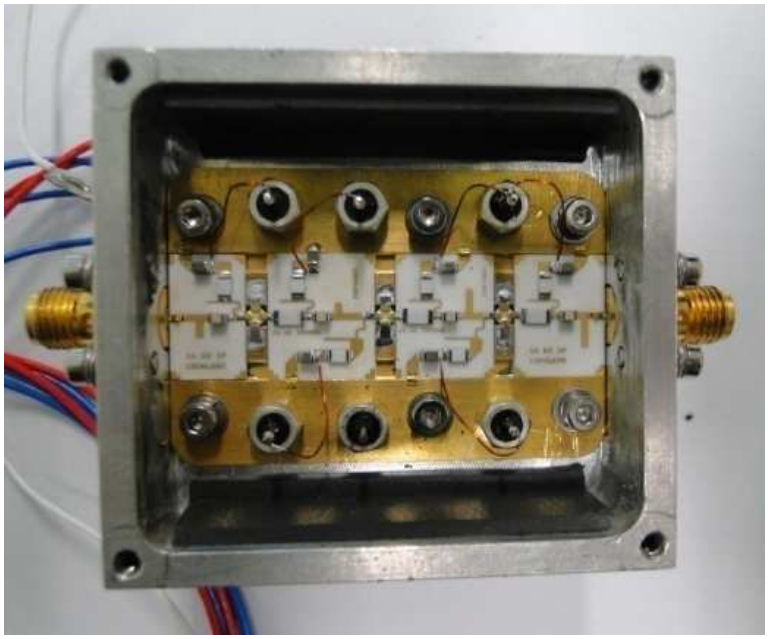

Fig. 3.18. Fabricated HiRel three-stage LNA microwave IC (design-1)

3.3. Analysis of LNA (design–2) using resistor temperature noise representation

This section focuses on the two-port modeling of the three-stage LNA considering intrinsic and extrinsic device parasitics. We have modeled and analyzed the input referred noise of the LNA in order to minimize the noise figure. For the same, sixteen-element device distributed model with all possible inherent resistor temperature noise sources are considered in the analysis as shown in the Fig. 3.19. Apart from the typical device level analysis, we have extended our analysis to the circuit level considering extrinsic device parasitics, stability resistor and matching networks to the next stage for the multistage system. We fabricated and tested design-2 of the LNA. In design-2, we minimized the input referred noise by making the correlated noise ideally zero. For the same, we considered stability-gain-noise figure trade off and the gain constrained noise optimization. Results are presented showing the improvements in the design-2 over design-1.

There are three assumptions for our analysis:

1. Device source lead inductance outside the package is negligible and so, no source degeneration is considered. Device source is always grounded which is also a requirement for the two-port analysis. The assumption is valid as, in the fabrication; device source is immediately terminated with the ground. Hence, L_{s1}, L_{s2} and L_{s3} in Fig. 3.1 are very small and can be neglected.
2. Noise from the bias networks is not considered in the analysis. However, bias network shows open circuit in the desire band.
3. Only thermal noise is considered in the analysis as other noises like $1/f$ noise, are negligible at our frequency of interest.

For two-port noise analysis, let i_{n1} and i_{n2} be the extracted noise sources present at the input and output port of the noiseless system respectively. For *intrinsic* device in Fig. 3.19, extracted noises $\overline{i_{n1}^2}$ and $\overline{i_{n2}^2}$ may be analyzed as, (refer to Appendix B)

$$\overline{i_{n1}^2} = \overline{i_{ngs}^2} + \overline{i_{ngd}^2}\left(\frac{j\omega C_{gd}}{\frac{1}{R_{gd}} + j\omega C_{gd}}\right)^2 = 4kT\left(\frac{1}{R_{gs}} + \frac{1}{R_{gd}}\left(\frac{j\omega C_{gd}}{\frac{1}{R_{gd}} + j\omega C_{gd}}\right)^2\right) \quad \text{.. ...(3.4)}$$

$$\overline{i_{n2}^2} = \overline{i_{nds}^2} + \overline{i_{ngd}^2}\left(\frac{j\omega C_{gd}}{\frac{1}{R_{gd}} + j\omega C_{gd}}\right)^2 = 4kT\left(\frac{1}{R_{ds}} + \frac{1}{R_{gd}}\left(\frac{j\omega C_{gd}}{\frac{1}{R_{gd}} + j\omega C_{gd}}\right)^2\right) \quad \text{.. ...(3.5)}$$

where, $\overline{i_{ngs}^2}$, $\overline{i_{ngd}^2}$ and $\overline{i_{nds}^2}$, are the uncorrelated intrinsic noise sources. However, $\overline{i_{n1}^2}$ and $\overline{i_{n2}^2}$ are correlated, which can be noticed from the equations (3.4) and (3.5).

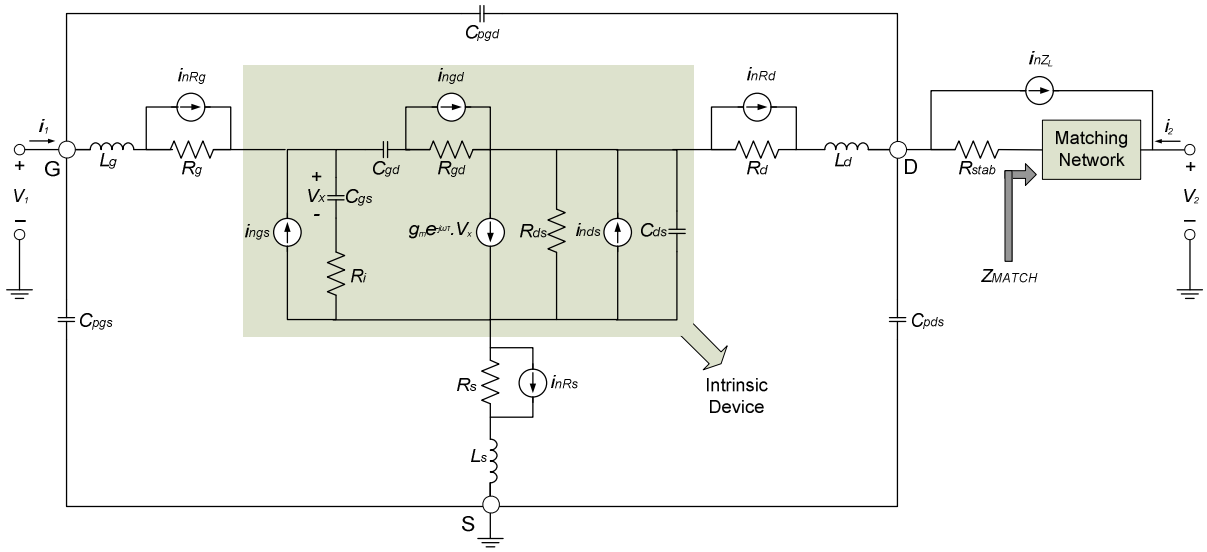

Fig. 3.19. Device small signal resistor temperature noise model followed by stability resistor and matching network to the next stage

Now, intrinsic device Y-parameter matrix is analyzed to be [Y^{in}]. By embedding the extrinsic package parasitics to [Y^{in}], complete device Y-parameter matrix is analyzed to be [Y^{ext}].

where,

$$\left[Y^{in}\right] = \begin{bmatrix} Y_{11}^{in} & Y_{12}^{in} \\ Y_{21}^{in} & Y_{22}^{in} \end{bmatrix} \text{ and } \left[Y^{ext}\right] = \begin{bmatrix} Y_{11}^{ext} & Y_{12}^{ext} \\ Y_{21}^{ext} & Y_{22}^{ext} \end{bmatrix} \quad \text{... ...(3.6)}$$

Parameters embedding analysis is presented in Appendix B.

Correlated extracted input and output noise sources i_{n1} and i_{n2} for the complete three-stage noiseless LNA, considering device intrinsic and extrinsic package parasitics may be analyzed as a function of various inherent noise sources and device parameters as follows,

$$i_{n1} = i_{ngs}\left[Y_g\left(-Z_{ngs}{}' - Z_{ngs}\frac{Z_g{}'}{Z_e}\right)\right] + i_{nds}\left[Y_g\left(Z_{nds}{}' - Z_{nds}\frac{Z_g{}'}{Z_e}\right)\right] + i_{ngd}\left[Y_g\left(Z_{ngd}{}' + Z_{ngd}\frac{Z_g{}'}{Z_e}\right)\right]$$
$$+ i_{nZ_L}\left[Y_g\left(Z_{nL}{}' + Z_{nL}\frac{Z_g{}'}{Z_e}\right)\right] + i_{nRs}\left[Y_g\left(Z_{nRs}{}' + Z_{nRs}\frac{Z_g{}'}{Z_e}\right)\right] + i_{nRd}\left[Y_g\left(Z_{nRd}{}' + Z_{nRd}\frac{Z_g{}'}{Z_e}\right)\right]$$
$$+ i_{nRg}R_g\left[Y_g\left(1+\frac{Z_g{}'}{Z_e}\right)\right] \qquad \text{... ...(3.7)}$$

$$i_{n2} = -i_{ngs}\frac{Z_{ngs}}{Z_e} - i_{nds}\frac{Z_{nds}}{Z_e} + i_{ngd}\frac{Z_{ngd}}{Z_e} + i_{nZ_L}\frac{Z_{nL}}{Z_e} + i_{nRs}\frac{Z_{nRs}}{Z_e} + i_{nRd}\frac{Z_{nRd}}{Z_e} + i_{nRg}\frac{R_g}{Z_e} \qquad \text{... ...(3.8)}$$

The values of various impedance and admittance parameters used in the equations (3.7) and (3.8) are presented in Appendix B. The identical devices and identical stability resistors are considered for the analysis in all three-stages. Using equation (3.6), i_{n1} and i_{n2} can be represented in terms of *input referred* equivalent noise sources i_n and v_n as mentioned below.

$$i_n = i_{n1} - i_{n2}\frac{Y_{11}^{ext}}{Y_{21}^{ext}} \qquad \text{... ...(3.9)}$$

$$v_n = -\frac{i_{n2}}{Y_{21}^{ext}} \qquad \text{... ...(3.10)}$$

The analysis for the equations (3.9) and (3.10) is presented in Appendix B.

Proceeding further, the condition for the minimum noise factor F_{min} is given by, [3,37,39,43]

$$\frac{d\left(F\big|_{B_s=-B_c}\right)}{dG_s} = 0 \qquad \text{... ...(3.11)}$$

$$\textit{where, } Y_c = \frac{\overline{v_n^* i_n}}{\overline{v_n^2}}$$

$Y_c=G_c+jB_c$ is the correlation admittance, and $Y_s=G_s+jB_s$ is the source admittance.

Solution to the equation (3.11) gives $G_s = G_{opt}$ and $B_s = B_{opt} = -B_c$. where, optimum source termination admittance $Y_{opt} = G_{opt} + jB_{opt}$.

Noise factor F in terms of F_{min} and optimum value of the source termination can be represented as, [3,37,39,43]

$$F = F_{\min} + \frac{R_n}{G_s}\left[\left(G_s - G_{opt}\right)^2 + \left(B_s - B_{opt}\right)^2\right] \quad \text{. ...(3.12)}$$

$$\text{where, } G_s = \frac{\overline{i_s^2}}{4KT},\ R_n = \frac{\overline{v_n^2}}{4KT}$$

In equation (3.12), noise factor can be divided in terms of correlated noise and uncorrelated noise. The term F_{min} represents the uncorrelated noise contribution which cannot be made zero. The other term is the noise contribution by the correlated noise which can be made zero by applying source termination admittance Y_{opt}. Hence, the optimum source termination as analyzed in equation (3.12) leads to the minimum noise figure. However, to achieve maximum gain it requires conjugate match which is not same as the noise match as analyzed. Hence, noise match is achieved at the cost of poor input return loss, and hence poor gain. To extract the parasitics in equations (3.7) and (3.8), cold FET method [44],[45] can be used. It requires the S-parameter measurements of the device in cold-state (off-state) by driving the device gate below threshold voltage. In our case, it is below –3V for CFY67 GaAs HEMT. However, in our case, as the device generic model was available from the manufacturer, analysis was carried out by simulation and optimum admittance was found out.

From the stability analysis for the single stage LNA (design-1) shown in Fig. 3.3, it was concluded that 9Ω series resistor at the output port is required to stabilize the device unconditionally operating at 2V/15mA. However, it was found that for multistage amplifier design, the case is not the same. Adding a 9Ω resistor at the output port of the each stage achieves the stability factor k much greater than 1. Consequently, it ruins the gain and more importantly it degrades noise performance. In cascaded system, the input impedance of the following stage acts as the load impedance for the preceding stage. So the effective stability resistor to be presented at the output port of the each stage is far smaller than 9Ω which is required if it would have been single stage design. Stability analysis proves that around 1Ω

resistor value is enough for the gain to reach near to the Maximum Stable Gain (MSG), with minimum possible noise figure and to achieve the unconditional stability. The factors like temperature and bias variations inevitably result in the device S-parameter fluctuations. So, to be on safer side, 3.3Ω series stability resistor is used at the output of the each stage.

In the equation (3.12), to make the correlated noise minimum (ideally zero), required Y_{opt} is analyzed to be *(17+j38) mS*. For the same Y_{opt} , analyzed *minimum* noise factor $F = F_{min}$= 1.30 (noise figure is 1.13dB) at around 13.5GHz in Ku-band. Fig. 3.20 shows the noise factor variation with respect to the source admittance Y_s for 3.3Ω stability resistors. Color bar shows the noise factor intensity distribution. Noise factor becomes minimum when $Y_s = Y_{opt}$. Now, let Γ_{Gmax} be the reflection coefficient where gain is maximum, and Γ_{opt} be the reflection coefficient where NF is minimum. Γ_{Gmax} corresponds to the conjugate power match while Γ_{opt} corresponds to Y_{opt}. In this design, Γ_{Gmax} is analyzed as $0.84\angle -143.08^{o}$ and Γ_{opt} is analyzed as $0.72\angle 130.63^{o}$.

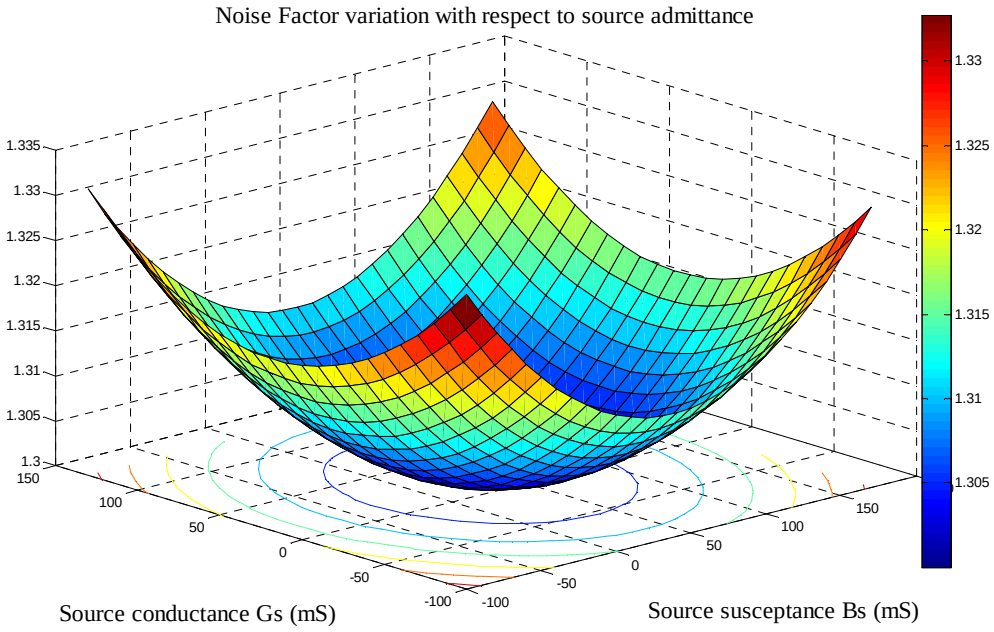

Fig. 3.20. Noise factor variation with respect to the source admittance Y_s (R_{stab}=3.3Ω, design-2)

Fig. 3.21 shows the gain constrained noise optimization for three-stage LNA with each stage operating at 2V/15mA rating. Only reflection coefficient's magnitude is considered in the graph, however angle of the reflection coefficient also affect the gain and noise figure significantly which directly implies from Fig. 3.20.

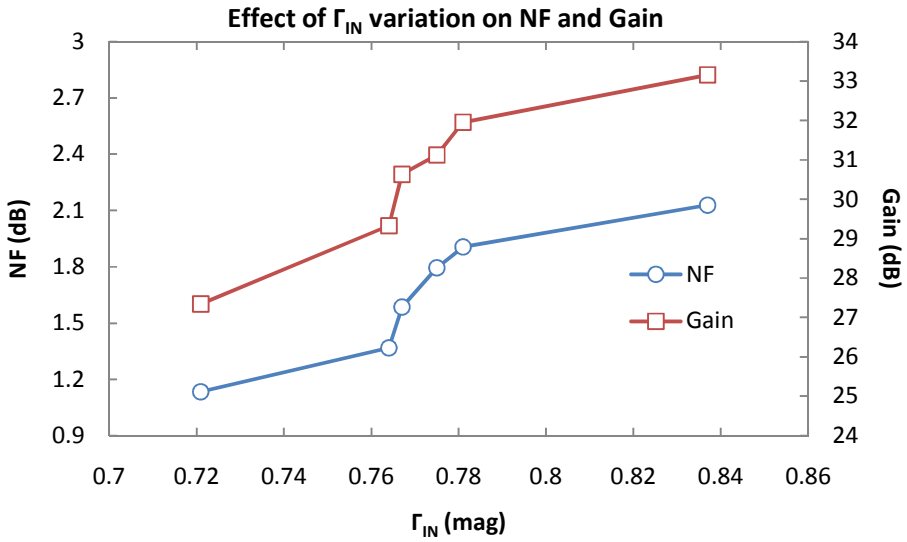

Fig. 3.21. Simulated Gain-NF trade-off (R_{stab}=3.3Ω, design-2)

As mentioned in equations (3.7) and (3.8), Z_{nL} and Z'_{nL} depend on the stability resistor. So, if stability resistor decreases, i_{n1} and i_{n2} also decreases. It improves noise figure performance with simultaneously providing unconditional stability in the device operating range 0–20GHz. We designed new Ku-band LNA (design-2) topology considering the stability resistor optimization (3.3Ω 0402 by Susumu [46]), gain-constrained noise optimization and analytical aspects presented in selection of Y_{opt} to make correlated noise zero.

Fig. 3.22 to Fig. 3.27 show the measurement results of various performance parameters for the LNA design-2. Measurenments are carried out at 13GHz in Ku-band when each stage is operated at 2V/15mA. Measured noise figure is 1.46dB. Gain constrained noise optimization ensures a gain of 30.1dB with very good –27dB output return loss. Input port is noise matched giving –12.8dB input return loss. It has a very good isolation of –56.7dB ensuring the unconditional stability of the circuit. Designed circuit is robust and gives considerably good results even at very low bias conditions. Fabricated amplifier is also tested with each stage operating at 1V/2.6mA. The measured noise figure is 2.14dB, gain is 26dB

with –9dB input return loss and –18dB output return loss. Isolation is better than –60dB. It results into DC power consumption as low as 7.8mW.

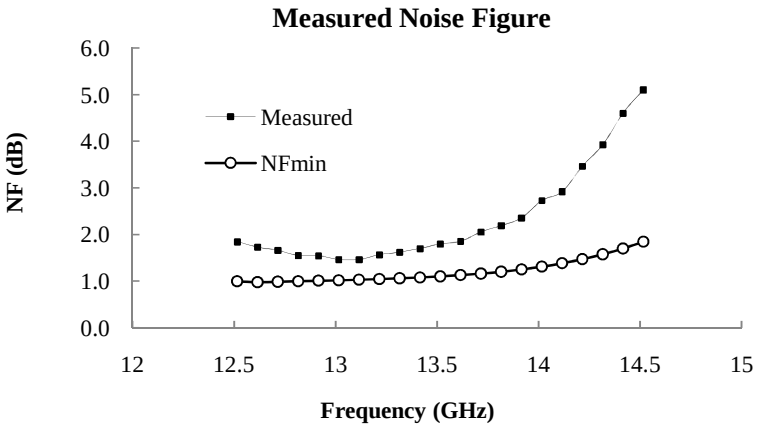

Fig. 3.22. Simulated $NF_{\min}$ for Γ_{opt} and measured NF (1.46dB)

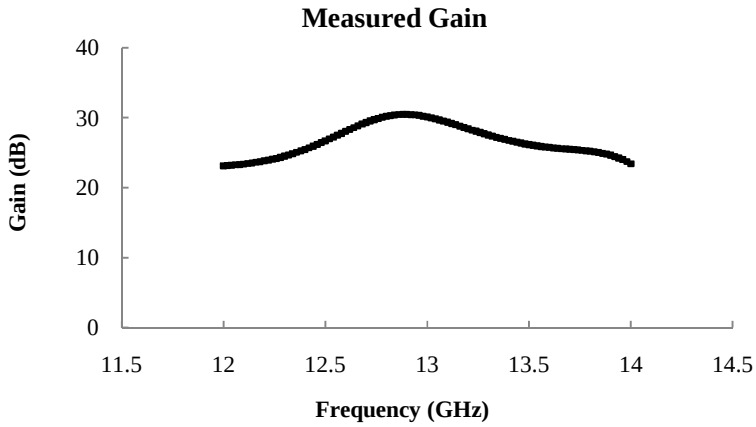

Fig. 3.23. Measured gain (30.1dB)

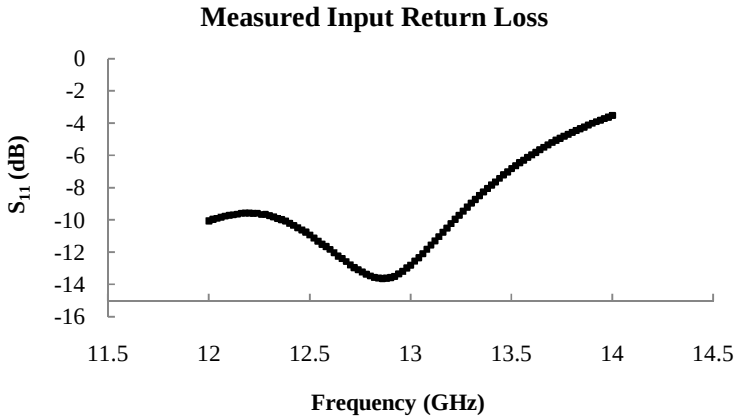

Fig. 3.24. Input return loss (better than –10dB)

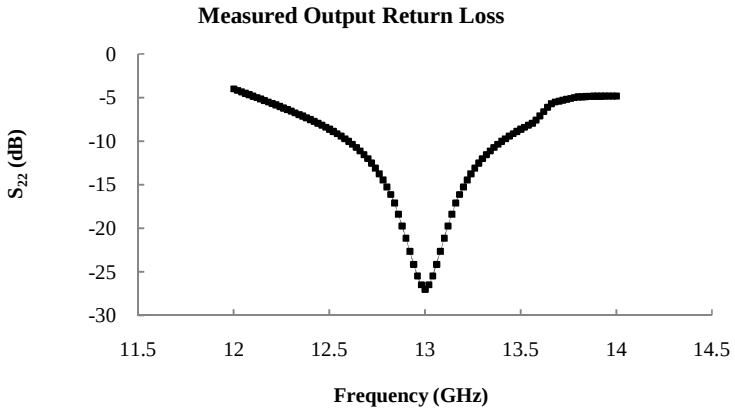

Fig. 3.25. Power matched output port reflection

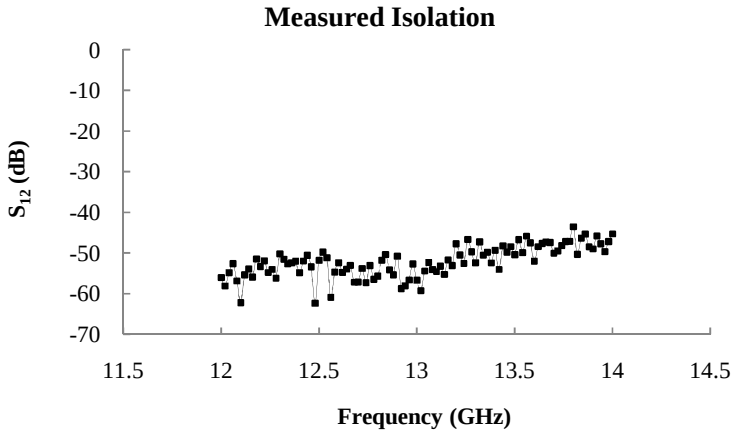

Fig. 3.26. Measured isolation

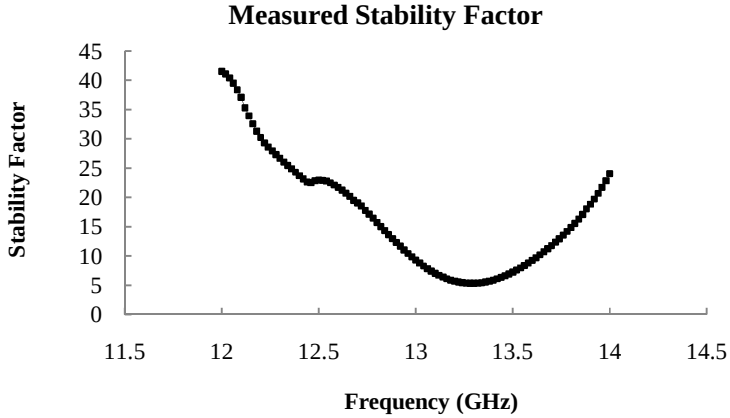

Fig. 3.27. Measured stability factor

The improvements in various measured performance parameters of LNA design-2 over design-1 are presented in Table 3.1. It can be seen that there is significant improvement

in the noise figure as well as in the gain. In the analysis we found that the stability factor much greater than 1 ruins the gain and also degrades the noise figure. It was taken care of while designing the second LNA topology. Input return loss has been improved in design-2 which was poor than –10dB in design-1.

Table 3.1. Comparison of LNA design-1 with LNA design-2

Parameters	Measured results LNA design-1	Measured results LNA design-2
Noise Figure (dB)	1.76	1.46
Gain (dB)	25	30.1
Stability Factor	21.4	7.2
S_{11} (dB)	-6.8	-12.8
S_{22} (dB)	-24.3	-27.0
S_{12} (dB)	-52	-57

However, fabricated improved LNA MIC design is compared with different technologies, MMIC designs and CMOS processes. Table 3.2 briefly describes the comparison of the proposed MIC design with the previously published work in Ku-band. From the tabular analysis it can be concluded that the work presented here has excellent noise figure and gain with very low power consumption.

Fig. 3.28 shows the fabricated design-2 of LNA MIC on alumina substrate and Kovar carrier plate using CFY-67 GaAs HEMT. Actual circuit size of the fabricated microawave IC is 411mm^2.

Table 3.2. Comparison of the proposed design (MIC) with previously published works in Ku-band

Reference	LNA operating Freq. (GHz)	Device used	V_{ds}(volts) /I_{ds}(mA)	Device S_{21}(dB) /NF_{min}(dB) at freq. (GHz)	No. of stages in LNA	NF (dB)	Gain (dB)	S_{11} (dB)	S_{22} (dB)	S_{12} (dB)	Power cons. (mW)
This work	**13**	**GaAs HEMT CFY67-08P**	**2/45**	**0.76/8.92 at 13**	**3**	**1.46**	**30.1**	**-12.8**	**-27.0**	**-56.7**	**90**
			1/7.8	**1.13/6.95 at 13**	**3**	**2.14**	**26.1**	**-8.7**	**-18.1**	**-59.9**	**7.8**
[47]	12	pHEMT	2/24	NA	2	1.24	24.5	<-16	<-16	NA	96
[48]	12	pHEMT	3/20	NA	2	<1.4	>15	-17†	-20†	NA	60
[49]	13.8	GaN HEMT	NA	NA/2 at 20	3	1.75†	22†	-11†	-12†	NA	840
[50]	14	GaN HEMT	NA	NA	3	1.9	>19.8	-6	-13	NA	NA
[51]	14.5	RF CMOS	1.6/12	NA	1	2	12.9	-6†	-14†	-30†	19.2
[52]	13	pHEMT	3/52	NA	3	2.1	22	-13	-15	-45	156
[53]	16	pHEMT	4/65	1.02/8.54 at 16	3	2.3	21.6	-14†	-15†	NA	260
[54]	13	pHEMT	NA	NA	2	2.5	22	<-10	<-10	NA	100
[55]	12	HBT	3.3/7.2	NA	1	3	11	-6†	-8†	NA	24
[56]	13	HEMT	1st stage 2.5/80, 2nd stage 4/109	NA/<1 dB at 10GHz	2	3	17.5	-13†	-12†	NA	636
[57]	14 to 15	CMOS	1.3/22	NA	2	3.2†	10.5†	-23†	-10.7†	NA	28.6
[58]	16	BiCMOS	1.5/1.5	NA/3 at 17	1	3.8	14.5	-4	-18	NA	2.25
[59]	16	HBT	1.5/5.3	NA	1	4	11.5	NA	NA	NA	8
[60]	15.2	CMOS	1.3/4	NA	2	4.2	10.8	<-10	-6	NA	5.2
[61]	13	CMOS	1.8/5.4	NA	1	4.67	4.9	-20†	-12†	NA	9.72
[62]	12	HBT	3/4	NA	1	4.7	9	-11	-6	NA	12

† Approx. mentioned from the figures NA: Not Available

Fig. 3.28. Fabricated three-stage LNA microwave IC (design-2)

3.4. Chapter conclusions

Three stage low noise amplifiers at Ku-band were designed. Analysis was carried out for the multistage design in order to minimize the noise figure. Circuit input referred noise was analyzed using resistor temperature noise sources, and intrinsic and extrinsic parameters of the sixteen element GaAs HEMT device. Noise figure was presented in terms of correlated and uncorrelated noise components. Both the low noise amplifiers were fabricated and tested in Ku-band. LNA was designed taking care of trade-offs, intrinsic and extrinsic parasitic elements, stability considerations and gain-constrained noise optimization in order to minimize the input referred correlated noise. The final LNA design showed its potential by achieving the excellent results. The performance parameters were compared extensively with the relevant published work in Ku-band LNA. It can be concluded that the design presented here has the simultaneously very low noise figure and high gain with low power consumption.

Chapter 4

Mixer

In this section a novel single balanced passive mixer design is proposed. It consists of a modified 3-dB hybrid and a pair of anti-parallel low barrier Shottky diodes. The mixer is designed to operate in 14-15GHz LO.

4.1. Wideband coupler design

The mixer's isolation and LO noise cancellation properties depends on the coupler as discussed in section 2.2. Hence, the coupler design becomes a crucial element in the mixer. However, coupler design is more challenging, when it is to be used in the mixer. As mixer operates on two distinct frequencies, coupler has to be designed in order to provide desired response for both the frequencies. Furthermore, the work becomes more challenging if the IF is considerably large.

We have presented a wideband coupler for the mixer application. Typical rat-race coupler is modified by introducing composite right-left hand (CRLH) transmission line in $3\lambda/4$ branch to provide the wideband response.

As discussed in section 2.2, analyzed CRLH couplers in [14], [19], and [20] uses lumped inductors and lumped capacitors in the design, where in all the cases, the frequency of operation is below 5.2GHz. In our case, the LO operating frequency is up to 14.98GHz. To allow the high frequency operation, we have used lumped capacitor with good tolerance (by American Technical Ceramics– ATC [63]) and the distributed element inductor. Fig. 4.1 shows the proposed quasi CRLH rat-race coupler and the CRLH equivalent transmission line model. Right–hand section of the composite transmission line uses the distributed elements. Left–hand section of the composite transmission line uses lumped capacitors and distributed inductor. Left–hand distributed inductor is realized by very thin transmission line and via

plated through hole connected to the conductive ground plane. Hence it signifies the name *quasi* CRLH coupler. In Fig. 4.1, introduced L_{LH} and C_{LH} together form a left–hand transmission line which is different from the conventional right hand structure. The circuit is designed and simulated on 25mil thick TMM10i [64] soft substrate (ε_r=9.8, $tan\delta$=0.0022 at 10GHz).

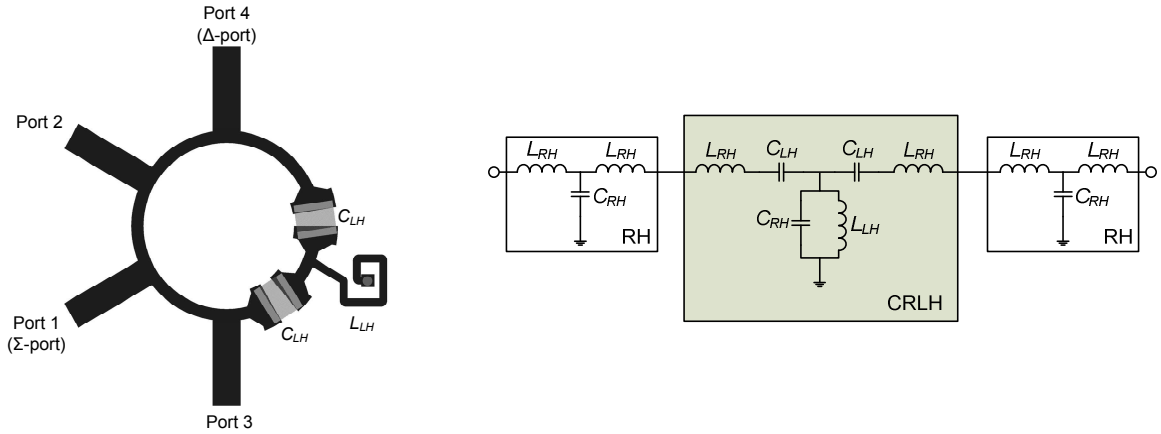

Fig. 4.1. Proposed rat-race hybrid (in left). Equivalent composite right/left handed (CRLH) transmission line model (in right).

CRLH inclusion in the rat-race coupler allowed it to be wideband. Fig. 4.2 shows the simulated coupler scattering parameter results in 13–16GHz band. Insertion loss is near to –3dB and ensures equal power division for the balanced operation. Σ-port (port-1) return loss is close to –40dB at around 13.515GHz. Isolation remains almost below –20dB in the band of interest. Fig. 4.3 shows the simulated phase difference results. It can be seen that the phase difference $\angle S_{21} - \angle S_{31}$ remains within $0^o \pm 10^o$ and $\angle S_{24} - \angle S_{34}$ remains within $180^o \pm 10^o$ for 13GHz to 15.5GHz range. Size of the proposed coupler is 4.3mm X 4.3mm. The coupler is designed to provide the response shifted towards LO frequency as S_{41} response shown in the Fig. 4.2. LO frequency is to be kept higher than the RF in our case. LO is to be applied to the Δ-port which allows LO noise to get cancelled.

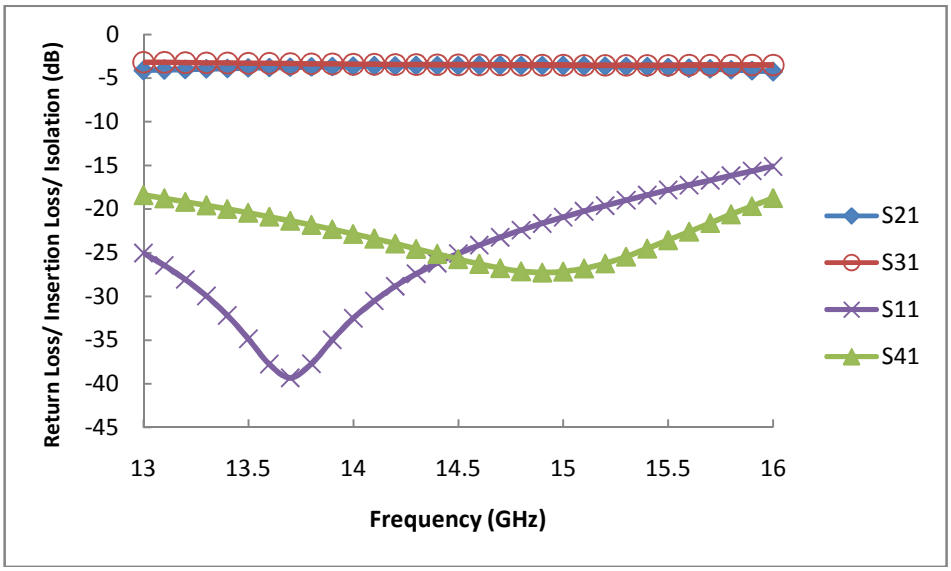

Fig. 4.2. Simulated coupler results: Σ-port return loss (S_{11}), insertion loss (S_{21} and S_{31}) and isolation (S_{41})

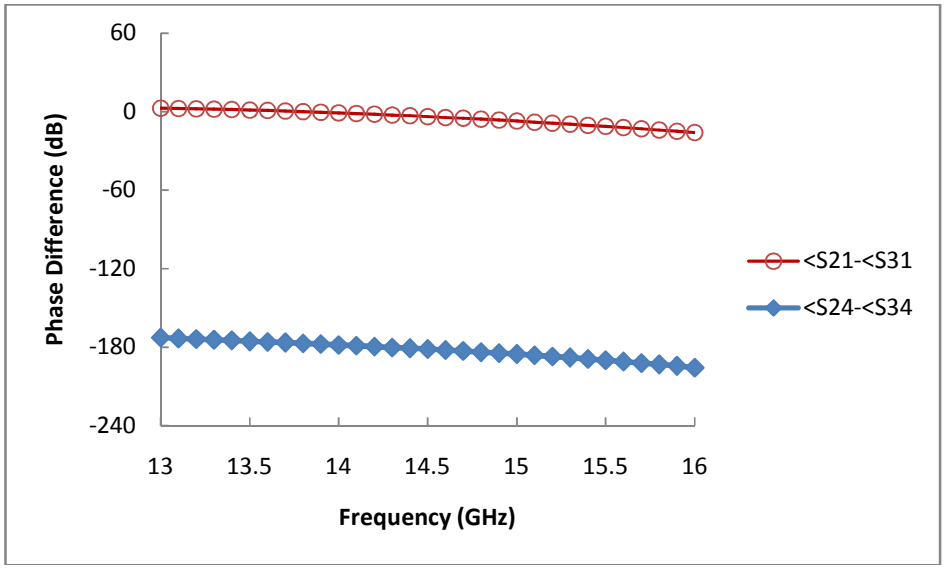

Fig. 4.3. Simulated coupler phase difference. Phase imbalance is within ±10° for 13–15.5GHz range.

4.2. Ku-band mixer design

Fig. 4.4 shows the Ku-band passive balanced mixer using the quasi CRLH rat-race coupler. RF and LO are applied to the pair of mutually isolated Σ-port (port-1) and Δ-port (port-4) respectively. From Fig. 4.2, it can be concluded that the coupler is designed to provide the best port-1 return loss in the band at RF frequency as RF is to be applied to the port-1.

Further it also can be seen that the proposed coupler has wideband port-4 to port-1 isolation response as it has to accommodate variable LO frequency.

In the proposed mixer in Fig. 4.4, Aeroflex metelics MSS20-143-B10D [65] low barrier beam lead identical diodes D_1 and D_2 are connected to the port-2 and port-3. Diodes' remaining terminal is combined to generate the IF. One way is, to terminate one terminal of the diode to the ground while keeping the other terminal connected to port-2 and port-3. IF is to be taken out from the point on the hybrid, $3\lambda/4$ away from the RF port as presented in [66,67]. But in the coupler proposed here, it is difficult to do so due to presence of LH lumped elements. As a solution to this, port-2 and port-3 are folded inside the coupler which also allows to achieve the small size. D_1 and D_2 are the diodes connected in the anti-parallel configuration; provide nonlinear behavior in order to generate the sum and difference frequencies. In 180° hybrid, anti-parallel configuration of the diodes allows elimination of all *(m,n)* harmonics where *m* and *n* are even. Also, all *(m,n)* harmonics where $m=\pm2$ and $n=\pm1$ are eliminated. As LO is applied to Δ-port, noise present in LO gets cancelled as discussed in section 2.2. Inductors L_2, L_3 and L_4 provide DC return paths for the diodes. As L_4 bypasses the DC component present after mixing, it is not seen in the IF output. L_2 and L_3 are 180µm $\lambda/4$ TLs designed to ensure enough wideband open circuit at the diode inputs in Ku-band. Hence, it eliminates any chances of RF or LO bypassing before mixing action take place. L_2 and L_3 are designed in order to have the least electromagnetic interference with the nearest components present. However, the design layout is electromagnetically simulated in order to accommodate all the effects. Size of the mixer is almost same as the coupler. IF is taken out from a 50Ω TL (0.6mm on TMM10i substrate [64]) using a Panasonic ERJ-1 0Ω jumper (*J*) [68]. Jumper can be used in the IF line as IF is not as high as RF.

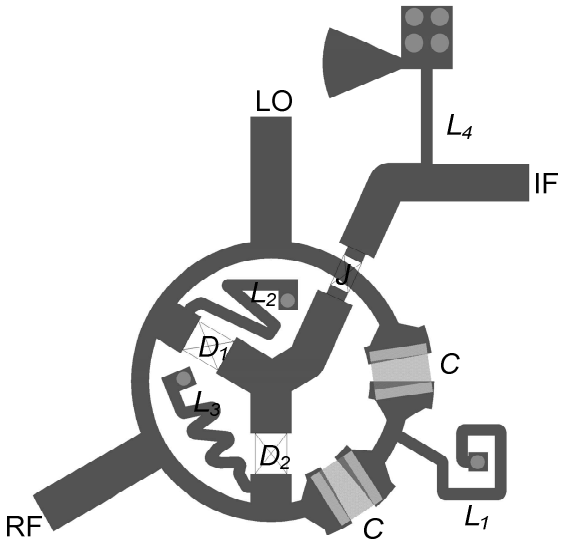

Fig. 4.4. Ku-band passive balanced mixer using the quasi CRLH rat-race coupler

Fig. 4.5 shows the conversion loss of a mixer with respect to LO frequency. Mixer exhibits almost flat conversion loss response in 14.3GHz to 14.7 GHz LO frequency range. Conversion performance is found better at around 14.3GHz and around 15GHz. Fig. 4.6 shows conversion loss of a mixer with respect to LO power. Fig. 4.7 shows mixer SSB and DSB NF with respect to LO frequency and IF. DSB NF is the NF without considering image rejection RF filter. SSB NF is 3dB poor than the DSB NF. In DSB case, the image IF falls on the true IF and hence, it improves the conversion loss and the NF by 3dB. There is 1.5dB noise figure variation in 100MHz to 1500MHz IF range. LO to RF isolation is near to –25dB for 14GHz to 15GHz LO frequency range as shown in Fig. 4.8. Mixer exhibits potentially linear response. 1dB compression and IIP_3 are at 4dBm and at 15.7dBm RF power respectively as shown in Fig. 4.9 and Fig. 4.10.

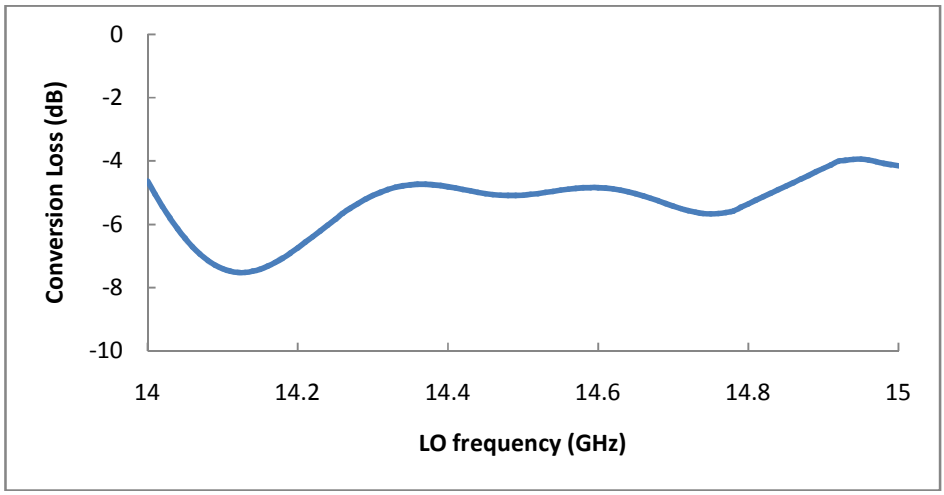

Fig. 4.5. Conversion loss vs. LO frequency for P_{LO} = 9.5dBm, f_{RF} = 13.5GHz, P_{RF} = –50dBm

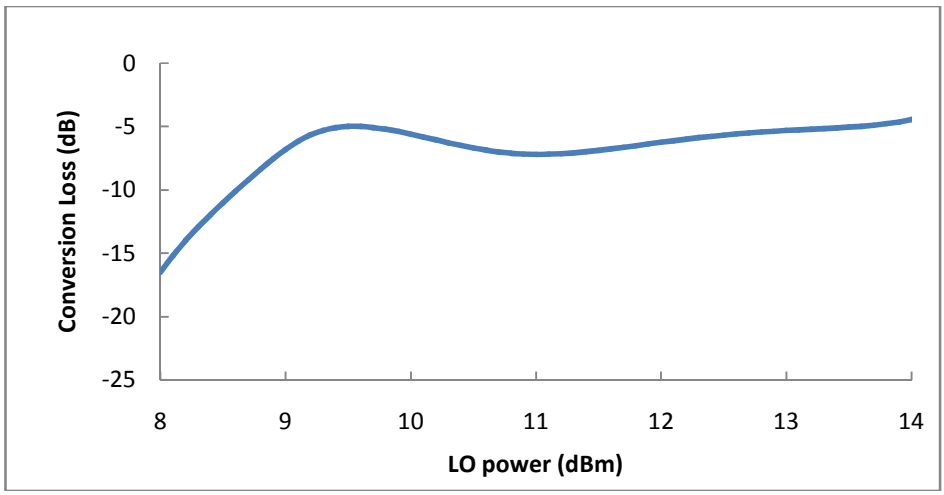

Fig. 4.6. Conversion loss vs. LO power for f_{LO} = 14.31GHz, f_{RF} = 13.5GHz, P_{RF} = –50dBm

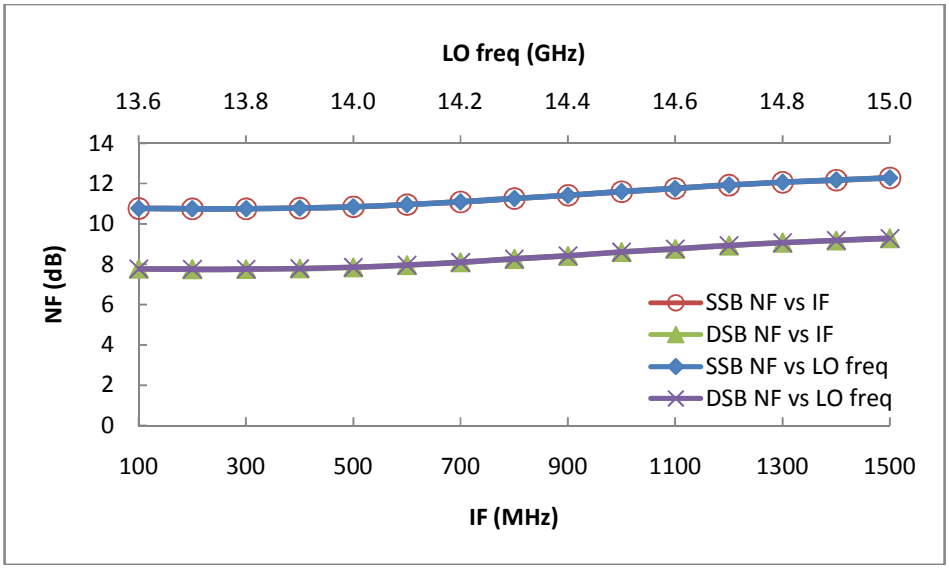

Fig. 4.7. SSB and DSB NF vs. LO frequency and IF for P_{LO} = 9.5dBm, f_{RF} = 13.5GHz, P_{RF} = –50dBm

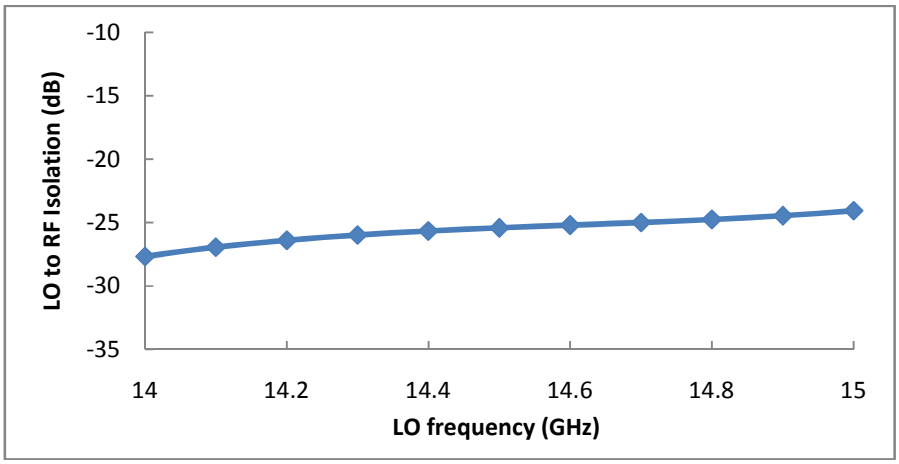

Fig. 4.8. RF to LO isolation for different LO frequencies for P_{LO} = 9.5dBm

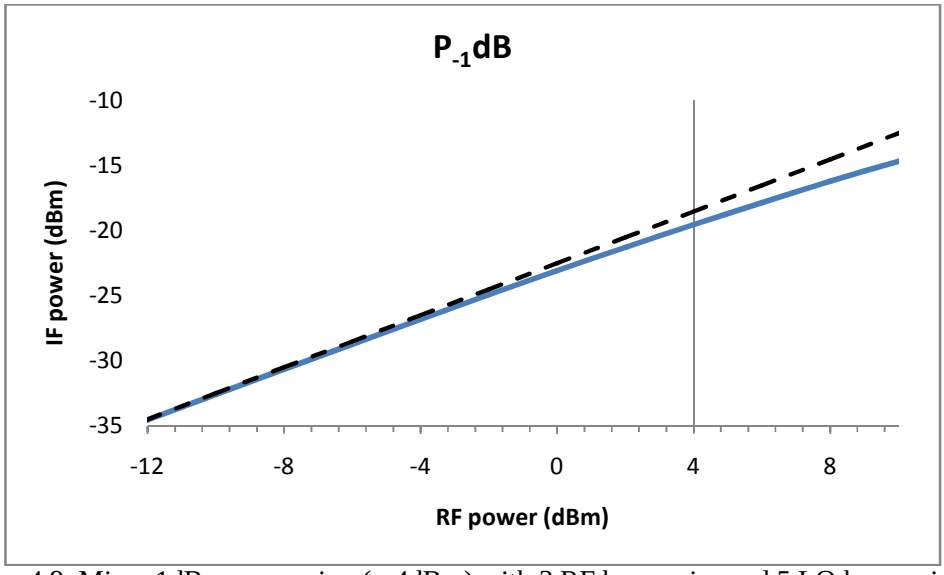

Fig. 4.9. Mixer 1dB compression (= 4dBm) with 3 RF harmonics and 5 LO harmonics, f_{RF} = 13.5GHz, f_{LO} = 14.31GHz, P_{LO} = 9.5dBm

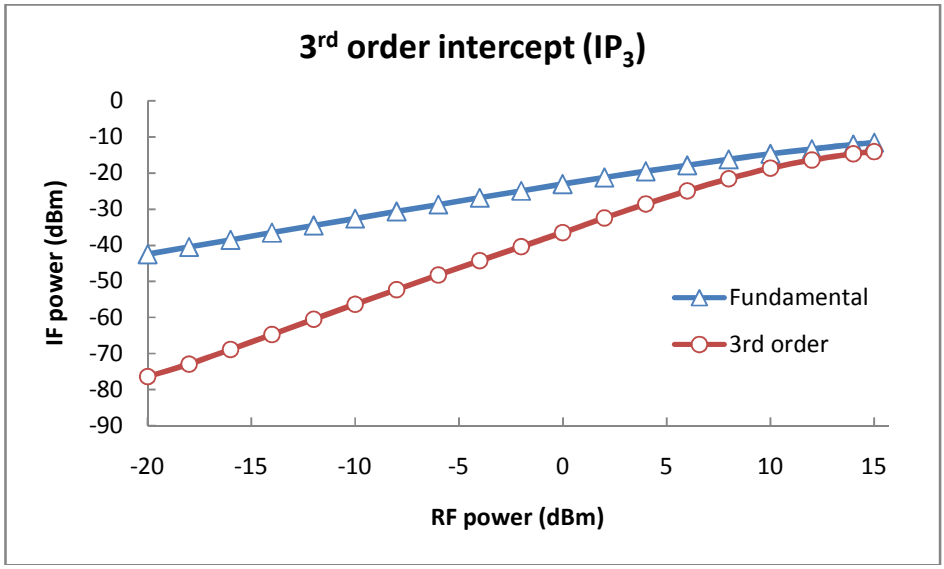

Fig. 4.10. Mixer IP_3 (IIP_3=15.7dBm) with 3 RF harmonics and 5 LO harmonics, f_{RF} = 13.5GHz, f_{LO} = 14.31GHz, P_{LO} = 9.5dBm

4.3. IF filter

As output of the mixer contains the unwanted intermodulation products, all of them are to be suppressed by the IF filter to achieve desired IF frequency in the output. Fig. 4.11 shows the complete mixer followed by IF filter. Filter is designed with the multiple $\lambda/4$ radial stubs in order to achieve wideband rejection of the selected intermodulation frequencies. Fig. 4.12 shows the insertion loss response of the two-stage multiband filter. The filter is designed to suppress RF, LO frequency, 2^{nd} order intermodulation products ($2LO$, $2RF$ and $LO+RF$), and 3^{rd} order intermodulation products ($2RF–LO$ and $2LO–RF$). Table 4.1 describes the results after applying the two-stage IF filter to the mixer. It can be seen that the frequencies other than the IF, get suppressed by significant amount.

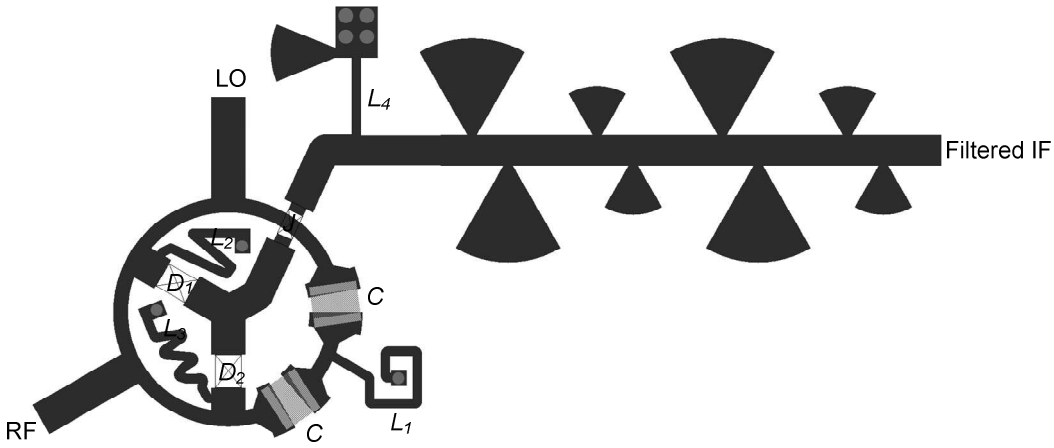

Fig. 4.11. Complete mixer followed by two-stage IF filter

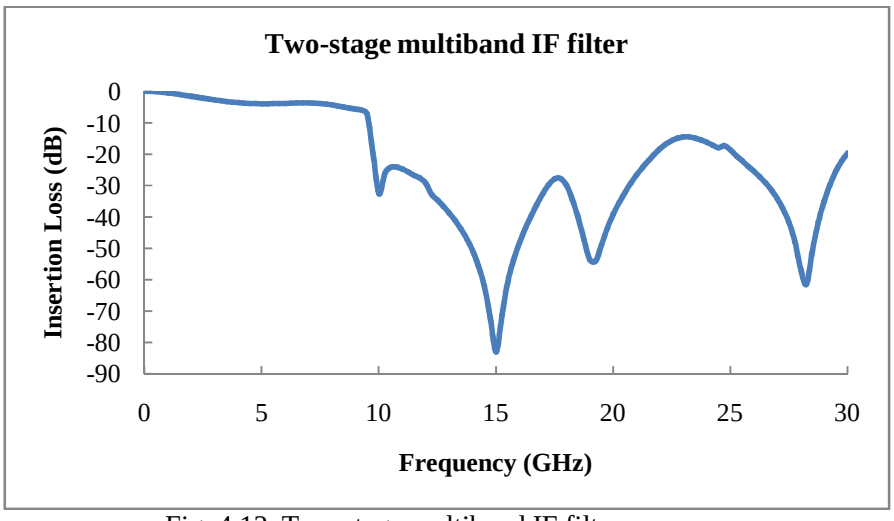

Fig. 4.12. Two-stage multiband IF filter response

Table 4.1. Undesired intermodulation products suppression using two-stage multiband-rejection filter

Frequency (GHz)	Mixing spectrum without filter (dBm)	Mixing spectrum with filter (dBm)
0.810 (IF)	-39.32	-39.75
13.50 (RF)	-32.50	-81.97
14.31 (LO)	-11.46	-77.23
15.12 (2*LO–RF) 3rd order	-46.44	-132.58
27.81 (LO+RF) 2nd order	-42.57	-90.92
28.62 (2*LO) 2nd order	-29.53	-72.07

4.4. Chapter conclusions

We presented a wideband 3-dB balanced coupler for the mixer application. Typical rat-race coupler was modified by introducing CRLH transmission line in $3\lambda/4$ branch to provide wideband response. Proposed coupler is small in size (4.3mm X 4.3mm) and provides wideband response in 13–16GHz. Using the coupler presented; small size wideband singly balanced passive mixer in Ku-band was designed. Mixer simulated results were presented in terms of mixer performance parameters, conversion loss, noise figure and linearity. Proposed mixer has low conversion loss and very good LO to RF isolation in Ku-band. The mixer exhibited good linear response; 1-dB compression was at 4dBm RF power, and IIP_3 was at 15.7dBm RF power. Two-stage multiband-reject IF filter was designed and simulated to suppress– RF, LO frequency, 2^{nd} order intermodulation products ($2LO$, $2RF$ and $LO+RF$), and 3^{rd} order intermodulation products ($2RF–LO$ and $2LO–RF$).

Chapter 5

Local Oscillator

Local Oscillator (LO) contributes as an important building block in the communication systems. It generates a frequency offset from the RF in order to produce IF using mixer. As VCO provides the frequency tunability in order to generate required IF, low phase noise VCO is used as a LO in our case.

VCO has been always of an interest for the researchers due to the challenges like low phase noise, tunability with sustained oscillations, small size, and ease of fabrication avoiding complex structures. Any oscillator requires high-Q resonator in order to achieve low phase noise and so frequency stability. At high frequencies, dielectric resonators are preferred as they have very high-Q and hence they have ability to generate high spectral purity signal. Unfortunately they have drawbacks, including limited tuning range, and limiting temperature range. They are bulky in size and require complex assembly. Here, we proposed new high-Q planar resonators in two different Ku-band VCO topologies at around 15GHz and 14.3GHz center frequency to generate required IF; 1.5GHz and 800MHz for our scatterometer application. (From Fig. 4.6, it can be noticed that the mixer has the lowest conversion loss at 14.3GHz and at 14.98GHz in the LO band). Introducing small size planar resonators in the circuit rather than the conventional dielectric resonators, drastically reduces the cost of fabrication and time to market.

5.1. Design of low power low phase noise negative resistance Ku-band VCO using planar resonator pair (Design–1)

New negative resistance voltage-controlled oscillator (VCO) at Ku-band is designed. The proposed topology uses packaged NPN Silicon Germanium RF transistor and two parallel resonator structures connected to the device emitters. We proposed novel active open ended planar structure as a resonator for the VCO. Resonator is analyzed in terms of the required reflection coefficient and input impedance. Resonator's quality factor varies in between 159 and 235 as a function of tuning voltage. VCO microwave IC is fabricated on TMM10i [64] soft substrate with 17.5µm *Cr-Cu-Au* metallization process. VCO can be tuned for 180MHz by varying resonators' varactors from 0V to 22V. Measured output power remains in between 4.20dBm and 8.06dBm for the entire tuning range (14.89–15.06GHz). Measured phase noise is –145dBc/Hz at 1MHz offset with 8V tuning voltage. Normalized phase noise figure of merit (PNFOM) for the VCO is –214.4dBc/Hz. The circuit has low power consumption of 25.5mW and high DC to RF conversion efficiency ($\eta_{\text{DC-RF}}$).

5.1.1. Proposed Ku-band VCO

Fig. 5.1 shows the proposed novel voltage controlled negative resistance oscillator circuit topology. As $1/f$ noise is the significant contributor to the phase noise, bipolar RF transistors are preferable over HEMTs. The design uses an NPN Silicon Germanium NXP BFU725F bipolar RF transistor. It has low $1/f$ noise, 10–24dB gain and 0.42–1.1dB noise figure in 1.5–12GHz range. Hence, it makes the transistor perfectly suitable for VCO application. Open loop analysis was carried out to achieve a negative stability factor with gain $|S_{21}| > 1$ and $\angle S_{21} \sim 0^{\circ}$. Specific reflection coefficient applied to the emitter leads to both $|S_{11}|$ and $|S_{22}| > 1$ which is required to make the amplifier oscillating. Reflection coefficients being greater than one make real part of the impedance to be negative, while looking from the emitter end. Hence the topology is the negative resistance oscillator. From the analysis, it was concluded that there is further improvement seen in S_{11} and S_{22} when the device base is terminated with L_bC_b series resonant feedback. L_b is the high impedance 180µm line and C_b is the lumped capacitor. L_b and C_b are selected in a way that the S_{11} and S_{22} become maximum. R_1, R_2, C_3 and L_4 form a dedicated bias to the device. Large capacitor C_3 is used to bypass the

dc fluctuations due to power supply. L_1 and L_4 are 180µm *λ/4* high impedance lines. L_1 provides a dc return path for emitters and restricts the desired frequency being grounded. C_1 is 0.4pF capacitor from ATC [63] with 14GHz specific resonant frequency (SRF) and insertion loss better than –0.4dB in 8–24GHz band. C_{out} filters out the frequency components which are falling far from its SRF and also restricts the dc presence at the output due to collector bias.

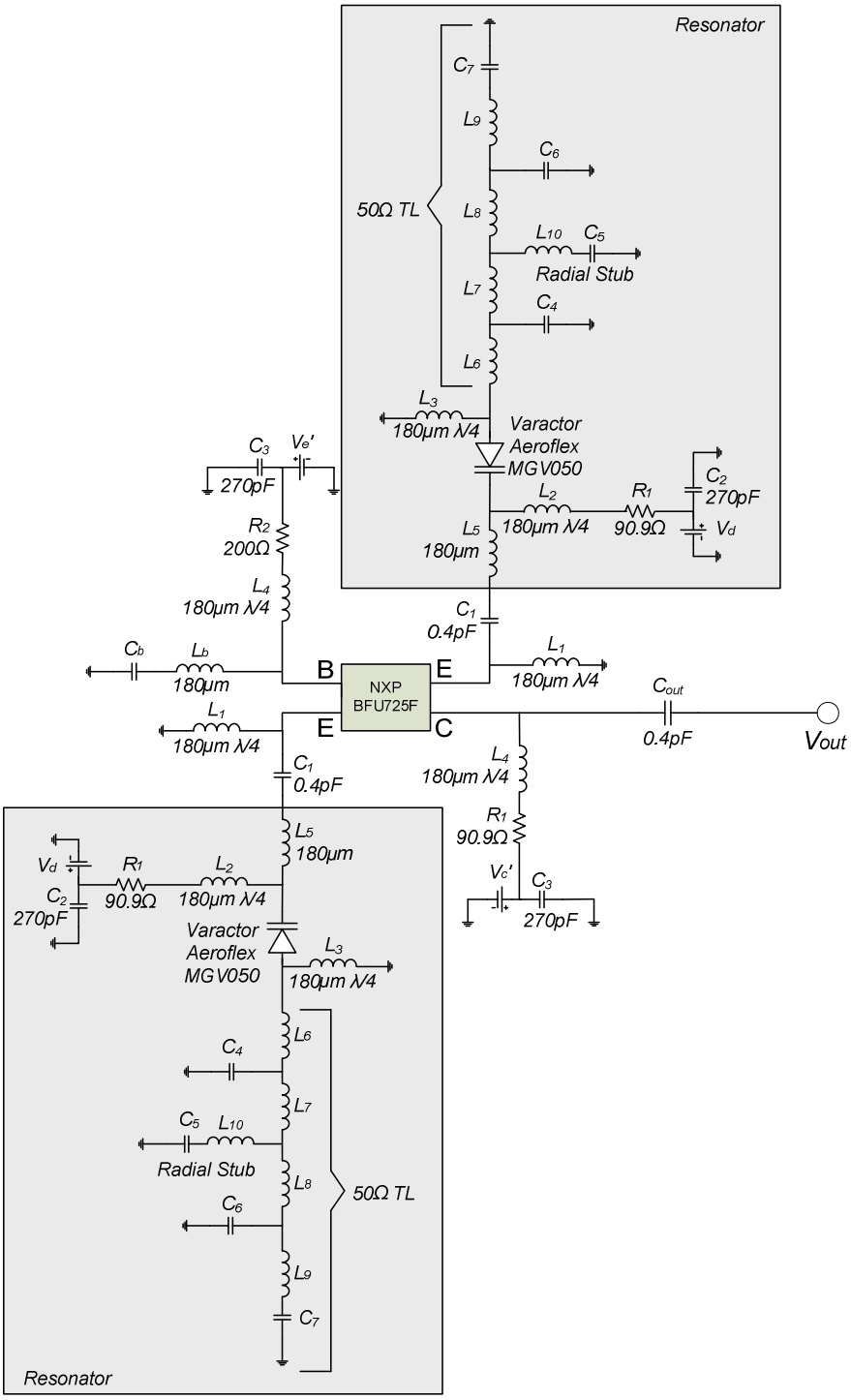

Fig. 5.1. Proposed Ku-band VCO

5.1.2. Proposed resonator analysis

The network which provides the specific reflection coefficient to the emitter is designed to be the resonator as shown in Fig. 5.2 which is extracted out from the Fig. 5.1. Frequency stability, and hence, the phase noise behavior of the circuit depends on the resonator design which makes it a crucial element in VCO. After analyzing the open loop amplifier's emitter reflection coefficient Γ_e (corresponding $Z_e = -R \pm jX$), a resonator network has to be designed with reflection coefficient Γ_{RES} (corresponding $Z_{RES} = R/3 \mp jX$). As the device has two emitters, it is not appropriate to run a long transmission line from two emitters surrounding the device base network and to connect it to a single resonator structure. As the encircling long transmission path may act as a resonator itself and also it will have electromagnetic coupling issues. More importantly, long transmission line for resonator will introduce extra loss which will degrade the resonator's quality factor performance. To avoid this, two parallel resonators are connected to both the emitters. Resonators are connected in such a way that the reflection coefficients do not differ from the analyzed values. For the same, resonator equivalent resistor *R* and, inductor *L* or capacitor *C* are analyzed. As both the device emitters are inherently in parallel, the connected individual resonators to both the emitters will also form a parallel network. Hence, the required equivalent values for individual resonator to provide the expected performance are resistor $R' = 2R$ and, inductor $L' = 2L$ or capacitor $C' = C/2$.

An identical resonator pair is connected to the two emitters, the way shown in the Fig. 5.1. The resonator networks use varactor diodes with a dedicated bias for each. L_6 to L_{10} and C_4 to C_7 form an open ended planar resonator network. The capacitor C_7 corresponds to the open ended transmission line. L_{10} and C_5 represent the equivalent open stub.

To achieve wide tuning bandwidth, all the stubs used in resonator and bias networks are the radial stubs. Resonators use Aeroflex GaAs MGV050 [69] series varactor diodes in reverse bias for tuning. L_3 corresponds to $\lambda/4$ high impedance line to provide a dc return path for the varactors and to restrict the RF to be grounded.

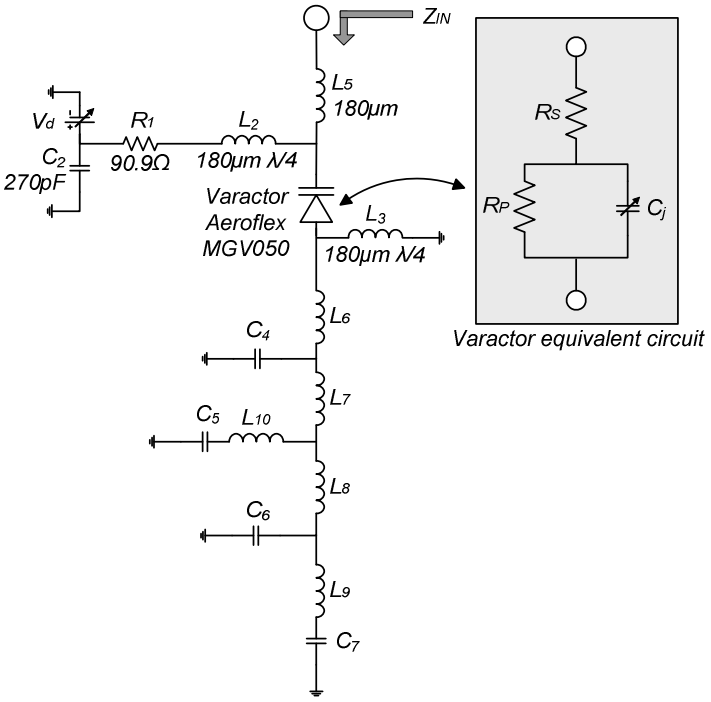

Fig. 5.2. Proposed planar active resonator

Abstractly, the input impedance of the resonator may be represented as,

$$Z_{in} \approx \left(R_s + \frac{R_P}{K_1} \right) + j\omega \left(L_5 + L_6 - \frac{K_2 K_3}{\omega^2 \left(-\omega^2 C_5 C_7 \left(L_8 + L_{10} \right) + \left(C_5 + C_7 \right) \right)} - \frac{R_P^2 C_j}{K_1} \right) \quad \ldots\ldots (5.1)$$

where,

$K_1 = 1 + \omega^2 R_P^2 C_j^2$

$K_2 = 1 - \omega^2 L_8 C_7$

$K_3 = 1 - \omega^2 L_{10} C_5$

Varactor junction capacitance, $C_j = f\left(V_d\right)$

In equation (5.1), conductor losses are not considered, only varactor diode's intrinsic resistances are taken into account. As varactor intrinsic resistances are present in the real part of the Z_{in}, they play an important role to sustain the oscillations. Here low loss varactor with small intrinsic resistors is selected to achieve a high quality factor of the planar resonator. Values of the resonator parameters can be selected accordingly so that the required X= *–imaginary(*Z_{in}*)*. However, in simulation it is found that the line lengths corresponding to L_5, L_6 and C_5 have the dominating role in tuning the resonator's input reflection coefficient.

After applying resonator networks to both the emitters; Barkhausen, Nyquist and Kurokawa criteria were checked to ensure the unstable region of operation and sustained oscillations.

5.1.3. Results and discussion

Fig. 5.3 shows the simulated open ended resonator's input return loss with respect to the frequency as a function of varactor tuning voltage. 0–22V variable varactor bias provides 200MHz tunability from 14.85GHz to 15.05GHz in Ku-band. Fig. 5.4 shows the calculated resonator Q-factor and varactor junction capacitance as a function of tuning voltage. Q-factor varies from 159 to 235 for 0V to 22V tuning range.

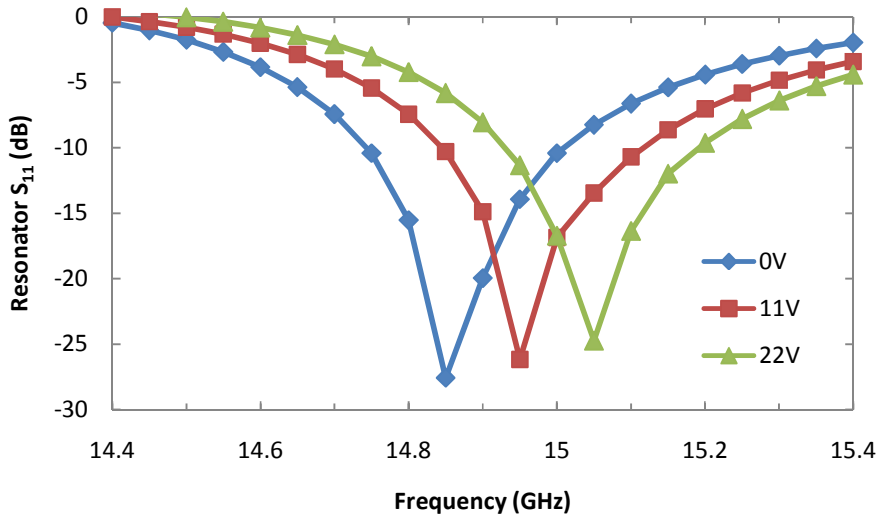

Fig. 5.3. Resonator response as a function of varactor bias

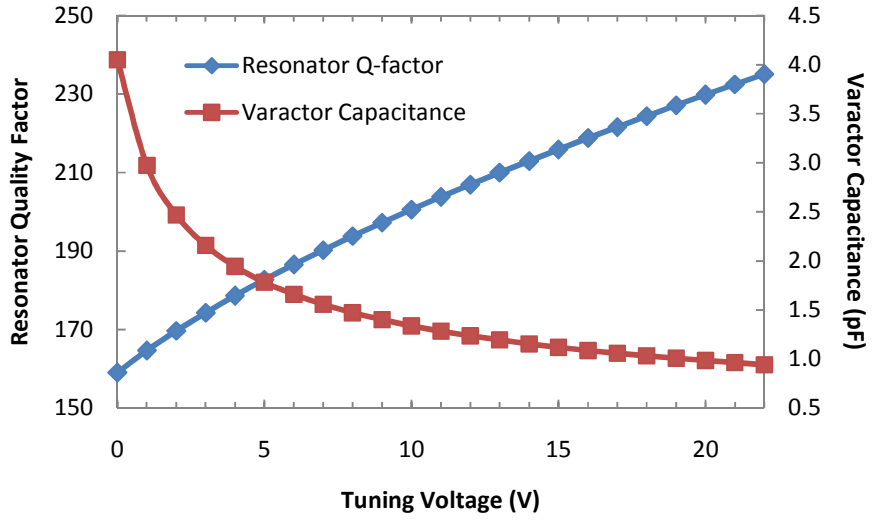

Fig. 5.4. Resonator Q-factor and varactor junction capacitance as a function of tuning voltage

The Ku-band VCO circuit is fabricated and tested. In this design, 25mil TMM10i [64] soft substrate is used for ease of providing via for immediate grounding. It has ε_r=9.8 and *tanδ*=0.0022 at 10GHz. Microwave IC is packaged in Aluminium test box. Upper cover height is considered to be at 11mm and it is electromagnetically modeled and simulated. Carrier plate was made from Kovar and was plated with Gold. Metallization process is *Cr-Cu-Au* with 17.5µm accuracy. Measured spectrum output is presented in Fig. 5.5 when varactors are biased at 8V. Measured fundamental tone is at 14.98 GHz with 6.87dBm output power. Fig. 5.6 shows the measured VCO oscillation frequency and output power as a function of varactor tuning voltage. VCO can be tuned for 180MHz in 14.89GHz to 15.06GHz range by varying resonators' varactors from 0V to 22V. Measured output power remains in between 4.20dBm and 8.06dBm for the entire tuning range. The device draws 8.5mA current at 3V resulting into very low 25.5mW dc power consumption. Fig. 5.7 represents the measured phase noise at 8V varactor bias. Measured phase noise is –60dBc/Hz at 1KHz offset and –145dBc/Hz at 1MHz offset from the carrier 14.98GHz. Normalized phase noise figure of merit (PNFOM) for VCO can be calculated using [70],

$$PNFOM = L(\Delta f) - 20\log_{10}\left(\frac{f_o}{\Delta f}\right) + 10\log_{10}\left(\frac{P_{DC}}{1mW}\right) \quad \ldots\ldots (5.2)$$

where, $L(\Delta f)$ is the phase noise at Δf offset frequency, f_o is the frequency of oscillation, and P_{DC} is the dc power consumption. The PNFOM of the developed VCO at 1MHz offset and 8V varactor bias is -214.4dBc/Hz. DC to RF efficiency may be defined as,

$$\eta_{DC-RF} = \frac{P_{RF}}{P_{DC}} \times 100\% \quad \ldots\ldots (5.3)$$

where, P_{RF} is the output signal power at the oscillation frequency. The DC to RF efficiency of VCO at 8V varactor bias is 19%. To the best of our knowledge, PNFOM and $\eta_{\mathrm{DC\text{-}RF}}$ are the best among the published planar resonator based VCOs in our frequency band of interest, to date. Fig. 5.8 shows the Ku-band voltage control oscillator fabricated microwave IC.

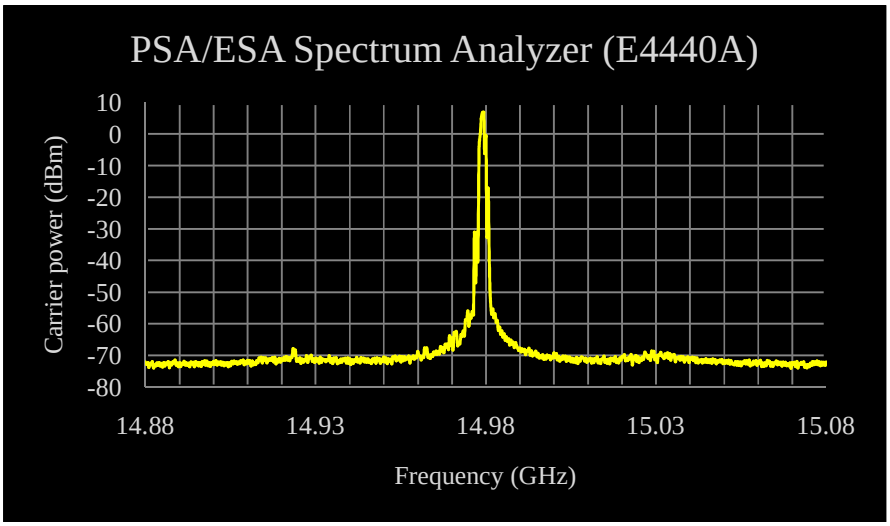

Fig. 5.5. VCO measured frequency spectrum at 8V varactor bias. Carrier frequency is 14.98GHz with 6.87dBm output power. Resolution BW= 1MHz. Span Frequency= 200MHz. Total number of points= 601. Instrument model: Agilent PSA E4440A

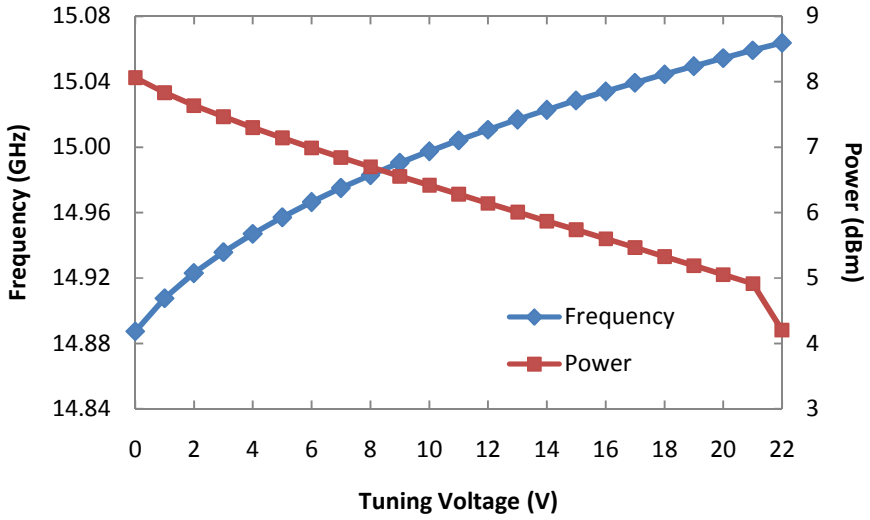

Fig. 5.6.VCO measured oscillation frequency and output power as a function of tuning voltage

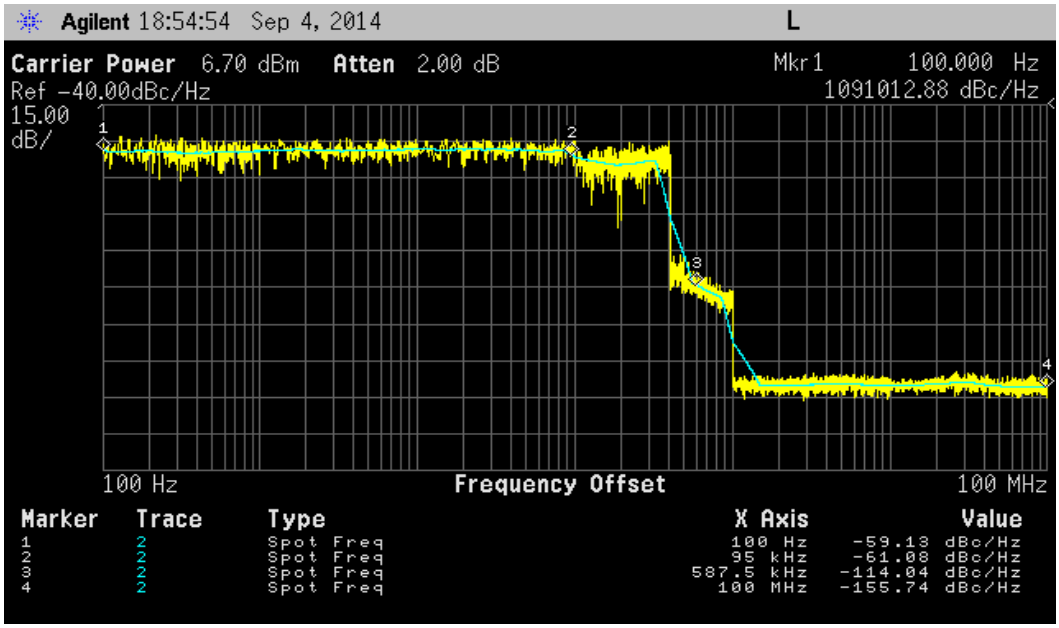

Fig. 5.7. Measured phase noise at 8V varactor bias

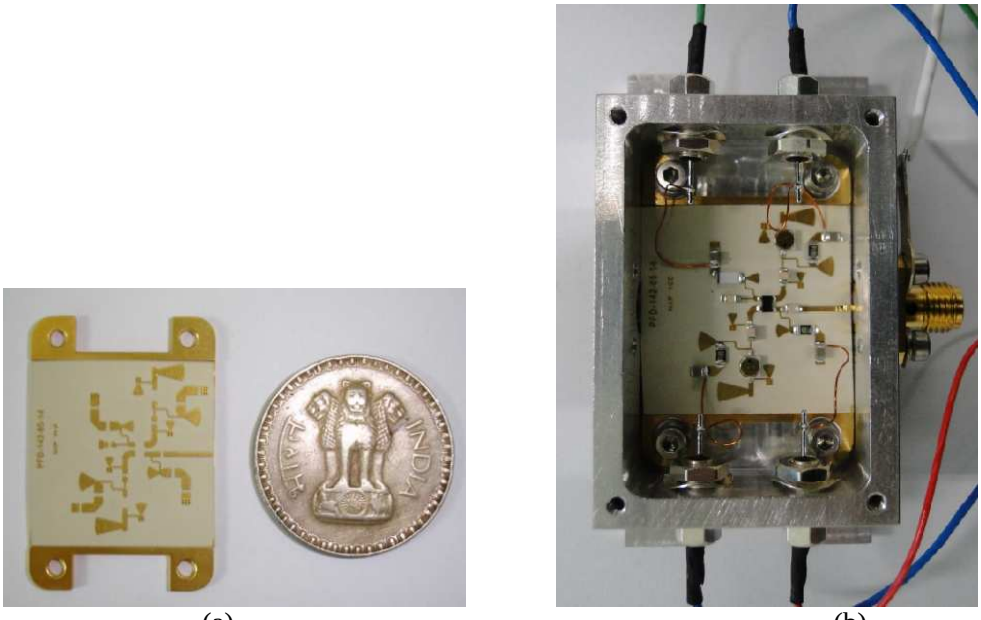

(a) (b)

Fig. 5.8. Fabricated VCO (a) Small size developed circuit layout on TMM10i substrate fitted on Kovar carrier plate. (b) packaged VCO microwave IC with top cover removed.

Comparative analysis in terms of various performance parameters of the proposed VCO with the published work in planar resonator oscillators is briefly carried out in Table 5.1. From the tabular analysis, it can be concluded that the developed small size Ku-band planar VCO has excellent simultaneous performances of very low power consumption, high DC-RF conversion efficiency, low phase noise and excellent PNFOM.

Table 5.1. Comparison with published planar oscillators

Reference	Device	Oscillation frequency f_o (GHz)	Output power P_{RF} (dBm)	Power consumption P_{DC} (mW)	DC to RF effi. $\eta_{DC\text{-}RF}$ (%)	Phase noise (dBc/Hz)	Offset frequency (KHz)	PNFOM (dBc/Hz)
[71]	InP/InGaAs DHBT	87	8 (max)	75 (VCO core)	8.41	-102	1000	-168.66
[72]	AlGaN/GaN HEMT	39.1	25	3900	8.11	-123	1000	-172.51
[28]	SiGe HBT	8.06	3.5	22.4	10	-122.5	100	-177
[73]	Si BJT	18.66	3.1 (max)	315	0.65 (max)	-123	1000	-183.3
[74]	HEMT	10	10	500	2	-112.05	100	-185.06
[75]	InGaP/GaAs HBT	12.09	12	168	9.43	-114.4	100	-193.8
[76]	InGaP/GaAs HBT	25	-1	90	0.88	-130	1000	-195
[34]	Si BJT	2.46	6.4	43.7	10	-144.47	1000	-195.76
[77]	SiGe HBT	9.1	9.7	66.6	14	-138	1000	-198.9
[29]	SiGe HBT	8	10	200	5	-150	1000	-205
This work	**SiGe HBT**	**14.98**	**6.9 (max 8.1)**	**25.5**	**19.1**	**-145**	**1000**	**-214.4**

5.2. Design of voltage-controlled oscillator using novel planar active metamaterial resonator (Design-2)

In this section, we have proposed another novel Ku-band VCO topology. The proposed topology uses two parallel planar resonator structures. We proposed novel double negative active metamaterial planar structure as a resonator for the VCO. Metamaterial resonator is analyzed and composite complex constituent parameters are extracted. Resonance achieved by metamaterial resonators determined the oscillator frequency which is 14.3 GHz at 11V varactor bias. VCO can be tuned for around 100MHz by varying resonators' varactor

from 0V to 22V. Planar resonator's loaded quality factor is calculated to be 305. The VCO microwave IC is fabricated on TMM10i soft substrate.

5.2.1. Proposed Ku-band VCO

In this topology, we replaced the resonator in Fig. 5.1 with the novel RF resonator. Infineon Technologies' CFY25-20 GaAs metal semiconductor field effect transistor [78] is used in the design. Device gate is connected with *active* tunable series *LC* network which helps to increase $|S_{11}|$ and $|S_{22}|$ further >1, leading to enough negative resistors at input and output ports.

5.2.2. Proposed resonator analysis

We proposed new planar active tunable metamaterial complementary split rings as resonators in the proposed topology as shown in Fig. 5.9. Fig. 5.9(a) shows the passive metamaterial structure of modified complimentary split ring resonators with included capacitive loaded strip. Proposed *active* metamaterial resonator is shown in Fig. 5.9(b).

Now, we carried out the constitutive parameter extraction by analyzing the metamaterial considering the free space characterization. First, passive metamaterial structure is analyzed using Ansoft HFSS. Metamaterial is inserted on the TMM10i standard substrate. TMM10i has ε_r=9.8 and $tan\delta$=0.0022 at 10GHz [64]. Now, uniform plane wave is incident on the sample. Material is treated as uniform composite in the direction of propagation.

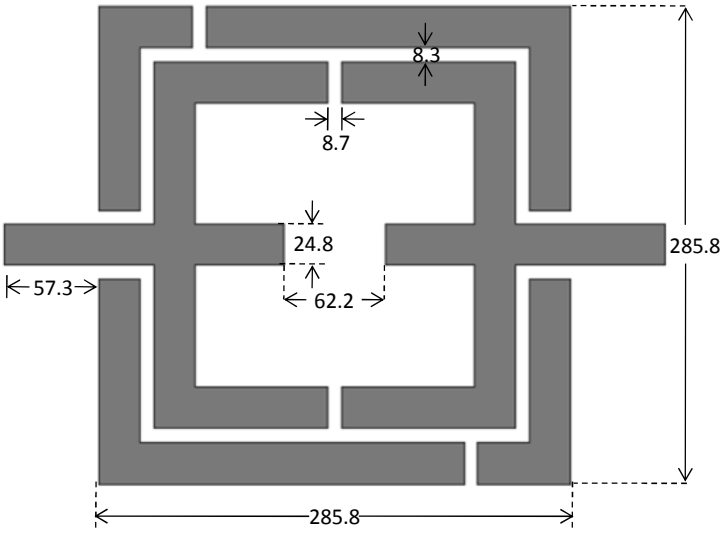

(a)

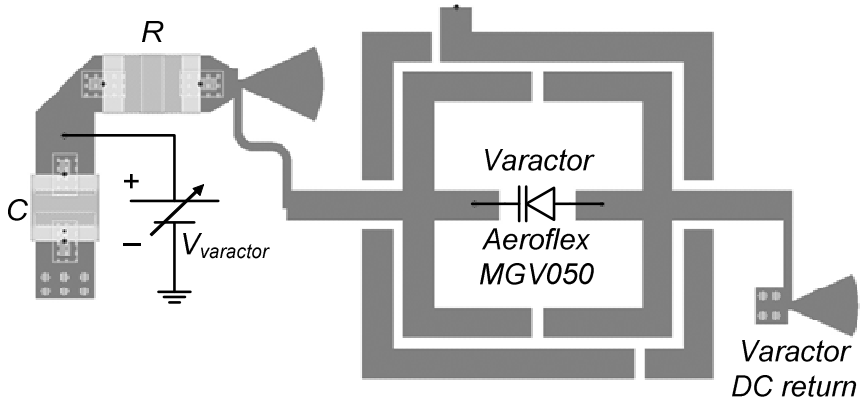

(b)

Fig. 5.9. (a) Proposed planar passive metamaterial resonator. Dimensions are in mil. (b) Proposed planar active metamaterial resonator.

Sample thickness in the direction of propagation *d*, is considered in odd multiples of the quarter wavelength to maximize S_{11}. Uncertainties in measurement of S_{11} are low for high values of $|S_{11}|$ which ensures effectiveness of constituent parameter extraction. Sample thickness *d* is kept at $3\lambda/4$ in our case, where λ is the guided wavelength. Material under test is the proposed metamaterial composite.

Uniform plane wave with linear polarization is normally incident on the sample. Considering the boundary conditions for the semi-infinite sample, parameters Γ and T were

calculated from the finite sample's reflection and transmission coefficients S_{11} and S_{21} respectively [79]. Γ and T are the reflection and transmission coefficients at the air-sample interface respectively. Considered $17.5\mu m$ metamaterial thickness takes care of the *Cr-Cu-Au* metallization process during fabrication. Still the thickness is very small and it can be treated as the planar inclusion in the analysis. Extraction of complex constituent parameters was analyzed by Ghodgaonkar [79] and can be written as,

$$\varepsilon = \frac{\gamma}{\gamma_0}\left(\frac{1-\Gamma}{1+\Gamma}\right), \quad \mu = \frac{\gamma}{\gamma_0}\left(\frac{1+\Gamma}{1-\Gamma}\right) \qquad \ldots\ldots (5.4)$$

where, γ = Propagation constant of the material under test. It is a function of *T*.

As mentioned in [79], calculated *T* is a complex quantity which gives multiple solutions for complex ε and μ for different possible values of *n*. *n* can be 0, ±1, ±2, ±3... However [79] narrates the extraction procedure for any dielectric material, equation (5.4) is also applicable to metamaterials because the material under test is assumed to be uniform in the direction of propagation. Hence, the extracted values will be composite complex ε and μ.

ε and μ straight away for the planar metamaterial structure was analyzed and given by Ziolkowski [80] and can be written as,

$$\varepsilon \sim \frac{2}{jk_0 d}\left(\frac{1-V_1}{1+V_1}\right), \quad \mu \sim \frac{2}{jk_0 d}\left(\frac{1-V_2}{1+V_2}\right) \qquad \ldots\ldots (5.5)$$

where, $V_1 = S_{21} + S_{11}, \quad V_2 = S_{21} - S_{11}$

Equation (5.5) is valid only if electrical thickness (k_{real}*d) of the sample is not too large [80]. In our case, k_{real}*d=0.8 which is less than 1 and hence the extraction method given in [80] is applicable to our proposed metamaterial structure.

In HFSS simulations, convergence was achieved by λ-refinement of 0.01048 based on the twice the center frequency of 14.3GHz and with 12 numbers of passes for the simulation. The number of tetrahedras used were 24697 and *S*-parameter variations ΔS, was 0.00263.

To overcome the discrepancy of multiple solutions [79], two samples with different thicknesses can be considered. Solution of n is the one for which extracted ε and μ are same for two different samples with thicknesses d_1 and d_2. However, by analyzing the different n values and comparing the extracted complex ε and μ results with the Ziolkowski's method [80] results, it was concluded that for our proposed design n=2 is the most appropriate case.

Fig. 5.10(a)–(d) show simulated results of the extracted composite complex permittivity and permeability considering two methods discussed by Ghodgaonkar [79] and Ziolkowski [80]. Results are reported in the range of interest from 14GHz to 14.5GHz. It can be seen that the simultaneous negative region is roughly matching in both the techniques. Still, real part of permittivity resonance seems good in Ziolkowski's method while real part of permeability resonance seems good in Ghodgaonkar's method. Taking both the methods into account, it can be concluded that the proposed metamaterial has a simultaneous negative permittivity and negative permeability present in 14.20–14.48GHz range.

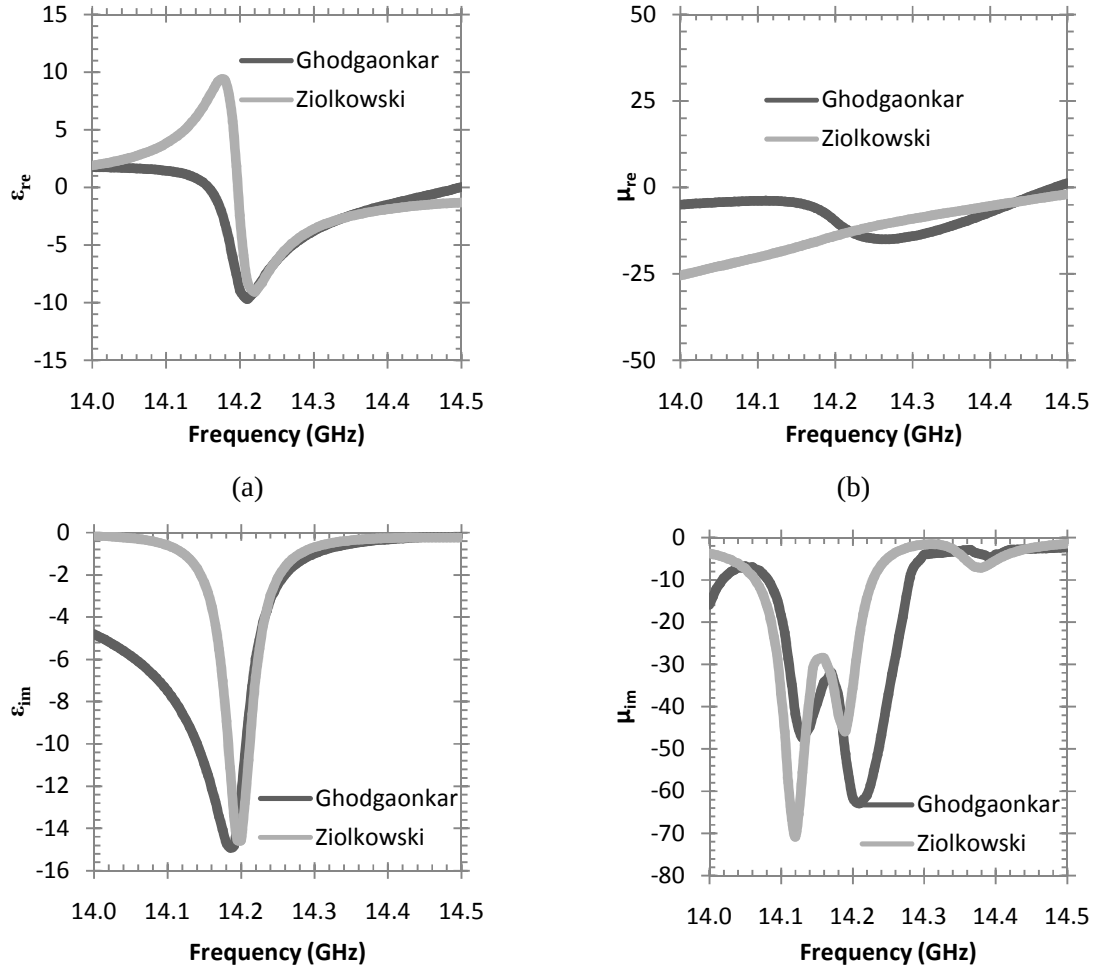

Fig. 5.10. Extracted complex constituent parameters calculated from simulated S-parameters. For proposed metamaterial: (a) real part of permittivity (b) real part of permeability (c) imaginary part of permittivity (d) imaginary part of permeability

Now, consider an active metamaterial resonator presented in Fig. 5.9(b). Aeroflex MGV050 varactor diode is introduced for frequency tuning. It has a dedicated bias network and dc ground return path designed at the desired frequency. Radial stubs ensure wideband open circuit in the desired frequency band of 14GHz to 14.5GHz. Hence, introduced supporting networks required for the varactor diode does not change the electromagnetic behavior of the passive metamaterial in the desired frequency band. Hence, it can be concluded that the active metamaterial also exhibits double negative region at the same frequency at which the passive metamaterial structure does. The same was proved by exporting multiport S-parameter data from HFSS to Keysight Technologies' ADS.

Co-simulation results are presented in Fig. 5.11 for various varactor biases. It clearly shows that at 0V varactor bias, resonant peak is achieved at 14.25GHz which is in the double negative region for the passive metamaterial resonator as shown in Fig. 5.10. Simulated loaded quality factor of the resonator is 305 at 14.3GHz for 11V varactor bias.

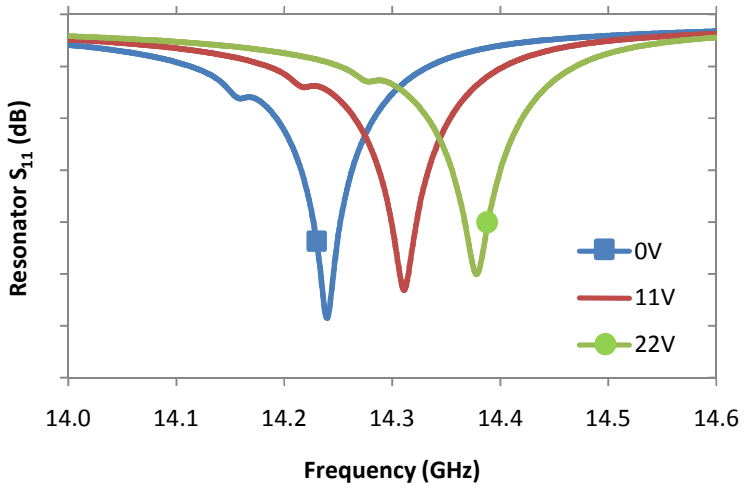

Fig. 5.11. Proposed resonator frequency tuning. By varying varactor bias from 0V to 22V, 150MHz tuning is achieved in simulation.

Two active planar metamaterial resonators are connected in parallel to the two sources of the device as shown in the Fig. 5.1. Varying the varactor bias in the active resonator provides VCO frequency tuning of nearly 100MHz while measurements. Varactor connected to the device gate provides enhanced control in VCO tuning.

Measurement result is presented when resonators' varactors are biased at 11V. Measured carrier power is 10.37dBm at 14.315GHz as shown in Fig. 5.12. Measured phase noise is –65dBc/Hz at 1KHz offset and –120dBc/Hz at 5MHz offset from the carrier 14.315GHz which can be seen from the Fig. 5.13. However, the device used in this VCO design-2 has the comparatively high 1/*f* noise with respect to the HBT used in previous VCO design-1. Hence, design-2 has the poor phase noise performance compare to the design-1, although the quality factor of the metamaterial resonator is better than the quality factor of the resonator used in the previous design-1. Fig. 5.14 shows the complete fabricated microwave IC. In this design, 25mil soft substrate TMM10i [64] is used for ease of providing via for immediate grounding. Upper cover height is considered as 433mil and it is

electromagnetically modeled and simulated. The circuit draws 23mA current at 2.4V resulting in 55mW dc power consumption.

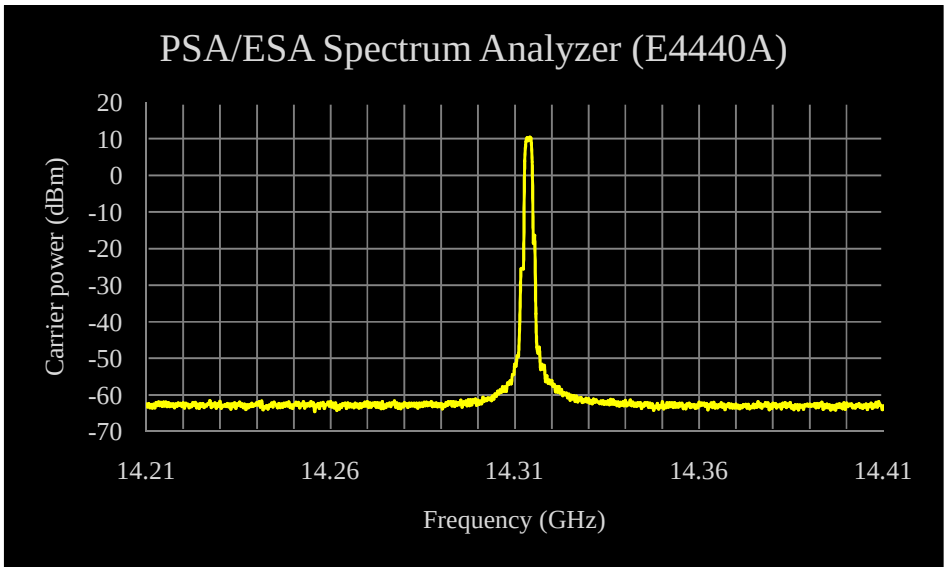

Fig. 5.12. Measured Ku-band VCO spectrum ($V_{varactor}$=11V) Measured carrier power is 10.37dBm at 14.315GHz. Resolution BW=1MHz.

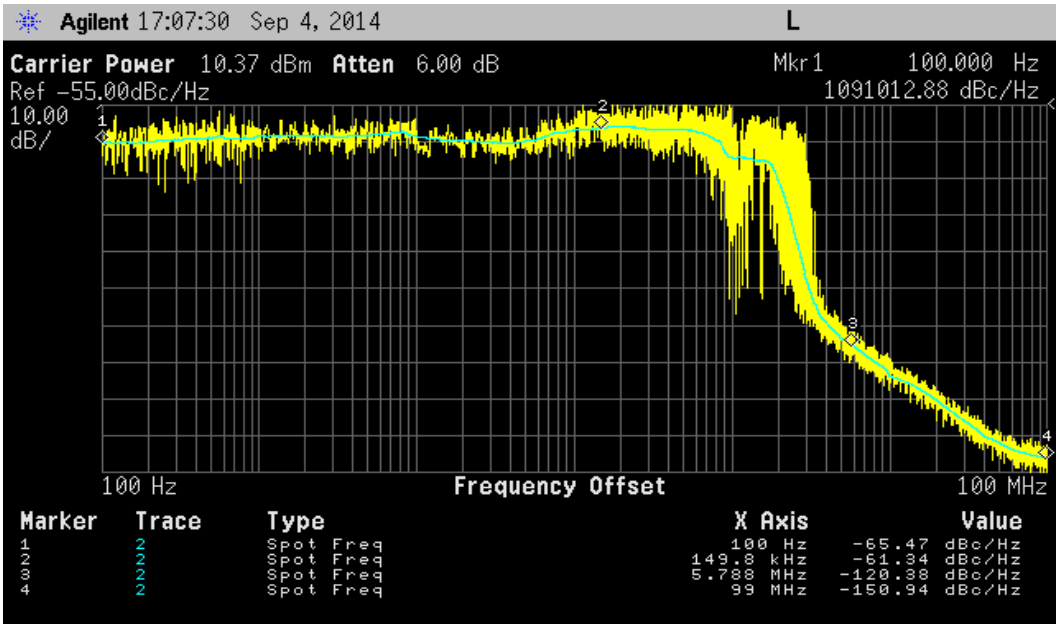

Fig. 5.13. Measured phase noise at 11V varactor bias

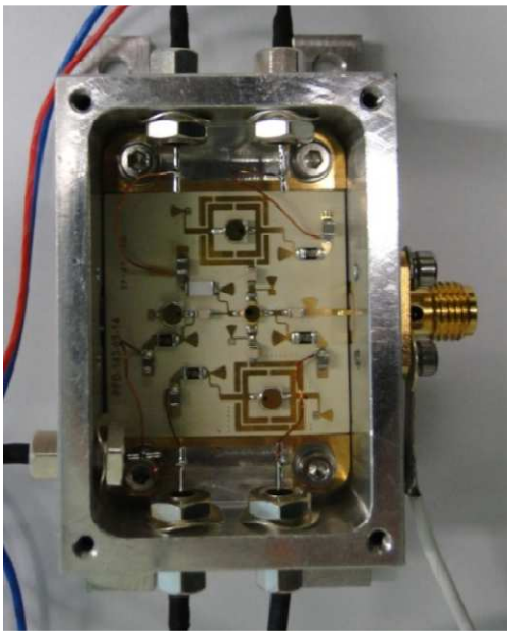

Fig. 5.14. Fabricated VCO microwave IC using active tunable planar metamaterial resonator with space grade technology

5.3. Chapter conclusions

Two different new topologies of the negative resistance voltage-controlled oscillators at Ku-band were proposed. In VCO design-1, we proposed novel active open ended planar structure as a resonator for the VCO. Even though being a planar resonator, it provides very good quality factor (up to 235) which ensures the low phase noise. VCO microwave IC was fabricated and tested. Measurements show that the VCO can be tuned for 180MHz by varying resonators' varactors from 0V to 22V. Measured output power remains in between 4.20dBm and 8.06dBm for the entire tuning range. Measured PNFOM for the VCO is –214.4dBc/Hz. The DC to RF efficiency ($\eta_{\text{DC-RF}}$) of VCO is 19%. To the best of our knowledge, PNFOM and $\eta_{\text{DC-RF}}$ are the best among the published planar resonator based VCOs, to date. In VCO design-2, we proposed novel double negative active metamaterial planar structure as a resonator. Metamaterial resonator was analyzed and composite complex constituent parameters were extracted. Metamaterial resonator has an improved quality factor compare to the resonator proposed in design-1. The IC was fabricated and tested. Measurements show 10.37dBm power at 14.3GHz which is improved compare to the VCO design-1.

Chapter 6

Conclusions and Suggestions for Future Work

A novel receiver front-end; LNA, mixer and oscillator, was designed and analyzed in Ku-band. Different design aspects of the subsystems along with the trade-offs and improvements were presented.

Two designs of three-stage Ku-band low noise amplifier were presented. The performance parameters of the LNA were improved by minimizing the correlated noise of the cascaded system. The improved design had the 30dB gain with 1.46dB noise figure. The measurement results were compared with the large number of relevant work published in Ku-band. It was concluded that the design presented has the excellent results with simultaneously very low noise figure and high gain with low power consumption.

Next, we presented a wideband 3-dB balanced coupler for the mixer application. Typical rat-race coupler was modified by introducing CRLH transmission line in $3\lambda/4$ branch to provide wideband response. Proposed coupler is small in size (4.3mm X 4.3mm) and provides wideband response in 13–16GHz. Using the coupler presented; small size wideband singly balanced passive mixer in Ku-band was designed. Mixer simulated results are presented in terms of mixer performance parameters, conversion loss, noise figure and linearity. Proposed mixer has low conversion loss and very good LO-to-RF isolation in Ku-band. The mixer exhibited good linear response; 1-dB compression was at 4dBm RF power, and IIP_3 is at 15.7dBm RF power. Two-stage multiband-reject IF filter was designed and simulated to suppress– RF, LO frequency, 2^{nd} order intermodulation products ($2LO$, $2RF$ and $LO+RF$), and 3^{rd} order intermodulation products ($2RF–LO$ and $2LO–RF$).

Two different new topologies of negative resistance voltage-controlled oscillators at Ku-band were proposed. In VCO design-1, we proposed novel active open ended planar structure as a resonator for the VCO. Even though being a planar resonator, it provides very

good quality factor (up to 235) which ensures low phase noise. VCO microwave IC was fabricated and tested. Measurements showed that the VCO can be tuned for 180MHz by varying resonators' varactors from 0V to 22V. Measured output power remained in between 4.20dBm and 8.06dBm for the entire tuning range. Measured PNFOM for the VCO is −214.4dBc/Hz. The DC to RF efficiency ($\eta_{\text{DC-RF}}$) of VCO is 19%. To the best of our knowledge, PNFOM and $\eta_{\text{DC-RF}}$ are the best among the published planar resonator based VCOs, to date. In VCO design-2, we proposed novel double negative active metamaterial planar structure as a resonator. Metamaterial resonator was analyzed and composite complex constituent parameters were extracted. Metamaterial resonator has an improved quality factor compare to the resonator proposed in design-1. The IC was fabricated and tested. Measurements show 10.37dBm power at 14.3GHz which is improved compare to the VCO design-1.

The work presented here may be extended as follows:

1. Noise cancellation LNA

   LNA feedback configurations can be modeled accordingly in order to achieve the noise cancellation properties. From the MIC experimental aspects, carrier plates need to be modified accordingly to accommodate feedback paths and to provide immediate grounding in case if brittle alumina substrate is to be used.

2. Receiver front-end on chip with integrated antenna

   The whole receiver front-end can be engineered on a single chip with active integrated antenna. It has significant electromagnetic coupling challenges are to be taken care-off. One more important aspect is, planar antenna requires low permittivity substrate for better radiation efficiency, while the active circuit on the same chip requires high permittivity substrate. Hence, the trade-off is to be analyzed in order to have optimized performance parameters.

3. Instead of the passive mixer presented here, active mixer can be designed which exhibits conversion *gain*. In the presented mixer, tunable coupler may be introduced in order to achieve desired frequency response.

References

[1] "Millimeter wave propagation: spectrum management implications", Federal Commun. Commission, Washington, DC, pp.1-24, July, 1997.

[2] Harald T. Friis, "Noise Figure of Radio Receivers," *proc. I.R.E.*, vol. 32, no. 7, pp. 419-422, July 1944.

[3] Guillermo Gonzalez, *Microwave transistor amplifiers: analysis and design*, 2nd edi., New Jersey, Prentice Hall, 1996.

[4] Pospieszalski, M.W., "Modeling of Noise Parameters of MESFET's and MODFET's and Their Frequency and Temperature Dependence," *IEEE Trans. Microw. Theory Tech.*, vol. 37, no. 9, pp. 1340–1350, Sept. 1989.

[5] Felgentreff, T., Olbrich, G., Russer, P., "Noise parameter modeling of HEMTs with resistor temperature noise sources," in *Proc. IEEE MTT-S Int. Microw. Symp. Dig.*, San Diego, CA, USA, May 1994, pp. 853–856.

[6] Sungjae Lee, Webb, K.J., Tilak, V., Eastman, Lester F., "Intrinsic Noise Equivalent-Circuit Parameters for AlGaN/GaN HEMTs," *IEEE Trans. Microw. Theory Tech.*, vo. 51, no. 5, pp. 1567–1577, May 2003.

[7] Chen, Guang, Kumar, V., Schwindt, R.S., Adesida, I., "A low gate bias model extraction technique for AlGaN/GaN HEMTs," *IEEE Trans. Microw. Theory Tech.*, vol. 54, no. 7, pp. 2949–2953, July 2006.

[8] Jarndal, A., Kompa, G., "A New Small-Signal Modeling Approach Applied to GaN Devices," *IEEE Trans. Microw. Theory Tech.*, vol. 53, no. 11, pp. 3440–3448, Nov. 2005.

[9] Jarndal, A., Markos, A.Z., Kompa, G., "Improved Parameter Extraction Method for GaN HEMT on Si Substrate," in *Proc. IEEE MTT-S Int. Microw. Symp. Dig.*, Anaheim, CA, May 2010, pp. 1668–1671.

[10] Liu, Z.H., Arulkumaran, S., Ng, G.I., "Temperature dependent microwave noise parameters and modeling of AlGaN/GaN HEMTs on Si substrate," in *Proc. IEEE MTT-S Int. Microw. Symp. Dig.*, Boston, MA, June 2009, pp. 777–780.

[11] Zhang, X., Lin, B., Chau, F., "An Accurate Scalable Nonlinear Model for GaAs E-pHEMT and Low Noise Amplifiers," in *Proc. 2012 7th European Microw. Integr. Circuits Conf.*, Amsterdam, Oct. 2012, pp. 167–170.

[12] Stephen A. Maas, *Nonlinear microwave and rf circuits*, 2nd edi., Norwood, MA, Artech House Inc., 2003.

[13] Stephen A. Maas, *Microwave mixers*, Norwood, MA, Artech House Inc., 1993.

[14] Itoh, T., Pei-Ling Chi, Cheng-jung Lee, "Compact dual-band metamaterial-based hybrid ring coupler," U.S. Patent 8 072 291 B2, Dec. 6, 2011.

[15] Veselago, V.G., "The electrodynamics of substances with simultaneously negative values of ε and μ," *Sov. Phys.—Usp.*, vol. 10, no. 4, pp. 509–514, Jan.–Feb. 1968.

[16] Smith, D.R., Padilla, W.J., Vier, D.C., Nemat-Nasser, S.C., Schultz, S., "Composite medium with simultaneously negative permeability and permittivity," *Phys. Rev. Lett.*, vol. 84, no. 18, pp. 4184–4187, May 2000.

[17] Shelby, R.A., Smith, D.R., Schultz, S., "Experimental verification of a negative index of refraction," *Science*, vol. 292, no. 5514, pp. 77–79, Apr. 2001.

[18] Sanada, A., Caloz, C., Itoh, T., "Planar distributed structures with negative refractive index", *IEEE Trans. Microw. Theory Tech.*, vol. 52, no. 4, pp.1252–1263, 2004.

[19] Kim, T.-G., Lee, B., "Metamaterial-based wideband rat-race hybrid coupler using slow wave lines," *IET Microw. Antennas Propag.*, vol. 4, iss. 6, pp.717–721, 2010.

[20] Pei-Ling Chi, Itoh, T., "Miniaturized dual-band directional couplers using composite right/left-handed transmission structures and their applications in beam pattern diversity systems," *IEEE Trans. Microw. Theory Tech.*, vol. 57, no. 5, pp.1207-1215, May 2009.

[21] Liu, K.Y., Li, C., Li, F., "A New Type of Microstrip Coupler with Complementary Split-Ring Resonator (CSRR)," *Progress in Electromagnetics Research*, vol. 3, no. 5, pp.603-606, 2007.

[22] Ma, Y., Zhang, H., Li, Y., "Novel symmetrical coupled-line direction coupler based on resonant-type composite right-/left-handed transmission lines," *Progress in Electromagnetics Research*, vol. 140, pp.213-226, 2013.

[23] Alimenti, F., Mezzanotte, P., Giacomucci, S., Dionigi, M., Mariotti, C., Virili, M., Roselli, L., "24 GHz single-balanced diode mixer exploiting cellulose-based materials," *IEEE Microw. And Wireless Component Lett.*, vol. 23, no. 11, pp.596-598, Nov. 2013.

[24] Guillermo Gonzalez, "Negative-resistance oscillators," in *Foundations of oscillator circuit design*, Norwood, MA, Artech House Microwave Library, 2007, ch. 5, pp. 251-350.

[25] Kurokawa, K., ''Some Basic Characteristics of Broadband Negative Resistance Oscillator Circuit,'' *Bell System Technical Journal*, vol. 48, pp. 1937–1955, July 1969.

[26] Jankovic, M., “Design method for low-power, low phase noise voltage-controlled oscillators,” in *Proc. of 2nd European Microwave Integrated Circuits Conf.*, Munich, 08-10 Oct, 2007, pp. 199-202.

[27] Morteza, N., Mortazawi, A., “Oscillator phase-noise reduction using low-noise high-Q active resonators,” in *Proc. 2010 IEEE MTT-S Int. Microwave Symp. Dig.*, Anaheim, CA, 23-28 May 2010, pp. 276 – 279.

[28] Choi, J., Mortazawi, A., “Low phase-noise planar oscillators employing elliptic-response bandpass filters,” *IEEE Transactions on Microwave Theory and Techniques*, vol. 57, no.8, pp. 1959 -1965, Aug. 2009.

[29] Morteza, N., Mortazawi, A., “Low phase-noise planar oscillators based on low-noise active resonators,” *IEEE Transactions on Microwave Theory and Techniques*, vol. 58, no.5, pp. 1133-1139, May 2010.

[30] Morteza, N., Mortazawi, A., “A very low phase-noise voltage-controlled-oscillator at X-band,” in *Proc. 2011 IEEE MTT-S Int. Microwave Symp. Dig.*, Baltimore, MD, 5-10 June 2011, pp. 1-4.

[31] Yan Cheng, “Study on partitioning design approach on K-band oscillator design,” Ph.D. dissertation, Dept. Elect. Eng., Kassel University, Kassel, Germany, Oct., 2004.

[32] Rohde, U.L., Poddar, A.K., “Novel multi-coupled line resonators replace traditional ceramic resonators in oscillators/VCOs,” in *Proc. IEEE Int. Frequency Control Symp. and Expo.*, Miami, FL, June, 2006, pp. 432-442.

[33] Jin, T., Zhou, J., “A low phase noise X-band push-push VCO with microstrip resonator,” in *Proc. Int. Conf. on Microwave and Millimeter Wave Technology*, Nanjing, 21-24 April, 2008, pp. 274–276.

[34] Chih-Lin Chang, Chao-Hsiung Tseng, “Design of low phase-noise oscillator and voltage-controlled oscillator using microstrip trisection bandpass filter,” *IEEE Microw. Compon. Lett.*, vol. 21, no. 11, pp. 622–624, Nov. 2011.

[35] Chao-Hsiung Tseng, Chih-Lin Chang, “Design of low phase-noise microwave oscillator and wideband VCO based on microstrip combline bandpass filters,” *IEEE Trans. Microw. Theory Techn.*, vol. 60, no. 10, pp. 3151–3160, Oct. 2012.

[36] Byeong-Taek Moon, Noh-Hoon Myung, “Design of low phase-noise oscillator based on a Hairpin-shaped resonator using composite right/left-handed transmission line,” *IEEE Microw. Compon. Lett.*, vol. 24, no. 1, pp. 44–46, Jan 2014.

[37] Aldert Van Der Ziel, “Noise in solid-state devices and lasers,” in *Proceedings of the IEEE*, vol. 58, no. 8, pp.1178-1206, Aug. 1970.

[38] Behezad Razavi, *RF microelectronics*, New Jersey, Prentice Hall, 1998.

[39] Thomas H. Lee, *The design of CMOS radio-frequency integrated circuits*, Cambridge, Cambridge University Press, 1998.

[40] Vishay. *Applicat. note CRCW0805* [Online]. Available: http://www.vishay.com

[41] Infineon Technologies. *Applicat. note CFY67-08P* [Online]. Available: http://www.infineon.com

[42] Narda Microwave-east. *Applicat. note 4428C-2* [Online]. Available: http://www.nardamicrowave.com

[43] Rothe, H., Dahlke, W., “Theory of noisy four poles,” *Proceedings I.R.E.*, pp.811-818, 1956.

[44] Dambrine, G., Cappy, A., Heliodore, F., Playez, E., “A new method for determining the FET small-signal equivalent circuit,” *IEEE Trans. Microw. Theory Tech.*, vol. 36, no. 7, pp.1151–1159, July 1988.

[45] Berroth, M., Bosch, R., “Broad-band determination of the FET small-signal equivalent circuit,” *IEEE Trans. Microw. Theory Tech.*, vol. 38, no. 7, pp.891–895, July 1990.

[46] Susumu Co. *Applicat. note RL05S3.3* [online]. Available: http://www.susumu.co.jp

[47] Chang-Kun Park, Min-Gun Kim, Chung-Han Kim, Songcheol Hong, “Ku-band low noise amplifier with using short-stub ESD protection,” in *Proc. IEEE MTT-S International Microwave Symposium Digest*, Philadelphia, PA, USA, 8-13 June, 2003, vol. 1, pp. A157-A160.

[48] Yamanaka, K., Yamauchi, K., Mori, K., Ikeda, Y., Ikematsu, H., Tanahashi, N., Takagi, T., “Ku-band low noise amplifier MMIC amplifier with bias circuit for compensation of temperature dependence and process variations,” in *Proc. IEEE MTT-S Int. Microwave Symp. Dig.*, vol. 3, June 2002, pp. 1427–1430.

[49] Resca, D., Scappaviva, F., Florian, C., Rochette, S., Muraro, J.-L., di Giacomo Brunel, V., Chang, C., Baglieri, D., “A Robust Ku-Band Low Noise Amplifier using an Industrial 0.25-

µm AlGaN/GaN on SiC Process," in *Proc. of the 43rd European Microwave Conference*, Nuremberg, Germany, 7-10 Oct, 2013, pp. 1467-1470.

[50] Suijker, E.M., Rodenburg, M., Hoogland, J.A., van Heijningen, M., Seelmann-Eggebert, M., Quay, R., Bruckner, P., van Vliet, F.E., "Robust AlGaN/GaN Low Noise Amplifier MMICs for C-, Ku- and Ka-band Space Applications," *Annual IEEE Compound Semiconductor Integrated Circuit Symposium*, Greensboro, NC, 11-14 Oct. 2009, pp. 1-4.

[51] Aspemyr, L., Jacobsson, H., Bao, M., Sjoland, H., Ferndahl, M., Carchon, G., "A 15 GHz and a 20 GHz low noise amplifier in 90 nm RF-CMOS," *Silicon Monolith. Integr. Circuits RF Syst. Conf. Tech. Dig.*, San Diego, CA, Jan. 2006, pp. 387–390.

[52] Phan, K., Morkner, H., "A High Performance Yet Easy to Use Low Noise Amplifier in SMT Package for 6 to 20 GHz Low Cost Applications," *34th European Microwave Conference,* Amsterdam, 2004, pp. 365-368.

[53] Shu-Jenn Yu, Wei-Chou Hsu, Ching-Sung Lee, Chian-Sern Chang, Chang-Luen Wu, Ching-Hsueh Chang, "A Ku-band three-stage MMIC low-noise amplifier with superiorly low thermal sensitivity coefficients," *Microw. and Optical Technol. Lett.*, vol. 49, no. 7, pp. 1637-1641, July 2007.

[54] Zirath, H., Sakalas, P., Miranda, J.M., "A low noise 2-20 GHz feedback MMIC-amplifier," in *Proc. IEEE Radio Frequency Integrated Circuits Symp.*, Boston, MA, USA, 10-13 June 2000, pp. 169-172.

[55] Knapp, H., Zoschg, D., Meister, T., Aufinger, K., Boguth, S., Treitinger, L., "15 GHz wideband amplifier with 2.8 dB noise figure in bipolar technology," in *Proc. IEEE Radio Frequency Integrated Circuits Symp.*, June 2001, pp. 287–290.

[56] Ellis, G.A., Jeong-sun Moon, Wong, D., Micovic, M., Kurdoghlian, A., Hashimoto, P., Hu, Ming, "Wideband AlGaN/GaN HEMT MMIC Low Noise Amplifier," in *Proc. IEEE MTT-S International Microwave Symposium Digest*, 6-11 June 2004, vol. 1, pp. 153-156.

[57] Kuo-Liang Deng, Ming-Da Tsai, Chin-Shen Lin, Kun-You Lin, Huei Wang, Wang, S.H., Lien, W.Y., Chem, G.J., "A Ku-band CMOS Low-Noise Amplifier," in *Proc. IEEE International Workshop on Radio-Frequency Integration Technology*, Singapore, Nov 30-Dec 02, 2005, pp. 183-186.

[58] Ellinger, F., Jäckel, H., “Low-Cost BiCMOS Variable Gain LNA at Ku-Band With Ultra-Low Power Consumption,” *IEEE Transactions on Microwave Theory and Techniques*, vol. 52, no. 2, pp. 702-708, Feb 2004.

[59] Schad, K.-B., Urben, U., Soenmez, E., Abele, P., Schumacher, H., “A Ku Band SiGe Low Noise Amplifier," *Topical Meetings on Silicon Monolithic Integrated Circuits in RF Systems,* Garmisch, Germany, 28 April 2000, pp. 52–54.

[60] Wen-Lin Chen, Sheng-Fuh Chang, Guo-Wei Huang, Yuh-Sheng Jean, Ta-Hsun Yeh, “A Ku-Band Interference-Rejection CMOS Low-Noise Amplifier Using Current-Reused Stacked Common-Gate Topology,” *IEEE Microwave and Wireless Components Lett.*, vol. 17, no. 10, pp. 718-720, Oct 2007.

[61] Gil, J., Han, K., Shin, H., “A 13-GHz 4.67-dB NF CMOS low noise amplifier,” *Electron. Lett.*, vol. 39, no. 14, pp. 1056–1058, Jul. 2003.

[62] Girlando, G., Ferla, G., Ragonese, E., Palmisano, G., “Silicon bipolar LNAs in the X and Ku bands,” in *Proc. Int. Conf. on Electronics, Circuits and systems*, vol. 1, Sept. 2002, pp. 113–116.

[63] American Technical Ceramics (ATC). *Applicat. Note ATC100A CDR12* [Online]. Available: http://www.atceramics.com

[64] Rogers corp. *Applicat. note TMM10i* [Online]. Available: http://www.rogerscorp.com

[65] Aeroflex corp. *Applicat. note MSS20,143-B10D* [Online].
Available: http://www.aeroflex.com/metelics

[66] Ki-Byoung Kim, Tae-Soon Yun, Jong-Chul Lee, “A Single Balanced Diode Mixer with Defected Ground Structure (DGS) Lowpass Filter (LPF),” in *Proc. 34th European Microwave Conference*, Amsterdam, Netherlands, 12-14 Oct. 2004, pp. 197 – 200.

[67] Wei Zhao, Yong Zhang, Mingzhou Zhan, “Design and Performance of a W-Band Microstrip Rat-Race Balanced Mixer,” in *Proc. International Conference on Microwave and Millimeter Wave Technology*, Chengdu, China, 8-11 May 2010, pp. 713 – 716.

[68] Panasonic Corp. *Applicat. note ERJ-1* [Online].
Available: http://www.industrial.panasonic.com

[69] Aeroflex Corp. *Applicat. note MGV050-H20* [Online].
Available: http://www.aeroflex.com/metelics

[70] Tiebout, M., “Low-power low-phase-noise differentially tuned quadrature VCO design in standard CMOS,” *IEEE J. Solid-State Circuits*, vol. 36, no. 7, pp. 1018–1024, July 2001.

[71] Makon, R.E., Driad, R., Schneider, K., Maßler, H., Aidam, R., Quay, R., Schlechtweg, M., Weimann, G., “Fundamental low phase noise InP-based DHBT VCO operating up to 89 GHz,” *Electron. Lett.*, vol. 41, no. 17, pp. 961–963, Aug. 2005.

[72] Lan, X., Wojtowicz, M., Smorchkova, I., Coffie, R., Tsai, R., Heying, B., Truong, M., Fong, F., Kintis, M., Namba, C., Oki, A., Wong, T., “A Q-band low phase noise monolithic AlGaN/GaN HEMT VCO,” *IEEE Microw. Compon. Lett.*, vol. 16, no. 7, pp. 425–427, July 2006.

[73] Dussopt, L., Rebeiz, G.M., “A low phase noise Silicon 18-GHz push-push VCO,” *IEEE Microw. Compon. Lett.*, vol. 13, no. 1, pp. 4–6, Jan. 2003.

[74] Young-Taek Lee, Jaechun Lee, Sangwook Nam, “High-Q active resonators using amplifiers and their applications to low phase-noise free-running and voltage-controlled oscillators,” *IEEE Trans. Microw. Theory Techn.*, vol. 52, no.11, pp. 2621–2626, Nov. 2004.

[75] Tsuru, M., Nishida, K., Kawakami, K., Yamaguchi, D., Komaki, M., Taniguchi, E., Hieda, M., “Formulation of a dual-tapped microstrip resonator VCO,” *IEEE Trans. Microw. Theory Techn.*, vol. 62, no. 11, pp. 2733–2742, Nov. 2014.

[76] Bao, M., Yinggang Li, Jacobsson, H., “A 25-GHz ultra-low phase noise InGaP/GaAs HBT VCO,” *IEEE Microw. Compon. Lett.*, vol. 15, no. 11, pp. 751–753, Nov. 2005.

[77] Choi, J., Mortazawi, A., “A new X-band low phase-noise multiple-device oscillator based on the extended-resonance technique,” *IEEE Trans. Microw. Theory Techn.*, vol. 55, no.8, pp. 1642–1648, Nov. 2007.

[78] Infineon Technologies. *Applicat. note CFY25-20* [Online].
Available: http://www.infineon.com

[79] Ghodgaonkar, D.K., Varadan, V.V., Varadan, V.K., “Free-space measurement of complex permittivity and complex permeability of magnetic materials at microwave frequencies,” *IEEE Trans. Instrum. Meas.*, vol. 39, no. 2, pp. 387–394, April 1990.

[80] Ziolkowski, R.W., “Design, fabrication, and testing of double negative metamaterials,” *IEEE Trans.Antennas Propagat.*, vol. 51, no. 7, pp. 1516–1529, July 2003.

APPENDIX A

Abstract noise representation of the system with cascaded stages

For an abstract noise representation of the system with cascaded stages, consider,

R_s = Source resistor

I_{nDm} = *Effective* channel thermal noise present at the output end of the m^{th} stage device. It is a function of channel thermal noise i_{nD}.

R_{stabm} = Series stability resistor connected at the drain of the m^{th} stage

$\overline{V_{nR_{stab_m}}^2} = 4R_{stab_m}kT$ = m^{th} stage stability resistor thermal noise

Z_{INm} = m^{th} stage input impedance

Z_{OUTm} = m^{th} stage output impedance considering stability resistor and matching network

Z'_{OUTm} = m^{th} stage output impedance without considering stability resistor and matching network

A_{vm} = Unloaded m^{th} stage voltage gain

Noise to the first stage input port is, $\overline{v_{n_{in1}}^2} = \overline{v_{nR_s}^2}\left|\frac{Z_{IN_1}}{R_s + Z_{IN_1}}\right|^2 = \overline{v_{n_{in}}^2}$

Noise from the first stage output port is,

$$\overline{v_{n_{out1}}^2} = A_{v_1}^2\overline{v_{n_{in1}}^2} + \left(\overline{I_{nD_1}^2}\left|Z'_{OUT_1}\right|^2\right)\left|\frac{R_{stab_1}}{Z'_{OUT_1} + R_{stab_1}}\right|^2 + \overline{v_{nR_{stab_1}}^2}$$

Noise to the second stage input and from the output is,

$$\overline{v_{n_{in2}}^2} = \overline{v_{n_{out1}}^2}\left|\frac{Z_{IN_2}}{Z_{OUT_1} + Z_{IN_2}}\right|^2$$

$$\overline{v_{n_{out2}}^2} = A_{v_2}^2\overline{v_{n_{in2}}^2} + \left(\overline{I_{nD_2}^2}\left|Z'_{OUT_2}\right|^2\right)\left|\frac{R_{stab_2}}{Z'_{OUT_2} + R_{stab_2}}\right|^2 + \overline{v_{nR_{stab_2}}^2}$$

Similarly for the third stage,

$$\overline{v_{n_{in3}}^2} = \overline{v_{n_{out2}}^2}\left|\frac{Z_{IN_3}}{Z_{OUT_2}+Z_{IN_3}}\right|^2$$

$$\overline{v_{n_{out3}}^2} = A_{v_3}^2\overline{v_{n_{in3}}^2} + \left(\overline{I_{nD_3}^2}\left|Z_{OUT_3}^{'}\right|^2\right)\left|\frac{R_{stab_3}}{Z_{OUT_3}^{'}+R_{stab_3}}\right|^2 + \overline{v_{nR_{stab_3}}^2}$$

Noise delivered to load is the final output noise and can be written as,

$$\overline{v_{n_{out}}^2} = \overline{v_{n_{out3}}^2}\left|\frac{Z_L}{Z_{OUT_3}+Z_L}\right|^2$$

where,

$$\overline{v_{n_{out3}}^2} = A_{v_3}^2\left(\begin{array}{l}\left(\begin{array}{l}A_{v_2}^2\left(\left(A_{v_1}^2\left(\overline{v_{nR_s}^2}\left|\frac{Z_{IN_1}}{R_s+Z_{IN_1}}\right|^2\right)+\left(\overline{I_{nD_1}^2}\left|Z_{OUT_1}^{'}\right|^2\right)\left|\frac{R_{stab_1}}{Z_{OUT_1}^{'}+R_{stab_1}}\right|^2+\overline{v_{nR_{stab_1}}^2}\right)\left|\frac{Z_{IN_2}}{Z_{OUT_1}+Z_{IN_2}}\right|^2\right)\\ +\left(\overline{I_{nD_2}^2}\left|Z_{OUT_2}^{'}\right|^2\right)\left|\frac{R_{stab_2}}{Z_{OUT_2}^{'}+R_{stab_2}}\right|^2+\overline{v_{nR_{stab_2}}^2}\end{array}\right)\left|\frac{Z_{IN_3}}{Z_{OUT_2}+Z_{IN_3}}\right|^2\\ +\left(\overline{I_{nD_3}^2}\left|Z_{OUT_3}^{'}\right|^2\right)\left|\frac{R_{stab_3}}{Z_{OUT_3}^{'}+R_{stab_3}}\right|^2+\overline{v_{nR_{stab_3}}^2}\end{array}\right)$$

$$A_v^2 = \left|\frac{Z_{IN_1}}{R_s+Z_{IN_1}}\right|^2 A_{v_1}^2\left|\frac{Z_{IN_2}}{Z_{OUT_1}+Z_{IN_2}}\right|^2 A_{v_2}^2\left|\frac{Z_{IN_3}}{Z_{OUT_2}+Z_{IN_3}}\right|^2 A_{v_3}^2\left|\frac{Z_L}{Z_{OUT_3}+Z_L}\right|^2$$

Noise factor of a three stage amplifier may be expressed by,

$$F = \frac{1}{A_v^2}\frac{\overline{v_{n_{out}}^2}}{\overline{v_{n_{in}}^2}}$$

$$= 1 + \frac{\left(\overline{I_{nD_1}^2}\left|Z_{OUT_1}^{'}\right|^2\right)\left|\frac{R_{stab_1}}{Z_{OUT_1}^{'}+R_{stab_1}}\right|^2+\overline{v_{nR_{stab_1}}^2}}{\left|\frac{Z_{IN_1}}{R_s+Z_{IN_1}}\right|^2 A_{v_1}^2\overline{v_{nR_s}^2}} + \frac{\left(\overline{I_{nD_2}^2}\left|Z_{OUT_2}^{'}\right|^2\right)\left|\frac{R_{stab_2}}{Z_{OUT_2}^{'}+R_{stab_2}}\right|^2+\overline{v_{nR_{stab_2}}^2}}{\left|\frac{Z_{IN_1}}{R_s+Z_{IN_1}}\right|^2 A_{v_1}^2\left|\frac{Z_{IN_2}}{Z_{OUT_1}+Z_{IN_2}}\right|^2 A_{v_2}^2\overline{v_{nR_s}^2}}$$

$$+ \frac{\left(\overline{I_{nD_3}^2}\left|Z_{OUT_3}^{'}\right|^2\right)\left|\frac{R_{stab_3}}{Z_{OUT_3}^{'}+R_{stab_3}}\right|^2+\overline{v_{nR_{stab_3}}^2}}{\left|\frac{Z_{IN_1}}{R_s+Z_{IN_1}}\right|^2 A_{v_1}^2\left|\frac{Z_{IN_2}}{Z_{OUT_1}+Z_{IN_2}}\right|^2 A_{v_2}^2\left|\frac{Z_{IN_3}}{Z_{OUT_2}+Z_{IN_3}}\right|^2 A_{v_3}^2\overline{v_{nR_s}^2}}$$

In general, the analyzed equation is applicable to any *m* number of cascaded stages.

APPENDIX B

Resistor temperature noise representation considering sixteen-element device distributed model for three-stage LNA

Let us consider the small signal device model presented in Fig. 3.19.

For an intrinsic device,

$$i_1 = \frac{v_1}{R_i + \frac{1}{j\omega C_{gs}}} + \frac{v_1 - v_2}{R_{gd} + \frac{1}{j\omega C_{gd}}} - i_{ngs} + i_{ngd}\left(\frac{j\omega C_{gd}}{\frac{1}{R_{gd}} + j\omega C_{gd}}\right) \quad ..(B.1)$$

$$i_2 = \frac{g_m(\omega)e^{-j\omega\tau}v_1}{R_i + \frac{1}{j\omega C_{gs}}}\frac{1}{j\omega C_{gs}} + v_2\left(\frac{1}{R_{ds}} + j\omega C_{ds}\right) - \frac{v_1 - v_2}{R_{gd} + \frac{1}{j\omega C_{gd}}} - i_{nds} - i_{ngd}\left(\frac{j\omega C_{gd}}{\frac{1}{R_{gd}} + j\omega C_{gd}}\right) \quad ... ...(B.2)$$

Intrinsic HEMT 2-port Y-parameter matrix can be analyzed as, $\left[Y^{in}\right] = \begin{bmatrix} Y_{11}^{in} & Y_{12}^{in} \\ Y_{21}^{in} & Y_{22}^{in} \end{bmatrix}$,

where,

$$Y_{11}^{in} = \frac{1}{D_1 D_2}\left[\omega^2\left(R_{gd}C_{gd}^2 D_1 + R_i C_{gs}^2 D_2\right) + j\omega\left(D_1 C_{gd} + D_1 C_{gs}\right)\right]$$

$$Y_{12}^{in} = -\frac{1}{D_2}\left(\omega^2 R_{gd}C_{gd}^2 + j\omega C_{gd}\right)$$

$$Y_{21}^{in} = \frac{1}{D_1 D_2}\left[\left(D_2 g_m(\omega)e^{-j\omega\tau} - D_1\omega^2 R_{gd}C_{gd}^2\right) - j\omega\left(D_2 g_m(\omega)e^{-j\omega\tau}R_i C_{gs} + D_1 C_{gd}\right)\right]$$

$$Y_{22}^{in} = \left(\frac{1}{R_{ds}} + \frac{\omega^2 R_{gd}C_{gd}^2}{D_2}\right) + j\omega\left(C_{ds} + \frac{C_{gd}}{D_2}\right)$$

where, $D_1 = 1 + \omega^2 R_i C_{gs}^2$ *and* $D_2 = 1 + \omega^2 R_{gd}C_{gd}^2$

However, i_1 and i_2 in terms of local noise current sources for the intrinsic device can be analyzed as,

$$i_1 = v_1 Y_{11}^{in} + v_2 Y_{12}^{in} - i_{ngs} + i_{ngd}\left(\frac{j\omega C_{gd}}{\frac{1}{R_{gd}} + j\omega C_{gd}}\right)$$

$$i_2 = v_1 Y_{21}^{in} + v_2 Y_{22}^{in} - i_{nds} - i_{ngd}\left(\frac{j\omega C_{gd}}{\frac{1}{R_{gd}} + j\omega C_{gd}}\right)$$

Noiseless system with external noise sources of i_{n1} and i_{n2}, applied at the input and output respectively, will generate the same noise as it existed internally considering the noisy system [38,39,43].

For an intrinsic device, extracted noises $\overline{i_{n1}^2}$ and $\overline{i_{n2}^2}$ may be expressed as,

$$i_{n1} = -i_{ngs} + i_{ngd}\left(\frac{j\omega C_{gd}}{\frac{1}{R_{gd}} + j\omega C_{gd}}\right)$$

$$i_{n2} = -i_{nds} - i_{ngd}\left(\frac{j\omega C_{gd}}{\frac{1}{R_{gd}} + j\omega C_{gd}}\right)$$

$$\overline{i_{n1}^2} = \overline{i_{ngs}^2} + \overline{i_{ngd}^2}\left(\frac{j\omega C_{gd}}{\frac{1}{R_{gd}} + j\omega C_{gd}}\right)^2 = 4kT\left(\frac{1}{R_i} + \frac{1}{R_{gd}}\left(\frac{j\omega C_{gd}}{\frac{1}{R_{gd}} + j\omega C_{gd}}\right)^2\right) \quad \text{... ...(B.3)}$$

$$\overline{i_{n2}^2} = \overline{i_{nds}^2} + \overline{i_{ngd}^2}\left(\frac{j\omega C_{gd}}{\frac{1}{R_{gd}} + j\omega C_{gd}}\right)^2 = 4kT\left(\frac{1}{R_{ds}} + \frac{1}{R_{gd}}\left(\frac{j\omega C_{gd}}{\frac{1}{R_{gd}} + j\omega C_{gd}}\right)^2\right) \quad \text{... ...(B.4)}$$

where, $\overline{i_{ngs}^2}$, $\overline{i_{ngd}^2}$ and $\overline{i_{nds}^2}$ as shown in Fig. 2.4, are uncorrelated intrinsic noise sources. However, $\overline{i_{n1}^2}$ and $\overline{i_{n2}^2}$ are correlated, which can be noticed from equations (B.3) and (B.4).

Here, two-port network analysis is carried out through out as device's source is always grounded. By embedding extrinsic package parasitics to $[Y^{in}]$, complete device Y-parameter matrix is analyzed to be $\left[Y^{ext}\right]=\begin{bmatrix} Y_{11}^{ext} & Y_{12}^{ext} \\ Y_{21}^{ext} & Y_{22}^{ext} \end{bmatrix}$ as follows:

$$\begin{bmatrix} Y_{11}^{in} & Y_{12}^{in} \\ Y_{21}^{in} & Y_{22}^{in} \end{bmatrix}$$

$$\downarrow \quad Y \rightarrow Z$$

$$\begin{bmatrix} Z_{11} & Z_{12} \\ Z_{21} & Z_{22} \end{bmatrix}$$

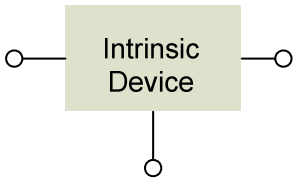

$$\begin{bmatrix} Z_{11}+R_g+R_s+j\omega\left(L_g+L_s\right) & Z_{12}+R_s+j\omega L_s \\ Z_{21}+R_s+j\omega L_s & Z_{22}+R_d+R_s+j\omega\left(L_d+L_s\right) \end{bmatrix}$$

$$\downarrow \quad \mathrm{Z} \rightarrow Y$$

$$\begin{bmatrix} Y_{11} & Y_{12} \\ Y_{21} & Y_{22} \end{bmatrix}$$

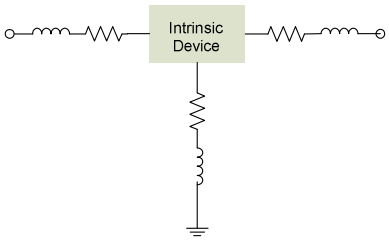

$$\begin{bmatrix} Y_{11}+j\omega\left(C_{pgs}+C_{pgd}\right) & Y_{12}-j\omega C_{pgd} \\ Y_{21}-j\omega C_{pgd} & Y_{22}+j\omega\left(C_{pds}+C_{pgd}\right) \end{bmatrix}$$

$$\downarrow \quad Y \rightarrow Z$$

$$\begin{bmatrix} Z_{11} & Z_{12} \\ Z_{21} & Z_{22} \end{bmatrix}$$

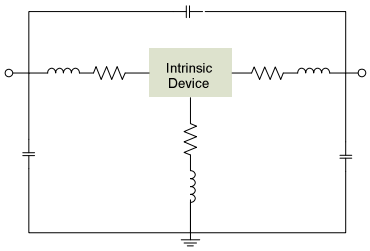

$$\begin{bmatrix} Z_{11} & Z_{12} \\ Z_{21} & Z_{22}+Z_L \end{bmatrix}$$

$$\downarrow \quad \mathrm{Z} \rightarrow Y$$

$$\begin{bmatrix} Y_{11}^{ext} & Y_{12}^{ext} \\ Y_{21}^{ext} & Y_{22}^{ext} \end{bmatrix}$$

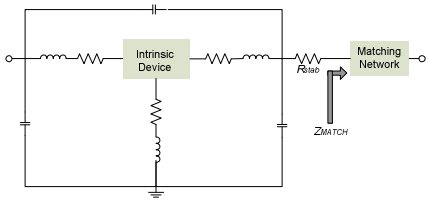

Correlated external input and output noise sources i_{n1} and i_{n2} for the complete three-stage noiseless LNA, considering device intrinsic and extrinsic package parasitics are analyzed as a function of various inherent noise sources and device parameters as follows:

$$i_{n1} = i_{ngs}\left[Y_g\left(-Z_{ngs}{}' - Z_{ngs}\frac{Z_g{}'}{Z_e}\right)\right] + i_{nds}\left[Y_g\left(Z_{nds}{}' - Z_{nds}\frac{Z_g{}'}{Z_e}\right)\right] + i_{ngd}\left[Y_g\left(Z_{ngd}{}' + Z_{ngd}\frac{Z_g{}'}{Z_e}\right)\right]$$
$$+ i_{nZ_L}\left[Y_g\left(Z_{nL}{}' + Z_{nL}\frac{Z_g{}'}{Z_e}\right)\right] + i_{nRs}\left[Y_g\left(Z_{nRs}{}' + Z_{nRs}\frac{Z_g{}'}{Z_e}\right)\right] + i_{nRd}\left[Y_g\left(Z_{nRd}{}' + Z_{nRd}\frac{Z_g{}'}{Z_e}\right)\right]$$
$$+ i_{nRg}R_g\left[Y_g\left(1 + \frac{Z_g{}'}{Z_e}\right)\right]$$

... ...(B.5)

$$i_{n2} = -i_{ngs}\frac{Z_{ngs}}{Z_e} - i_{nds}\frac{Z_{nds}}{Z_e} + i_{ngd}\frac{Z_{ngd}}{Z_e} + i_{nZ_L}\frac{Z_{nL}}{Z_e} + i_{nRs}\frac{Z_{nRs}}{Z_e} + i_{nRd}\frac{Z_{nRd}}{Z_e} + i_{nRg}\frac{R_g}{Z_e} \quad \text{... ...(B.6)}$$

The values of various impedance and admittance parameters used in the equations (B.5) and (B.6) are presented in Table B.1. In the analysis, identical devices are considered in all the three-stages.

Table B.1. Values of the parameters used in equation (B.5) and (B.6)

$$Z_g = \frac{1}{Y_g} = R_g + j\omega L_g$$

$$Z_d = R_d + j\omega L_d$$

$$Z_s = R_s + j\omega L_s$$

$$Z_L = R_{stab} + Z_{match}$$

$$Z_{gd} = R_{gd} + \frac{1}{j\omega C_{gd}}$$

$$Z_{gs} = R_i + \frac{1}{j\omega C_{gs}}$$

$$Y_{ds} = \frac{1}{R_{ds}} + j\omega C_{ds}$$

$$Y_1 = \frac{1}{R_g + j\omega L_g} + j\omega\left(C_{pgs} + C_{pgd}\right)$$

$$\frac{1}{Z_P} = Y_{ds} + \frac{1}{Z_{gs}} + \frac{1}{Z_s}$$

$$\frac{1}{Z_A} = \frac{1}{Z_{gd}} + \frac{Z_P}{Z_{gs}} Y_{ds} + \left(Z_P Y_{ds} - 1\right)\frac{g_m(\omega)e^{-j\omega\tau}}{Z_{gs}\left(j\omega C_{gs}\right)}$$

$$K_A = 1 + \frac{Z_g}{Z_{gs}} + \frac{Z_g}{Z_{gd}} - \frac{Z_g Z_P}{Z_{gs}^2}\left(1 + \frac{g_m(\omega)e^{-j\omega\tau}}{j\omega C_{gs}}\right)$$

$$K_B = -\frac{Z_g}{Z_{gd}} - \frac{Z_g}{Z_{gs}} Z_P Y_{ds}$$

$$Y_B = \frac{1}{Z_{gd}} + Y_{ds} - Y_{ds}^2 Z_P$$

$$K = Y_B Z_A K_A + K_B$$

$$Z_{nL} = Z_L\left[K + j\omega\left(C_{pds} + C_{pgd}\right)\left(KZ_d + Z_A K_A\right)\right]$$

$$Z_{nL}' = Z_L Z_A\left[Y_B + j\omega\left(C_{pds} + C_{pgd}\right)\left(1 + Z_d Y_B\right)\right]$$

$$Z_{ngs} = Z_A Z_P Y_{ds} K_A - Z_g\left(1 - \frac{Z_P}{Z_{gs}}\right)$$

$$Z_{ngs}' = Z_A Z_P Y_{ds}$$

$$Z_{nds} = Z_A K_A\left(Z_P Y_{ds} - 1\right) + \frac{Z_g Z_P}{Z_{gs}}$$

$$Z_{nds}' = Z_A\left(1 - Z_P Y_{ds}\right)$$

$$Z_{nRs} = \frac{R_s Z_P}{Z_s}\left(Y_{ds} Z_A K_A + \frac{Z_g}{Z_{gs}}\right)$$

$$Z_{nRs}' = Z_{ngs}' = Z_A Z_P Y_{ds}\frac{R_s}{Z_s}$$

$$Z_{nRd} = KR_d$$

$$Z_{nRd}' = Y_B Z_A R_d$$

$$Z_{ngd} = Z_A K_A \frac{j\omega C_{gd}}{\frac{1}{R_{gd}} + j\omega C_{gd}}$$

$$Z_{ngd}' = Z_A \frac{j\omega C_{gd}}{\frac{1}{R_{gd}} + j\omega C_{gd}} = \frac{Z_{ngd}}{K_A}$$

Now consider the Fig. B.1 representing external equivalent noise sources i_n and v_n applied to the noiseless 2-port network.

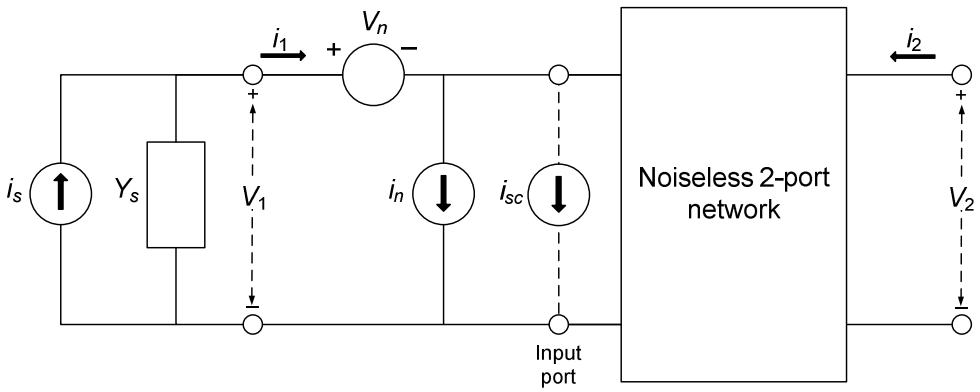

Fig. B.1. Equivalent input referred correlated noise sources

Input referred equivalent noises i_n and v_n can be represented in terms of the analyzed i_{n1} and i_{n2} as follows:

$$i_1 = (v_1 - v_n)Y_{11}^{ext} + v_2 Y_{12}^{ext} + i_n$$

$$i_2 = (v_1 - v_n)Y_{21}^{ext} + v_2 Y_{22}^{ext}$$

$$i_{n1} = i_n - v_n Y_{11}^{ext}$$

$$i_{n2} = -v_n Y_{21}^{ext}$$

$$i_n = i_{n1} - i_{n2}\frac{Y_{11}^{ext}}{Y_{21}^{ext}} \quad \text{... ...(B.7)}$$

$$v_n = -\frac{i_{n2}}{Y_{21}^{ext}} \quad \text{... ...(B.8)}$$

i_{sc} is the short circuit current and so it is the noise current which flows at the input port of the 2-port network. i_s is the input noise current due to the source. Considering that i_{sc} flows in the direction as shown in the Fig. B.1,

$$\overline{i_{sc}^2} = \overline{(i_s - i_n - v_n Y_s)^2} = \overline{i_s^2} + \overline{(i_n + v_n Y_s)^2} - 2\overline{i_s (i_n + v_n Y_s)} = \overline{i_s^2} + \overline{(i_n + v_n Y_s)^2}$$

where, $Y_s = G_s + jB_s$ is the source admittance. As i_n and v_n are system's extracted noise, source noise i_s is uncorrelated with i_n and v_n. However, i_n and v_n are correlated [3,39,43].

Noise factor of the two-port network is given by,

$$F = \frac{\overline{i_{sc}^2}}{\overline{i_s^2}} = 1 + \frac{\overline{\left(i_n + v_n Y_s\right)^2}}{\overline{i_s^2}}$$

Proceeding further, the conditions for minimum noise factor F_{min} in terms of optimum source termination $Y_{opt}=G_{opt}+jB_{opt}$ is given by, [3,37,39,43]

$$\frac{d\left(F\big|_{B_s=-B_c}\right)}{dG_s} = 0$$

$$where,\ Y_c = \frac{\overline{v_n^* i_n}}{\overline{v_n^2}}$$

$Y_c=G_c+jB_c$ is the correlation admittance.

Noise factor F in terms of F_{min} and optimum value of source termination can be represented as, [3,37,39,43]

$$F = F_{\min} + \frac{R_n}{G_s}\left[\left(G_s - G_{opt}\right)^2 + \left(B_s - B_{opt}\right)^2\right] \quad \text{... ...(B.9)}$$

$$where,\ G_s = \frac{\overline{i_s^2}}{4KT},\ R_n = \frac{\overline{v_n^2}}{4KT}$$

Hence, source termination admittance Y_{opt} will give the minimum noise figure.

List of Publications

[1] Sanket S. Patel, Sanjeev Gupta, and Deepak Ghodgaonkar, "Ku-Band Low Noise Multistage Amplifier MIC Design Having Performance Comparable to MMIC," in *Proc. of Third IEEE Int. Conf. on Advances in Comput., Commun. and Informatics,* New Delhi, 24–27 Sept., 2014, pp. 501–506.

Conference track: Advances in Satellite Communications and Networking (SatComNet)

Acceptance rate: 20.6%

IEEE sponsored conference ID# 33166

IEEE sponsors: IEEE Communications Society (IEEE ComSoc), IEEE Systems, Man, and Cybernetics Society (IEEE SMC)

Jointly organized with: Hochschule Offenburg, University of Applied Sciences, Germany.

[2] Sanket S. Patel, Sanjeev Gupta, and Deepak Ghodgaonkar, "Analysis of Nonlinear Effects on Operation of Low Noise Amplifier For Satellite Scatterometer," in *Proc. of Sixth IEEE Int. Conf. on Comput. Intell. and Commun. Netw.*, Bhopal, 14–16 Nov., 2014, pp. 97-101.

[3] Sanket S. Patel, Sanjeev Gupta, and Deepak Ghodgaonkar, "Ku-Band Novel Voltage Controlled Oscillator Microwave Integrated Circuit with Low Phase Noise," in *Proc. of Sixth IEEE Int. Conf. on Comput. Intell. and Commun. Netw.*, Bhopal, 14–16 Nov., 2014, pp. 74-77.

For papers [2] and [3]:

Conference track: Microwave IC, Antennas and Wave Propagation

Acceptance rate: 16.6%

IEEE sponsored conference ID# 35037

Technically sponsored by: IEEE Microwave Theory and Techniques Society (IEEE MTT-S)

[4] Sanket S. Patel, Sanjeev Gupta, and Deepak Ghodgaonkar, “Design of Low Power Low Phase Noise Negative Resistance Ku-Band VCO Using Planar Resonator Pair,” *Wiley Microw. and Optical Technol. Lett.*, vol. 57, no. 8, pp. 1938 – 1941, August 2015.

Award Received

Received 2014 IEEE M V Chauhan Award

The award was received from IEEE India Council Chair Dr. M. Ponnavaikko on December 13, 2014. A part of doctoral research was submitted for the contest. Submitted research stood *First* in all India Doctoral Category. The research was presented at the felicitation ceremony held at Pune.